

UNIVERSITÀ
DI PAVIA

UNIVERSITY OF PAVIA
FACULTY OF ENGINEERING
DEPARTMENT OF ELECTRICAL, COMPUTER AND BIOMEDICAL ENGINEERING

MASTER'S DEGREE IN ELECTRONIC ENGINEERING

MASTER THESIS

DYNAMICS OF PIEZO-ACTUATED VIBRATING STRUCTURES: RESULTS OF SIMULATIONS AND INTERFEROMETRIC MEASUREMENTS

DINAMICA DI STRUTTURE VIBRANTI PILOTATE DA ATTUATORI PIEZOELETTRICI: RISULTATI DI SIMULAZIONI E DI MISURE INTERFEROMETRICHE

Candidate: Bahareh Haddadi

Supervisor: Prof. Sabina Merlo

Co-supervisor: Carlo Anelli

A.A. 2025/2026

I dedicate this thesis to my family,
who are a part of who I am.
To my mother, who taught me patience.
To my father, from whom I learned to be strong.
And to my sister “Sharareh”, who is a part of my soul.

Abstract

The research activity carried out within the Laboratory of Electrooptics of the Department of electrical, computer and biomedical engineering at the University of Pavia has demonstrated the application of laser diode feedback interferometry, also known as self-mixing interferometry (SMI), for the non-contact characterization of piezoelectrically actuated planar structures and fluid chambers, and the exploitation of their vibrational modes for particle manipulation.
In this work, a near-infrared laser diode is focused by a lens on the vibrating structure under test. A fraction of the backscattered light re-enters the laser cavity and modulates the optical power, which is detected by the monitor photodiode integrated in the laser package and converted into a voltage signal by a transimpedance amplifier. In the frequency domain, the piezoelectric actuator is driven by white noise and the spectrum is acquired by a dynamic signal analyzer. In the time domain, the actuator is driven by sinusoidal signals and the interferometric fringes, each corresponding to a displacement of half the laser wavelength, are acquired by an oscilloscope. The data are then loaded and elaborated in MATLAB environment to reconstruct displacement, displacement sensitivity and phase delay. The vibrational behavior has been evaluated at different spatial scales. Indeed, in the first part of the work a piezo-MEMS speaker and a piezo-actuated Plexiglas plate were characterized in terms of resonance frequencies and mode shapes. These results were then used to validate the experimental and numerical procedures on well-defined structures. In the second part, the same tools have been applied to a Petri dish and to a closed polymeric microchannel, with the piezoelectric actuator bonded to the structure. Direct Chladni patterns in dry conditions, with particles collected along the nodal lines, and inverse Chladni patterns in water, with particles driven towards the antinodes, have been studied. Thus, density-based separation of particles has been demonstrated, and iron particles have been trapped in the water-filled microchannel at its fundamental resonance. Preliminary tests with yeast cells and polystyrene microspheres have been carried out to explore the application to biological samples.
A 3D numerical model has been implemented in COMSOL Multiphysics, combining structural mechanics, electrostatics, pressure acoustics and particle tracing. The model has allowed to evaluate resonance frequencies, mode shapes, acoustic pressure fields and particle trajectories.
Experimental results have been found in good agreement with numerical results.
The potentialities of the platform have been explored through parameters as resonance frequency, displacement sensitivity and phase delay, and the limits of the present driving hardware for the manipulation of cell-scale particles have been identified.

Table of contents

Abstract

Objectives and Outline I

Chapter 1. State of the Art 1
1.1. Introduction to Piezoelectric Effect 1
1.2. Acoustics 2
1.3. Fluidic Actuation Using Piezoelectric Effect 3
1.3.1. Acoustic Radiation Force (ARF) 4
1.3.2. Acoustic streaming-induced drag force 5
1.4. Chladni patterns 6
1.4.1. Chladni Pattern in air 7
1.4.2. Inverse Chladni Pattern in water 7
1.5. Mesoscale Structural Actuation vs. Micro-Acoustofluidic Devices 8

Chapter 2. Materials and Methods 10
2.1. Instrumental Configuration 10
2.1.1. Frequency Domain Analysis (DSA) 13
2.1.2 .Time-domain Analysis (Wave Form Reconstruction) 14
2.2. Numerical Simulation (Finite-Element-Analysis) 17
2.2.1. Mechanical Analysis (Natural Frequencies) 17
2.2.2. Electromechanical Analysis 18
2.2.3. Particle Tracing 19

Chapter 3. Multiscale Characterization of Piezoelectrically Actuated planar structures for acoustic application 21

3.1. MEMS Speaker (Micromachined Acoustic Transducer) 21
3.1.1. Spectral Response (Resonance Frequencies) 22
3.1.2. time domain response: Displacement and Phase Delay analysis 23
3.2. Macro-Scale Structural Dynamics (Plexiglas) 27
3.2.1. Spectral Response (Resonance Frequencies) 28

3.3. Numerical Simulation Results (COMSOL Multiphysics) 29
3.3.1. Physics 30
3.3.2. Boundary Conditions 33
3.4. Comparison of numerical and Experimental Results 33

Chapter 4. Particle Manipulation in petri dish Using Piezoelectric Actuation 36
4.1. Introduction and Platform Overview 36
4.2 .Numerical Results 37
4.2.1. Mechanical Simulation 37
4.2.2. Electromechanical Simulation 38
4.2.3. Extended Acoustic-Pressure and Particle-Tracing Simulation (Water-filled condition) 40
4.3. Experimental Results 44
4.3.1. Spectral Response 44
4.3.2. Time-domain Response 46
4.3.3. Chladni Patterns 47

Chapter 5. Particle Manipulation in Microchannel (Ibidi) Using Piezoelectric Actuation 50
5.1. Material and Methods 50
5.2. Experimental Results 51
5.2.1. Spectral Response 51
5.3. Chladni Patterns 52
5.4. Numerical Results 54
5.4.1. Mechanical and Electromechanical Modes in Air-filled Microchannel 54
5.4.2. Water-Filled Response: Displacement and Acoustic Pressure spectra 56
5.4.3. Particle Tracing Simulation 60
5.5. Biological Application 63
5.5.1. Yeast in PBS 63
5.5.2. Polystyrene Microspheres 65

Conclusion and future perspectives 67

References 68

Objectives and Outline

Piezoelectric materials convert electrical signals into mechanical motion and vice versa, and for this reason they have become key components of modern micro-electromechanical systems, acoustic and ultrasonic transducers, sensors and lab-on-a-chip devices. Through the converse piezoelectric effect, a small actuator bonded to a plate, a dish or a microchannel can excite vibrational modes of the whole structure, generating displacement fields and, when a liquid is present, acoustic pressure fields and streaming.

In this framework, flat surfaces actuated by piezoelectric elements are emerging as promising candidates for next-generation loudspeakers, offering compactness, low power consumption, and efficient electro-acoustic conversion compared to traditional moving-coil systems. Their thin profiles make them simple to integrate and thus suitable for portable and wearable devices, as well as for the transformation of already existing display surfaces into sound-radiating elements.

However, their electromechanical performances strongly depend on the shape and material properties of the vibrating structure, and it is important to understand the influence of these parameters on their spectral dynamic response.

Recently, also microfluidic device actuated by piezoelectric elements are attracting a lot of interest since the piezoelectric effect can be used to move, trap and sort suspended particles without any moving mechanical part, which makes the approach attractive for biomedical, analytical and point-of-care applications.

Most acoustofluidic platforms reported in the literature operate in the MHz range and rely on surface or bulk acoustic waves, interdigital transducers and cleanroom micro-fabrication. These systems are very effective, but they are costly and often not compatible with standard laboratory consumables. A complementary approach might be low-frequency (kHz) mesoscale structural actuation: a piezoelectric patch excites the flexural modes of a commercial, low-cost substrate such as a Petri dish or a polymer microchannel. At these frequencies the acoustic wavelength in the liquid is much larger than the device, so the particle motion is governed by the vibration of the structure and by its coupling with the fluid, rather than by a classical ultrasonic standing wave. The design of such devices requires a reliable knowledge of their resonance frequencies, mode shapes and displacement amplitudes, which are not easy to measure without contact and without bulky equipment.

The objective of this Thesis was the experimental and numerical characterization of piezoelectrically actuated structures at different scales, and the exploitation of their vibrational modes for particle manipulation. For the optical characterization we used laser diode feedback interferometry, also known as self-mixing interferometry. It is a compact, low-cost and non-contact technique in which the laser diode is at the same time the source and the sensing element, so that no external interferometer is needed. It allowed us to measure both the spectral response, using broadband excitation, and the out-of-plane displacement in the time domain, by counting and processing the interferometric fringes, each corresponding to a displacement of half the laser wavelength. The experimental work was supported by three-dimensional finite-element models implemented in COMSOL Multiphysics, which combine mechanical, electromechanical, acoustic and particle-tracing analyses and provide the mode shapes, the acoustic pressure fields and the expected particle trajectories.

The work followed a multiscale approach. We first characterized a piezo-MEMS speaker and a piezo-actuated Plexiglas plate, in order to validate the measurement and modeling procedures on well-defined structures. Then, we applied the same tools to a water-filled Petri dish and to a polymer microchannel in the format of a microscopy slide, studying how the

liquid modifies the resonances and how particles are redistributed in the dry condition (Chladni patterns) and in the liquid condition (inverse Chladni patterns). Finally, we tested the microchannel with different particles, to identify the potentiality and the limitation of the available platform.
The organization of the Thesis is described in the following paragraphs.
Chapter 1: Presentation of the state of the art. The chapter introduces the piezoelectric effect, the constitutive equations and the main piezoelectric materials, the basic concepts of acoustics, and the principles of fluidic actuation based on the acoustic radiation force and on the acoustic streaming drag force. Chladni patterns in air and inverse Chladni patterns in water are described, and mesoscale structural actuation is compared with high-frequency micro-acoustofluidic devices.
Chapter 2: Description of materials and methods. The self-mixing interferometric setup is presented, together with the frequency-domain and time-domain measurement procedures and the MATLAB algorithm for displacement reconstruction. The second part of the chapter describes the COMSOL models: mechanical and electromechanical analysis, acoustic analysis and particle tracing.
Chapter 3: Characterization of piezoelectrically actuated planar structures for acoustic applications. The piezo-MEMS speaker and the piezo-actuated Plexiglas plate are studied experimentally and numerically, in terms of resonance frequencies, displacement sensitivity and phase delay.
Chapter 4: Particle manipulation in a Petri dish. Numerical and experimental resonances in dry and water-filled conditions are compared, the spatial distribution of the displacement is mapped, and Chladni and inverse Chladni patterns are demonstrated with particles denser and lighter than water.
Chapter 5: Particle manipulation in a polymer microchannel. The closed channel is characterized in air-filled and water-filled conditions. Simulated and measured resonances and particle patterns are compared. Experiments with yeast cells in PBS and polystyrene microspheres are used to assess the limits of the platform for biological applications.
Summary of the main results of the Thesis and discussion of possible future developments are reported in the Conclusions.

Chapter 1. State of The Art

1.1. Introduction to Piezoelectric Effect

The piezoelectric effect represents a first-order linear electromechanical coupling phenomenon observed in specific crystalline materials that lack inversion symmetry in their non-centrosymmetric crystal structures [1]. This fundamental physical behavior is categorically divided into two distinct modes of operation: the direct piezoelectric effect and the converse piezoelectric effect [1, 2]. The direct piezoelectric effect, fundamentally discovered by Jacques and Pierre Curie in 1880, describes the generation of an electric polarization and a subsequent macroscopic surface charge density when the material is subjected to external mechanical stress [2]. Mathematically, this external mechanical load shifts the relative positions of the constitutive anions and cations within the crystal lattice, thereby inducing a net dipole moment [3]. Conversely, the converse piezoelectric effect involves the induction of mechanical strain or dimensional deformation within the crystalline lattice upon the application of an external electric field [1, 4]. In modern engineering, particularly in Micro-Electro-Mechanical Systems (MEMS), ultrasonic transducers, and acoustofluidic manipulation platforms, this dual-mode capability establishes piezoelectric materials as a crucial bridge between electrical excitation and mechanical actuation [3, 5].

At the microscopic domain level, the emergence of the piezoelectric effect is strictly governed by the spatial symmetry of the material's unit cell [2]. Out of the 32 well-defined crystal classes, 21 lack a center of symmetry, and 20 of these non-centrosymmetric classes exhibit inherent piezoelectric properties [2, 4]. In their natural or unpolarized state, the individual electric dipoles within these materials are randomly oriented across multiple ferroelectric domains, resulting in a net macroscopic polarization of zero [4]. To induce high-efficiency piezoelectric behavior suitable for reproducible acoustic actuation, the material must undergo a thermal-electrical treatment known as the poling process [1]. During poling, the material is heated below its characteristic Curie temperature (T_c), where the increased thermal energy enhances domain mobility [2]. A strong direct current (DC) electric field is then applied across the material boundaries, forcing the alignment of the electric dipoles along the vector of the applied field [1, 3]. As the system is gradually cooled below T_c with the electric field maintained, this anisotropic domain orientation becomes permanently locked into the crystal matrix, creating a highly responsive macroscopic piezoelectric axis [4].

To precisely evaluate, simulate, and design devices utilizing these materials such as planar structures or acoustic actuators the coupled linear electromechanical interactions must be expressed through strict constitutive relations [1]. Under low-frequency, quasi-static, and linear elastic approximations, these relationships couple the mechanical tensors, namely stress (T) and strain (S), with the vector components of the electrical domain, specifically the electric field (E) and electric displacement (D) [6]. Depending on the choice of independent variables, these relations can be formulated in four distinct matrix representations [2]. For structural and acoustic simulations, the strain-charge form is the most widely adopted framework, defined by the following coupled equations [1, 6]:

$$S_i = s_{ij}^E T_j + d_{ki} E_k \quad (1)$$

$$D_l = d_{lj} T_j + \varepsilon_{lk}^T E_k \quad (2)$$

In these equations, the index notation follows the standard IEEE compact matrix framework where mechanical indices i, j range from 1 to 6 (representing directional components of axial and shear stress/strain) and electrical indices k, l range from 1 to 3 (representing spatial Cartesian coordinates x, y, z) [6]. The variables and material tensors are defined as: S_i is the dimensionless strain tensor component, and T_j represents the mechanical stress tensor component (N/m^2), E_k is the applied or induced electric field vector (V/m), D_l denotes the macroscopic electric displacement vector (C/m^2), S_{ij}^E is the mechanical compliance tensor (m^2/N) measured under a constant, short-circuited electric field (E=0). d_{ki} and d_{lj} represent the piezoelectric coupling coefficients (C/N or m/V), which quantify the electromechanical conversion efficiency and ε_{lk}^T is the dielectric permittivity tensor (F/m) evaluated under constant, unconstrained mechanical stress (T=0).
For high-frequency acoustic applications and multi-scale fluidic actuation, the selection of the specific piezoelectric material composition acts as a primary design constraint, directly dictating the electromechanical coupling factor K_{eff}^2 and structural damping parameters [3]. Lead Zirconate Titanate ($Pb[Zr_xTi_{1-x}]O_3$ or PZT) ceramics are predominantly utilized in macro-scale structural dynamics due to their remarkably high piezoelectric charge constants (d_{33} and d_{31}) [4]. This high coefficient allows PZT to generate substantial displacement and high-amplitude acoustic pressure fields at relatively low driving voltages [1]. However, PZT exhibits severe manufacturing limitations at the micro-scale and is restricted in biological applications due to the inherent toxicity of lead [3, 4]. Consequently, for micro-scale systems such as microfluidic channels and silicon-integrated MEMS speakers, thin-film alternatives like Aluminum Nitride (AlN) and Zinc Oxide (ZnO) have become standard [5]. AlN, despite having lower piezoelectric constants compared to PZT, offers exceptional complementary metal-oxide-semiconductor (CMOS) integration capability, low intrinsic dielectric losses, high thermal conductivity, and an elevated acoustic velocity (≈11000 m/s), making it ideal for executing ultra-high frequency precise particle trapping and biocompatible cell manipulation [3, 5].

1.2. Acoustics

Acoustics in the context of micromachined, piezoelectrically actuated structures deals with the generation, transmission, and behavior of energy in the form of high-frequency vibrational waves [7]. When a planar or micro-scale system is harmonically excited via the converse piezoelectric effect, acoustic energy propagates through the medium, manifests as longitudinal pressure waves in fluids, and develops as combined longitudinal and shear waves within solid boundaries [8]. The fundamental behavior of an acoustic wave in an ideal, compressible, and non-viscous fluid medium is strictly governed by the classic conservation laws of continuum mechanics. These principles are mathematically formulated through the conservation of mass (continuity equation) and the conservation of momentum (Euler's equation). By applying a first-order perturbation analysis where the total pressure p_{total} and total density ρ_{total} are split into their ambient hydrostatic states (p_0, ρ_0) and small acoustic variations (p, ρ), the linear acoustic wave equation in terms of acoustic pressure (p) can be derived as follows [9]:

$$\nabla^2 p - \frac{1}{c_f^2}\frac{\partial^2 p}{\partial t^2} = 0 \tag{3}$$

Where ∇^2 represents the three-dimensional Laplacian operator and c_f denotes the thermodynamic speed of sound in the fluid domain. This velocity is intrinsically linked to the fluid's bulk modulus (β) and ambient density (ρ_0) through the classical relation $c_f = \sqrt{\beta/\rho_0}$ [10]. For systems under continuous harmonic excitation where the temporal dependence is represented by the complex exponential $e^{i\omega t}$, Equation (4) simplifies to the well-known inhomogeneous or homogeneous Helmholtz equation [11]:

$$\nabla^2 p + k^2 p = 0 \qquad (4)$$

Where $k=\omega/c_f$ represents the acoustic wavenumber and $\omega=2\pi f$ is the angular frequency of the applied electrical excitation signal. When these harmonic acoustic waves encounter geometric boundaries, such as the interface between the fluid domain and the solid walls of a Petri dish or a microchannel, reflection, transmission, and refraction phenomena take place due to the specific mismatch in acoustic impedance ($Z=\rho c$). The explicit boundary conditions at these interfaces dictate the formation of standing acoustic wave patterns, characterized by acoustic pressure nodes and antinodes, which are central to spatial particle trapping mechanisms [10,12]. However, in microscale or highly confined fluidic environments, the acoustic field cannot be treated as purely inviscid. Near any solid boundary, the fluid velocity must satisfy the no-slip condition, giving rise to an acoustic viscous boundary layer, often referred to as the Schlichting boundary layer [8]. The characteristic thickness of this viscous layer (δ_v) is extremely small and depends on the kinematic viscosity of the fluid (ν) and the operating frequency (ω), defined by [11]:

$$\delta_v = \sqrt{\frac{2\nu}{\omega}} \qquad (5)$$

The dissipation of acoustic energy within this ultra-thin boundary layer leads to non-linear, second-order time-averaged phenomena. This boundary interaction induces a localized Reynolds stress in the fluid, which ultimately drives steady rotational fluid flows known as acoustic streaming. Understanding the balance between these primary acoustic pressure fields and the secondary boundary-layer effects is crucial for predicting whether a suspended micro-particle will be governed by direct acoustic forces or viscous drag forces [7, 12].

1.3. Fluidic Actuation Using Piezoelectric Effect

The integration of piezoelectric actuation within microfluidic and meso-scale domains has established the robust discipline of acoustofluidics, where high-frequency mechanical vibrations are directly converted into controlled fluid motion and localized particle transport. When an alternating current (AC) signal is applied to a piezoelectric transducer, the converse piezoelectric effect generates bulk acoustic waves (BAWs) or surface acoustic waves (SAWs) that couple into the adjacent fluidic medium via structural boundaries [8]. Due to the compressibility of the fluid, these coupled mechanical oscillations establish a primary acoustic pressure field. As suspended micro-particles or biological cells interact with this localized energy field, they experience two dominant, competing physical forces: the direct Acoustic

Radiation Force (ARF) and the secondary Acoustic Streaming-Induced Drag Force [12]. In high-end electronic and Micro-Electro-Mechanical Systems (MEMS) designs, manipulating the operational frequency, electrical power, and boundary conditions allows for the precise tuning of these two forces to achieve spatial trapping, sorting, or mixing of target analytes [10].

1.3.1. Acoustic Radiation Force

The Acoustic Radiation Force (ARF) is a primary, first-order, time-averaged scattering phenomenon that arises from the direct transfer of momentum from the propagating or standing acoustic wave to a suspended particle [11]. When a micro-particle disturbs the ambient acoustic pressure field, it scatters the incident acoustic waves, generating a localized pressure differential across its boundary. For a small spherical particle whose radius (a) is significantly smaller than the acoustic wavenumber (k_a<<1), the time-averaged acoustic radiation force <F_{ARF}> can be rigorously derived from the gradient of a secondary thermodynamic potential field, widely known as the Gor'kov potential (U) [13]:

$$\langle F_{ARF} \rangle = -\nabla U \tag{6}$$

The Gor'kov potential expression encapsulates both the acoustic pressure fluctuations (p_1) and the acoustic fluid velocity perturbations (v_1) at the unperturbed position of the particle center, and is mathematically formulated as [13,14]:

$$U = 2\pi a^3 \left[\frac{\langle p_1^2 \rangle}{3\rho_0 c_f^2} f_1 - \frac{\rho_0 \langle v_1^2 \rangle}{2} f_2 \right] \tag{7}$$

where the brackets $\langle - \rangle$ denote a time-averaged evaluation over one full acoustic oscillation cycle. The dimensionless parameters f_1 and f_2 represent the monopole and dipole scattering coefficients, respectively, which quantify the acoustic contrast between the suspended particle and the host fluid domain based on their respective material properties [14]:

$$f_1 = 1 - \frac{k_p}{k_f} \tag{8}$$

$$f_2 = \frac{2(\rho_p - \rho_0)}{2\rho_p + \rho_0} \tag{9}$$

Here, ρ_p and k_p are the density and isentropic compressibility of the particle, while ρ_0 and k_f denote the identical thermodynamic parameters of the ambient fluid medium. In a standard one-dimensional standing acoustic wave field established between parallel resonant boundaries, the acoustic pressure can be simplified as $p_1 = p_a \cos(kx) \sin(\omega t)$. By substituting this field into Equation (7), the spatial acoustic radiation force equation resolves into a predictable sinusoidal function [11,15]:

$$\langle F_{ARF} \rangle = 4\pi \Phi k a^3 E_a \sin(2kx) \tag{10}$$

where $E_a = {p_a}^2/(4\rho_0 {c_f}^2)$ represents the time-averaged acoustic energy density of the acoustic field, and Φ is the critical dimensionless acoustic contrast factor, which dictates the explicit direction of particle migration within the standing wave pattern, defined as [15]:

$$\Phi = \frac{f_1}{3} + \frac{f_2}{2} = \frac{5\rho_p - 2\rho_0}{2\rho_p + \rho_0} - \frac{\kappa_p}{\kappa_f} \qquad (11)$$

The algebraic sign of the acoustic contrast factor (Φ) serves as a fundamental design parameter in MEMS sorting systems. A positive contrast factor ($\Phi>0$), typical for rigid solid particles and biological cells in aqueous solutions, forces the particles to migrate directly toward the acoustic pressure nodes (minimum pressure amplitude areas). Conversely, a negative contrast factor ($\Phi<0$), observed for highly compressible entities like lipid droplets or microbubbles, drives the structures toward the acoustic pressure antinodes (maximum pressure amplitude areas) [5,10]. Because the magnitude of F_{ARF} scales directly with the third power of the particle radius (a^3), the direct radiation force acts as the dominant mechanism for manipulating larger micro-particles and macroscopic structures [5,12].

1.3.2. Acoustic Streaming-Induced Drag Force

While the acoustic radiation force acts directly on the particle mass via wave scattering, the dissipation of acoustic energy within the fluid domain simultaneously drives a secondary steady, time-averaged fluid circulation known as acoustic streaming [16]. This steady bulk fluid motion is generated by the attenuation of the acoustic wave, which transfers its acoustic momentum to the fluid medium. In enclosed microfluidic structures, this attenuation occurs heavily within the ultra-thin viscous boundary layer (Schlichting layer) adjacent to the solid walls, giving rise to boundary-driven streaming cells, or Rayleigh streaming [17]. The continuous velocity field of this streaming vortex applies a viscous Stokes drag force on any suspended particle, which continuously opposes the direct trapping effects of the ARF. The time-averaged acoustic streaming-induced drag force $\langle F_{drag} \rangle$ acting on a spherical particle is governed by the classical hydrodynamic relation [17,18]:

$$\langle F_{drag} \rangle = 6\pi\eta_f a\big(\langle v_{str} \rangle - \langle v_p \rangle\big) \qquad (12)$$

where η_f represents the dynamic viscosity of the working fluid, $\langle v_{str} \rangle$ is the local time-averaged acoustic streaming velocity vector, and $\langle v_p \rangle$ denotes the velocity vector of the moving particle. The scaling behavior of these two phenomena introduces a critical physical boundary in multi-scale acoustofluidic applications. Since the acoustic radiation force scales with the volume of the particle ($F_{ARF} \propto a^3$) whereas the streaming drag force scales linearly with the radius ($F_{drag} \propto a$), a critical particle radius (a_{crit}) exists for every specific frequency and geometry. For particles with a radius significantly below a_{crit} (typically less than 1 µm at MHz frequencies), the viscous drag force of the streaming vortices completely dominates the system kinematics, causing the nano-particles or bacteria to follow the fluid streamlines instead of trapping at the nodes [19]. For larger particles ($a > a_{crit}$), the direct acoustic radiation force overcomes the fluidic drag, allowing for stable alignment and patterning. In high-frequency MEMS transducers and advanced structural manipulation networks,

mathematically predicting the spatial crossover between F_{ARF} and F_{drag} is a critical requirement for optimizing cell sorting, droplet handling, and bio-sensing efficiency [18,20].

1.4. Chladni patterns

Chladni patterns represent one of the most classical, yet highly sophisticated, manifestations of structural acoustics and wave mechanics in bounded planar domains. Originally discovered by Ernst Chladni in the late 18th century, this phenomenon involves the spatial distribution of granular materials on a vibrating plate or membrane, leading to the formation of distinct geometric figures that map the structural mode shapes of the operating system [21]. When a planar structure, such as a thin Plexiglas plate or a Petri dish substrate, is driven harmonically via a piezoelectric actuator, bending waves (Flexural waves) propagate through the solid matrix. The continuous reflection of these waves from the physical boundaries of the geometry establishes a two-dimensional standing wave field characterized by distinct regions of minimal and maximal mechanical displacement, known as nodal lines and antinodes, respectively [7,22]. In contemporary electrical and biomedical engineering, understanding the dynamics of Chladni patterns is crucial for executing macro-to-mesoscale acoustic particle manipulation without the need for complex micro-machined fluidic networks [8,23].
The fundamental governing equation for the harmonic, out-of-plane displacement w(x,y,t) of a thin, isotropic, and linear elastic planar structure subjected to an external harmonic actuation can be expressed through Kirchhoff-Love plate theory as [7,22]:

$$D\nabla^4 w + \rho_s h \frac{\partial^2 w}{\partial t^2} = F_e(x, y, t) \qquad (13)$$

where $\nabla^4 = \nabla^2(\nabla^2)$ is the biharmonic operator, ρ_s is the structural mass density, h is the plate thickness, and F_e represents the time-harmonic transverse driving force applied by the coupled piezoelectric actuator. The parameter D denotes the flexural rigidity of the plate, which depends on the material's Young's modulus (E) and Poisson's ratio (ν), formulated as [22]:

$$D = \frac{Eh^3}{12(1-\nu^2)} \qquad (14)$$

Under continuous steady-state harmonic excitation at a specific natural or resonance frequency (ω_n), the time-dependent displacement resolves into a spatial mode shape function W(x,y) such that $w(x, y, t) = W(x, y)e^{i\omega t}$. The configurations where W(x,y)=0 define the permanent non-vibrating geometric coordinates of the structure, which are designated as the structural nodal lines [26, 30]. The physical behavior of suspended or resting granular micro-particles placed on top of these vibrating surfaces depends heavily on the ambient fluid medium (e.g., air versus water), leading to either regular or inverse Chladni manipulation regimes [23, 26].

1.4.1. Chladni Pattern in air

When the acoustic manipulation process is conducted in air, the physical arrangement of granular matter typically follows the regular or classical Chladni Pattern regime, where

particles migrate dynamically away from the high-amplitude vibrating regions (antinodes) and gather securely along the non-vibrating structural nodal lines [24]. The primary kinetic mechanism driving this spatial distribution is a sequence of transient mechanical impacts and gravitational components. When a particle rests on an antinodal region of a piezoelectrically driven plate, the localized vertical acceleration of the surface ($\partial^2\omega/\partial t^2 = -\omega^2 W$) easily exceeds the gravitational acceleration (g), causing the particle to lose physical contact and undergo repeated ballistic flights or bouncing motions [24, 25], where ω represents the time-dependent, instantaneous out-of-plane displacement of the plate surface, W denotes the time-independent spatial amplitude or mode shape function of the flexural wave, and t represents the temporal variable.

During these cyclic physical impacts, the asymmetric slope of the flexural standing wave at the point of contact imparts a horizontal net momentum to the bouncing particle. Mathematically, the net time-averaged drift force $\langle F_{drift} \rangle$ directing a solid particle toward a nodal coordinate in a gaseous ambient medium can be phenomenologically modeled as a function of the local spatial gradient of the mean square velocity of the plate surface [15, 25]:

$$\langle F_{drift} \rangle \propto -\nabla \langle (\frac{d\omega}{dt})^2 \rangle \qquad (15)$$

Because the ambient density and dynamic viscosity of air are remarkably low ($\rho_{air} \approx 1.2$ kg/m^3), the acoustic streaming vortices generated in the surrounding gas domain are generally too weak to overcome the inertia of macro- and mesoscale granular materials [24]. Consequently, the particles accumulate continuously at the positions where the structural velocity and displacement are zero W(x,y)=0. Recording these precise physical coordinates allows researchers to directly visualize the complex two-dimensional eigenmodes of piezoelectrically actuated thin plates, providing an experimental benchmark for validating numerical finite-element-analysis (FEA) structural models without requiring complex optical interferometry [23, 25].

1.4.2. Inverse Chladni Pattern in Water

When the vibrating planar structure is completely immersed in or covered by a liquid layer, such as water ($\rho_{water} \approx 1000$ kg/m^3), the kinematic behavior of the micro-particles undergoes a complete reversal. This phenomenon is known as the Inverse Chladni Pattern, where suspended microscale particles or biological cells migrate away from the structural nodal lines and aggregate precisely at the regions of maximum out-of-plane displacement the (antinodes) [26]. This behavior appears counterintuitive to classical wave mechanics but can be rigorously explained by analyzing the extreme hydrodynamic coupling and the boundary-driven acoustic streaming fields generated in highly viscous and dense fluid media [17].

In a liquid environment, the high-frequency harmonic deflection of the solid plate generates intense, localized pressure gradients within the adjacent fluid layer. As established by boundary-layer theory, the non-slip condition at the solid-liquid interface induces a highly energetic Schlichting viscous boundary layer [17,26]. The high density and viscosity of water relative to air amplify the Reynolds stresses within this boundary layer, driving dominant, high-velocity acoustic streaming vortices directly above the plate surface. These rotational vortices establish a steady fluid circulation that flows along the surface toward the antinodes, rises vertically into the bulk fluid, and returns along the upper boundaries toward the nodes [17, 18].

A microscale particle suspended within this liquid domain experiences a powerful

hydrodynamic Stokes drag force ($\langle F_{drag} \rangle = 6\pi\eta a \langle v_{str} \rangle$) dictated entirely by the local acoustic streaming velocity field ($\langle v_{str} \rangle$). For particles whose physical dimensions are significantly small (typically below a few hundred micrometers), their structural inertia is entirely dominated by this viscous drag force [18, 26]. The steady fluid streamlines within the viscous boundary layer sweep these micro-particles directly along the plate floor toward the antinodes. Once the particles reach the core of the antinodal domain, the vertical stagnation zones of the streaming cells trap them, resulting in highly localized, stable clusters at the maximum displacement zones [19, 26].

The transition between regular and inverse Chladni states serves as a powerful design tool in electro-acoustic systems. By strategically adjusting the liquid fluid height, the operating electrical frequency of the piezoelectric actuator, and the specific particle size parameters, the system can be precisely tuned. It can switch between collecting biological targets at the nodes (via direct inertial forces) or sorting micro-entities at the antinodes (via streaming drag forces), expanding the flexibility of multi-scale planar actuators in diagnostic and cell-handling applications [20, 26].

1.5. Mesoscale Structural Actuation vs. Micro-Acoustofluidic Devices

In contemporary lab-on-a-chip and particle manipulation setups, selecting the appropriate electromechanical actuation regime is strictly dictated by the operating frequency spectrum, the geometric scale of the fluidic chamber, and the primary physical force intended to govern the particle kinematics [8]. While high-frequency micro-acoustofluidic platforms operating in the megahertz (MHz) regime rely on Surface Acoustic Waves (SAWs) or high-order Bulk Acoustic Waves (BAWs) to establish true ultrasonic pressure fields within compressed fluid channels, these systems require sophisticated cleanroom micro-fabrication, specialized interdigital transducers (IDTs), and are often constrained to sub-millimeter micro-channels [8,20]. Conversely, when the system design transitions to macro- and mesoscale setups, such as standard laboratory Petri dishes or custom Plexiglas configurations, operation at lower frequency ranges (typically in the kilohertz, kHz regime) shifts the physical manipulation mechanism from bulk fluid acoustic fields to direct structural wave dynamics [23].

At these lower frequency bands, the acoustic wavelength within the fluid domain is significantly larger than the physical dimensions of the fluidic container, preventing the formation of traditional microscale standing acoustic pressure fields [10]. Instead, the converse piezoelectric effect excites low-frequency structural eigenmodes, inducing high-amplitude flexural (bending) waves that propagate throughout the solid substrate. Under this regime, suspended or resting micro-particles do not experience dominant direct ultrasonic scattering forces. Instead, their spatial manipulation is strictly governed by the accelerated boundary displacements of the solid surface and the localized hydrodynamic fields, manifesting as regular or inverse Chladni manipulation mechanisms [23, 26].

This low-frequency mesoscale structural actuation offers distinct engineering advantages for specific biomedical and electronic testing applications. It completely bypasses the need for complex lithographic fabrication, allowing robust particle and cell handling directly within conventional, low-cost standard off-the-shelf fluidic wells and Petri dish platforms [26]. Furthermore, by operating at kHz frequencies, the system minimizes the risks of extreme acoustic heating and cavitation, which are often detrimental to sensitive biological analytes in high-power MHz acoustic devices [5,20]. Understanding how these low-frequency structural vibrations seamlessly couple with adjacent fluids to generate predictable Chladni and inverse

Chladni Patterns provides a cost-effective, versatile framework. This bridges the gap between macro-scale piezoelectric components and precise mesoscale fluidic actuation, which forms the core experimental and numerical focus of the subsequent chapters of this work [5,23].

Chapter 2. Materials and Methods

2.1. Instrumental Configuration

The complete and high-precision characterization of advanced microfluidic dynamic systems and piezoelectrically actuated structures requires optical and electromechanical sensing frameworks capable of measuring nanoscale deformations and continuous frequency spectra without introducing mass-loading or invasive structural damping. In high-frequency microscale applications, such as MEMS acoustic transducers and micro-speakers, alternative architectural designs based on the converse piezoelectric effect have increasingly attracted substantial scientific attention [27]. These structures are particularly appealing for non-invasive over-the-counter (OTC) and specialized air-conduction hearing aids that operate seamlessly without the need for complex surgical implantation procedures, owing primarily to their highly compact dimensions, low energy consumption, batch fabrication compatibility, and low power requirements [28,29]. Regardless of the explicit geometric configurations or application boundaries, a piezo-actuated system typically features a thin, multi-layered vibrating membrane or structural diaphragm designed to couple mechanical energy into the surrounding medium [30].

A comprehensive engineering evaluation of these acoustic and structural devices involves quantifying the dynamic surface profile, out-of-plane mechanical displacement, and absolute frequency response across extended spectral bands. Traditionally, complete audio-frequency characterization requires evaluating parameters like the sound pressure level (SPL) from a few hundred Hz up to at least 10 kHz within heavily controlled, isolated acoustic chambers equipped with calibrated laboratory microphones and complex recording chains [31,32]. Nonetheless, highly critical preliminary insight into the structural and physical performance of the device can be efficiently acquired through direct, localized evaluations of its electro-mechanical frequency response and displacement sensitivity, which is defined as the absolute displacement-to-driving-voltage amplitude ratio ($\Delta S/\Delta V$) [32].

These preliminary microfluidic and structural evaluations are, however, often carried out using highly complex, bulky, and exceptionally costly commercial optical profiling systems. These setups typically combine multi-axis scanning optical heads with electrical measurement instrumentation and generally necessitate a direct, unobstructed view of the entire device microstructure, which limits their utility in encapsulated, closed-chamber, or microfluidic lab-on-a-chip networks [33,34]. For instance, Laser Doppler Vibrometry (LDV) is a widely established, classic technique utilized for high-precision, non-contact structural vibration measurements. However, it requires highly expensive optomechanical equipment, extensive maintenance, and delicate, real-time laser beam alignment on microscopic features [34]. Alternatively, micro-optical detectors integrating vertical-cavity surface-emitting lasers (VCSELs) and discrete photodiode arrays have been explicitly developed to measure minute out-of-plane displacements and rotations in integrated micro-actuators, but they demand highly customized fabrication and lack setup versatility [35].

In many experimental and practical testing cases, compact external optoelectronic configurations are strongly preferred for remote, non-invasive vibration and displacement detection. To address these multi-scale testing challenges, laser diode feedback interferometry (LDFI), also fundamentally known as Self-Mixing Interferometry (SMI), offers an exceptionally compact, robust, and cost-effective alternative. It is capable of measuring linear and non-linear physical displacements and instantaneous motion directions even when operating on rough, unpolished, or highly diffusive structural target surfaces [36, 37].

The primary instrumental configuration implemented in this work is schematically detailed and illustrated in the comprehensive structural architecture of Figure 2.1. Unlike traditional external optical setups (such as classical Michelson, Mach-Zehnder, or Fabry-Pérot interferometers) that rely heavily on a multitude of discrete optical components including external beam splitters, reference arms, and high-precision reference mirrors, the self-mixing interferometric configuration eliminates optomechanical complexity [37,38]. In an LDFI framework, the semiconductor laser diode itself operates simultaneously as the coherent light source and the high-sensitivity phase-sensing element, resulting in unparalleled systemic compactness and simplicity [38].

The physical mechanism governing the operational behavior of the self-mixing interferometer relies on the phenomenon of optical feedback. A coherent infrared laser beam emitted from the semiconductor package is directed through a focusing lens assembly toward the target surface in this setup, the recessed, vibrating piezo-MEMS diaphragm or fluidic plate boundary [39]. A fraction of the light backscattered or reflected from the moving structure re-enters the laser cavity through the same lens, re-coupling into the active optical gain medium. This back-injected light perturbs the internal cavity field, inducing a continuous modulation of the laser's carrier density, photon density, and consequently, its net output optical power and emission frequency [38,40].

Consequently, variations in the physical distance between the laser facet and the moving target surface are directly encoded as high-contrast modulations in the intensity and frequency of the laser package output. The internal monitor photodiode integrated within the standard commercial laser diode package converts these rapid optical power variations into a photocurrent (I_{pd}) [39,41]. As detailed in the schematic diagram (Figure 2.1), this photocurrent is routed into a high-speed, low-noise Transimpedance Amplifier (TIA) circuit, which performs a precise current-to-voltage conversion to yield a clean, measurable output voltage signal (V_{pd}).

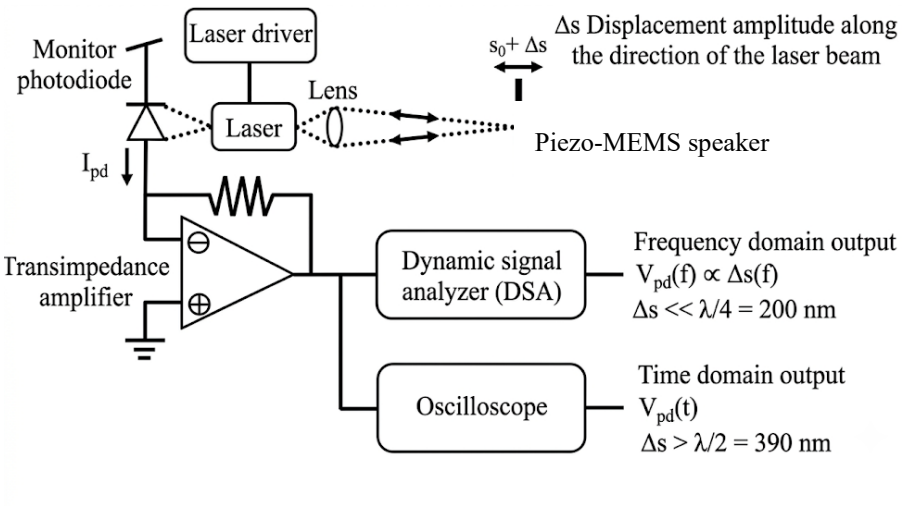


Figure 2.1. Instrumental configuration scheme of the laser diode feedback interferometer for piezo-MEMS speaker characterization. Δs represents the displacement amplitude along the direction of the laser beam. [60]

The core instrumentation framework is designed as a generalized, high-precision non-contact metrology platform capable of resolving out-of-plane micro-scale displacements across various target geometries, ranging from micro-electromechanical systems (MEMS) membranes to macroscopic continuous polymer plates. The architecture comprises several

integrated functional blocks. A commercial laser diode unit, driven by a highly stable, low-noise laser driver, generates the coherent optical beam. The laser emits at a nominal wavelength of λ_{laser}=780 nm. An adjustable focusing lens focuses the emitted light onto the reflective surface of the target structure (e.g., a piezo-actuated membrane or plate continuum.) The target is electrically excited using a function generator capable of supplying both broadband white noise and sinusoidal driving voltages. The amplified interferometric voltage output V_{pd} from the TIA is simultaneously routed into two parallel acquisition units depending on the target's operational displacement regime. The DSA is utilized primarily for small-amplitude linear displacements (Δs=200 nm), where the SMI operates within its linear fringe regime. The DSA extracts the frequency-domain spectrum and computes the empirical electromechanical transfer functions of the structural system. The oscilloscope is utilized for real-time time-domain tracking when the out-of-plane displacement exceeds the half-wavelength interferometric threshold causing the signal to exhibit non-linear fringe modulations. The oscilloscope captures the raw time-resolved interferometric waveforms for subsequent fringe-unwrapping processing.

The general mathematical expression for the detected time-varying self-mixing interferometric voltage signal V_{pd} derived from the perturbed optical field can be rigorously formulated as follows [40,42]:

$$V_{pd}(t) = V_{dc} + V_{MAX} \cos\left[\frac{4\pi}{\lambda_{laser}}\left(s_0 + \Delta s(t)\right)\right] \qquad (1)$$

Where V_{dc} is the dc components, V_{MAX} represents the maximum peak amplitude of the detected electronic signal (which scales directly with the optical feedback coupling coefficient, the surface reflectivity of the target, and the total electronic transimpedance gain of the TIA stage), λ_{laser} is the central emission wavelength of the laser diode, s_0 denotes the static, unperturbed laser-to-target distance, and $\Delta s(t)$ is the instantaneous out-of-plane displacement of the diaphragm relative to its equilibrium state.

To maximize the phase sensitivity of the interferometer to minute, sub-nanometric mechanical movements and ensure structural linearity, the optical system can be operated in the quadrature regime. The quadrature point corresponds to an exact operating condition where the absolute interferometer phase offset is positioned at the maximum slope of the cosine response curve [41]. By adjusting the static distance s_0 to establish an absolute phase offset equal to an odd multiple of ninety degrees (i.e. -90° or mπ/2), Equation (1) simplifies via trigonometric identities into an approximately linear sine function with respect to small displacements [42]:

$$V_{pd}(t) \propto V_{MAX} \sin\left[\frac{4\pi}{\lambda_{laser}}\Delta s(t)\right] \qquad (2)$$

In practical experimental configurations, maintaining stable operation around this highly sensitive quadrature point could be achieved through three complementary methods:

- Precisely adjusting the static laser-to-target distance via multi-axis micro-positioning stages to lock the optical phase at -90° relative to the internal reference cavity [39].
- Dynamically tuning the DC bias current or operational temperature of the laser diode to modulate the effective refractive index and phase shift within the active cavity [40].
- Employing external electronic filtering and active phase-shifting feedback circuits to continuously lock the output signal within the central linear region of the interferometric response [41].

It is worth noting that no additional advanced digital filters, hardware equalization, or post-processing algorithms were integrated into the experimental instrumentation setup. Instead, to maintain a straightforward and robust signal conditioning framework while effectively suppressing ambient environmental and electrical background noise, the data acquisition was governed strictly via an internal averaging technique. The real-time time-resolved waveforms on the digital oscilloscope and the power spectral density curves on the DSA were systematically averaged over multiple successive measurement cycles, successfully enhancing the signal-to-noise ratio (SNR) while preserving the pure, unaltered dynamic behavior of the vibrating target. To ensure structural isolation and eliminate external environmental noise, all experimental procedures were executed on a high-mass optical table equipped with active pneumatic vibration isolation legs, which effectively minimized low-frequency building vibrations and ambient acoustic disturbances [32]. The laser diode head was rigidly mounted on a three-axis (x, y, z) micro-positioning stage enabling fine spatial adjustments down to 0.1 μm resolution. This allowed the optical path to be aligned perpendicular to the target surface, optimizing the backscattered power coupled into the internal cavity. The absolute voltage output (V_{pd}) from the transimpedance circuit can be analyzed in frequency-domain using a Dynamic Signal Analyzer (DSA) or in time-domain with a digital oscilloscope.

2.1.1. Frequency Domain Analysis

The frequency-domain characterization framework within the self-mixing optoelectronic setup is systematically engineered to establish a rigorous, non-invasive methodology for mapping the linear electromechanical transfer function, tracking spatial mode shapes, and identifying the structural eigenvalues of the piezoelectrically driven diaphragm. In structural mechanics and micro-acoustofluidics, evaluating the frequency response under low-amplitude excitation is a fundamental prerequisite for isolating pure elastic behavior from non-linear structural dampening or high-order boundary perturbations [7]. As mathematically established by the first-order Taylor series expansion of the electromagnetic cavity modulation phase, when the instantaneous out-of-plane mechanical displacement amplitude (Δs) is strictly confined to a tiny fraction of the coherent emission wavelength $\Delta s << \lambda_{laser}/4$ the complex, multi-harmonic sinusoidal response of the photodetector output simplifies into an isolated linear relationship [41, 42]:

$$V_{pd}(t) \propto V_{MAX}\left(\frac{4\pi}{\lambda_{laser}}\Delta s(t)\right) \propto \Delta s(t) \qquad (3)$$

This small-displacement operational regime is exceptionally advantageous for conducting continuous, broadband spectral sweeps, as it ensures that the photodetected signal reflects only the true mechanical velocity and displacement fields without introducing complex optical fringe-counting errors or phase-wrapping ambiguities. To implement this characterization methodology, the piezoelectric micro-actuator is electrically stimulated using a broadband electrical white noise signal [32]. This excitation signal is digitally generated with a completely flat and constant power spectral density across the entire target frequency spectrum selected for the structural investigation [43]. The root-mean-square (RMS) amplitude of the applied driving noise voltage is regulated to guarantee that the resulting

structural deformations of the thin membrane remain firmly locked within this linear small-displacement window throughout the active testing duration.

The electrical excitation signal is delivered to the target piezoelectric transducer through a dedicated, low-noise coaxial transmission line configuration connected directly to a shared system ground and the active electromechanical terminal, thereby minimizing parasitic capacitive coupling and electromagnetic interference from the surrounding laboratory environment [29]. To capture and analyze the resulting electromechanical response, the analog output voltage ($V_{pd}(f)$) from the high-speed transimpedance amplifier circuit is routed directly into the analog input channels of a multi-channel Dynamic Signal Analyzer. The data acquisition configuration within the DSA is optimized to maximize the systemic signal-to-noise ratio (SNR) and eliminate stochastic experimental artifacts or thermal noise fluctuations. This is achieved by executing complex ensemble power spectral density averaging over a series of independent measurement tracks, where the frequency resolution, windowing functions (such as Hanning or Flat-Top windows), and total spectral lines are configured to the absolute hardware limits of the acquisition instrument [32].

To comprehensively map the spatial dependency and continuous geometric distribution of the structural mode shapes across the bounded elastic domain, a multi-point spatial scanning methodology is implemented. The compact optoelectronic head, which houses both the semiconductor laser diode and the primary focusing lens assembly, is rigidly clamped to a three-axis micro-positioning stage [39]. The focused laser spot is manually translated on the vibrating structure surface [32]. At each discrete spatial coordinate, the broadband power spectrum is acquired by the DSA. This scanning routine enables the localized tracking of frequency response variations of the device under test. This provides the comprehensive empirical dataset necessary for calculating the system's dynamic compliance and validating numerical finite-element analysis (FEA) structural models before transitioning the experimental campaign into large-displacement time-domain investigations.

2.1.2. Time-domain Analysis

When the electrical driving voltage applied to the piezoelectric actuator is systematically increased beyond the nanometric regime, the mechanical structure transitions into a large-displacement domain where the out-of-plane vibrational amplitude exceeds half the laser emission wavelength $\Delta s > \lambda_{laser}/2$. Under these operational conditions, the time-domain photodetected signal captured on the digital storage oscilloscope no longer exhibits a linear analog mapping of the displacement. Instead, it develops a rapid succession of periodic macroscopic voltage oscillations widely designated as interferometric fringes [41, 42]. These high-contrast fringes are physically generated by the continuous alteration of constructive and destructive optical interference states within the active semiconductor cavity as the external target surface sweeps across multiple half-wavelength boundaries of the propagating optical field.

Due to the non-linear coupling of back-injected photons returning from a diffusive, unpolished, or highly scattering structural target, the raw photodetected time-domain waveform assumes a heavily distorted, asymmetrical cosine or sawtooth-like geometry rather than a pure mathematical sinusoid [36, 40]. Crucially, the local slope and directional asymmetry of these interferometric fringes maintain a strict, mathematically predictable one-

to-one correspondence with the instantaneous direction of motion of the vibrating structure [36]. This unique physical property of laser diode feedback interferometry completely eliminates the classic sign ambiguity and direction-blindness that inherently plagues conventional single-beam optical setups, enabling autonomous tracking of forward and backward mechanical trajectories [37].

Figure 2.2 shows representative examples of the driving sinusoidal signal $V_{dr}(t)$ and the corresponding photodetected signal $V_{pd}(t)$, measured at the center of the vibrating diaphragm of the piezo-MEMS speaker acquired at three different driving frequencies. In these acquired signals, the optical feedback effect introduces a clear asymmetry where the sharp transitions appear as downward slope, indicating an increasing laser-target distance as the membrane pulls back. The orientation and steepness of these fringe transitions directly depend on the direction of displacement for this specific device setup.

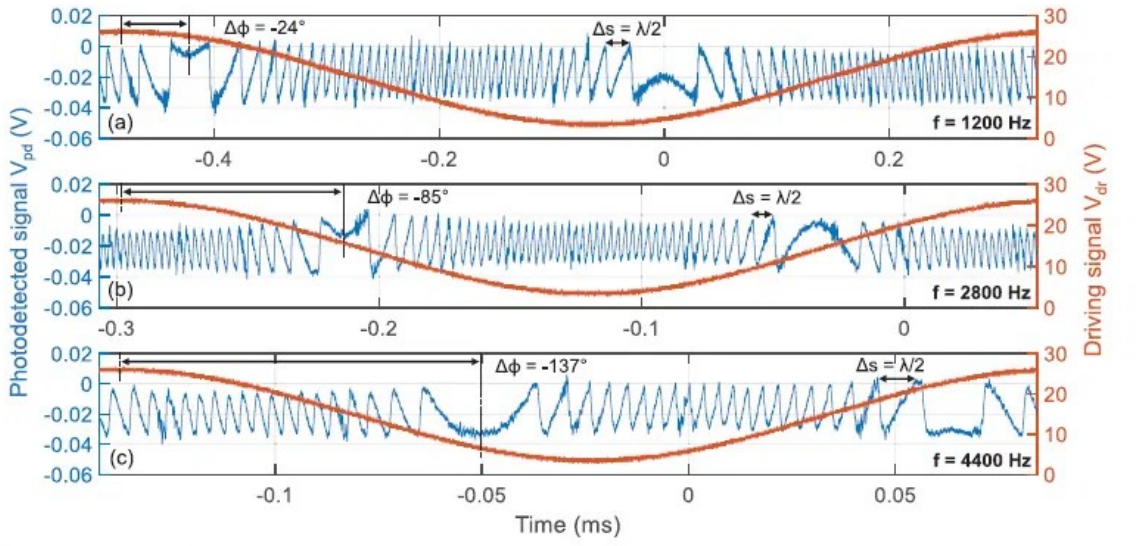


Figure 2.2. Driving sinusoidal signals V_{dr} (red traces) and photodetected output signals V_{pd} (blue traces) exhibiting distorted interferometric fringes due to optical feedback, acquired at three different frequencies on piezo-MEMS speaker (a) 1200 Hz; (b) 2800 Hz; (c) 4400 Hz. [60]

This fringe asymmetry can be directly exploited to reconstruct the target displacement, as illustrated in Figure 2.3. By identifying the fringe maxima (corresponding to $\lambda_{laser}/2$ displacement steps) and fitting a sinusoidal curve to their time sequence, the actual displacement waveform of the target can be recovered, as shown for the f = 2800 Hz case.

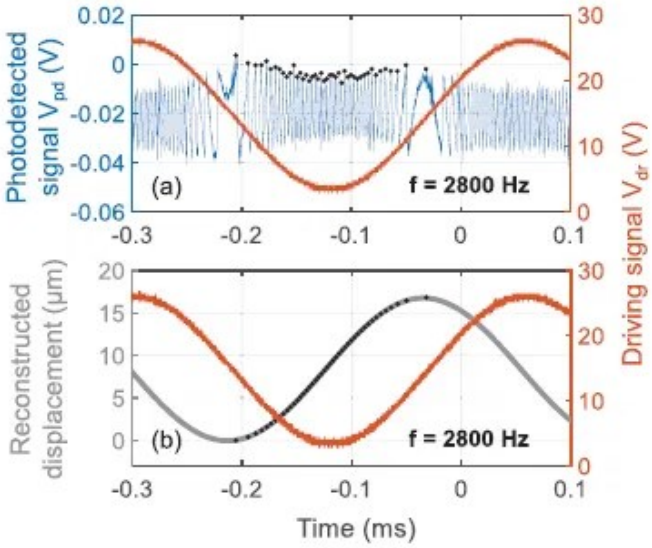


Figure 2.3. Displacement amplitude reconstruction: (a) signal reported in Figure 2.2b, in which black markers indicate the maxima of the interferometric fringes (blue trace), characterized by downward transitions with a significantly greater steepness than upward transitions (as laser–target distance increases); (b) sinusoidal curve (grey trace) that best fits the time sequence of $\lambda_{laser}/2$ moving steps (black markers), obtained by setting the reconstructed displacement frequency equal to the driving frequency (f = 2800 Hz). [60]

The directional extraction from the fringe asymmetry is governed by the following electromechanical and optoelectronic boundary principles:

Downward Steeper Transitions When the time-domain interferometric waveform displays a sharp, near-vertical downward transition from a local peak to the adjacent voltage minimum with a slope that is significantly steeper than the subsequent upward recovery phase, it mathematically indicates a progressively increasing absolute laser-to-target physical distance [36]. In the physical domain, this asymmetric signature demonstrates that the surface under test is currently being pulled backward by the converse piezoelectric lattice stress, migrating away from the optical head toward its maximum negative displacement boundary [42].
Upward Steeper Transitions Conversely, when the photodetected waveform exhibits sharp upward transitions characterized by a positive slope that is drastically steeper than the downward decay phase, it demonstrates a rapidly decreasing laser-to-target physical distance [42]. This optoelectronic state signifies that the surface under test is expanding or pushing outward toward the laser facet, moving through positive displacement coordinates.
To reconstruct the continuous physical displacement profiles and extract precise phase information relative to the input electrical signal, the raw time-domain voltage tracks captured by the digital oscilloscope are exported and processed using custom numerical algorithms executed in MATLAB. Because each consecutive interferometric fringe step corresponds to an absolute geometric displacement increment of exactly half the emission wavelength $\lambda_{laser}/2$, an automated fringe-identification and sinusoidal-fitting routine is executed. The numerical algorithm first identifies the motion inversion points where the structural movement halts and reverses direction, causing the fringe frequency to drop to zero. Then, it determines the temporal coordinates of the fringe maxima between these turning boundaries. Finally, rather than performing simple fringe counting or integration, the algorithm fits a target-frequency sinusoidal curve to the time sequence of the λ_{laser} /2 moving steps, accurately yielding the peak-to-peak displacement amplitude and phase delay without sub-fringe truncation errors [60]. The continuous displacement waveform ($\Delta s(t)$) is subsequently calibrated and smoothed

by executing a non-linear numerical fitting routine that matches a steady sinusoidal motion model to the discrete λ_{laser} /2 step sequences [32]. To accurately quantify the mechanical phase delay ($\Delta\Phi$), both the input driving voltage waveform and the photodetected optical response were captured simultaneously on the oscilloscope at identical sampling rates. At the exact natural frequency of a system, the presence of double complex-conjugate poles in the electromechanical transfer function mathematically dictates a structural phase shift ($\Delta\Phi$) of either -90° or -270°, depending on the direction of motion and the spatial coordinate of the measurement point relative to the driving boundary [32, 43].

2.2. Numerical Simulation

To complement the experimental optoelectronic characterization and provide a deep physical understanding of the multi-physics phenomena occurring within the systems under study, a rigorous three-dimensional (3D) Finite Element Analysis (FEA) framework was developed. Numerical simulations are essential in piezoelectric and acoustofluidic research to visualize acoustic pressure fields, mechanical stress distributions, and fluid-particle interactions that cannot be easily captured via direct experimental imaging [44]. All numerical models in this work were implemented using COMSOL Multiphysics, a versatile commercial software platform explicitly designed for solving coupled systems of partial differential equations (PDEs) through space-discretized finite elements.
The simulation workflow was executed in a hierarchical, multi-stage architecture to ensure mathematical convergence and isolating individual physical mechanisms before coupling them. The mesh generation utilized a combination of structured swept meshes for planar layers and highly dense, unstructured tetrahedral elements near geometric singularities, sharp fluidic boundaries, and solid-fluid interfaces where high gradient fields develop. Independent mesh convergence studies were systematically conducted based on the generalized expression $h_{mesh} \leq \lambda_{acoustic}/6$ to guarantee that the spatial discretization error did not artificially perturb the structural or acoustic eigenvalues.

2.2.1. Mechanical Analysis

In the COMSOL Multiphysics platform, structural vibrations and physical deformations are simulated using the dedicated Solid Mechanics interface. The simulation methodology begins with the construction of precise Three-Dimensional (3D) geometric models that replicate the exact physical dimensions, thickness profiles, and multi-layer structural layouts of the devices used in the experimental laboratory setup. To ensure high numerical accuracy, the geometry is discretized into a dense computational mesh. This mesh utilizes structured swept elements for the flat planar layers and localized unstructured tetrahedral elements around sharp boundaries, edges, and contact zones where high mechanical stress gradients naturally develop. A continuous mesh convergence study is systematically implemented by refining the element sizes until the calculated natural frequencies stabilize, guaranteeing that the spatial discretization size does not introduce numerical errors or artificially perturb the simulated structural behavior.
To mathematically represent the real-world mounting conditions and physical assembly configurations of the experimental framework, specific boundary conditions are applied to the boundaries of the simulated structures. First, a Fixed Constraint boundary condition is

assigned to the outermost peripheral edges and anchoring regions where the physical devices are clamped to the rigid laboratory evaluation boards. By forcing the mechanical displacement vector to zero (u=0), this condition prevents any translation or rotation at the clamping boundaries, matching the rigid structural limits of the physical setup. Second, a Free Boundary condition is assigned to all active, exposed, and vibrating surfaces, such as the top faces of the thin Plexiglas plates, the petri dishes, and the microchannel walls. This allows these structural domains to vibrate completely unrestricted in the out-of-plane direction when subject to dynamic mechanical excitation.

To compute the structural response within this multi-physics model, an Eigenfrequency Study Solver is implemented. This specialized numerical solver automatically calculates the structural eigenvalues (natural frequencies) and maps the corresponding two-dimensional mode shapes of the continuous system. A primary function of this analysis is to directly locate the zero-displacement coordinates across the vibrating surfaces, which mathematically define the structural nodal lines $W(x,y)=0$. By analyzing these simulated modal patterns, the software provides a clear structural map showing how the vibration amplitudes change from the center to the edges. These computed lines establish the exact physical baselines needed to predict where regular and inverse Chladni patterns will form, creating a strong link between the numerical model and the subsequent experimental investigations.

2.2.2. Electromechanical Analysis

Following the extraction of the structural eigenvalues, the numerical framework in COMSOL Multiphysics was expanded to analyze the full multi-physics behavior of the devices through the integrated Piezoelectricity interface. This section establishes the comprehensive methodology for evaluating the direct electromechanical transduction of the system. In this stage of the simulation, the focus shifts from analyzing pure mechanical vibrations to understanding how an applied external electrical field is transformed into active mechanical lattice stress and physical deformation via the converse piezoelectric effect [4]. This coupled simulation is essential for replicating the real-world operational behavior of piezoelectric micro-actuators, where the structural movement is driven entirely by electrical signals rather than external mechanical forces.

To implement this electromechanical coupling within the software, the Solid Mechanics interface is dynamically linked with the Electrostatics module. This allows the program to solve for mechanical displacements and electrical field distributions simultaneously within the multi-layer piezoelectric domains [47]. To accurately replicate the actual electrical excitation framework utilized in the laboratory experiments, specific electrical boundary conditions must be assigned to the thin electrode surfaces of the modeled piezoelectric materials. First, an Electric Potential boundary condition is applied directly to the active driving electrode terminal, representing the alternating current (AC) harmonic voltage signal supplied by the function generator. Second, a Ground boundary condition is assigned to the opposing shared counter-electrode. This configuration establishes a controlled electrical potential gradient across the thickness of the piezoelectric ceramic lattice, driving the electromechanical simulation.

The electromechanical model is computed using a Frequency Domain Study Solver in COMSOL. By systematically sweeping the driving frequency across the experimental bands, the software calculates the steady-state mechanical response of the thin membrane under a constant voltage input. This numerical analysis allows for the direct extraction of the device's displacement sensitivity, which is measured as the absolute out-of-plane displacement amplitude per volt of electrical excitation (μm/V). Additionally, the solver tracks the complex

capacitive admittance and the exact structural phase delay across the geometry. This provides a highly accurate method for evaluating how efficiently the electrical energy is converted into physical surface motion before introducing fluid layers or tracking individual particle movement.

2.2.3. Particle Tracing

The final and most comprehensive stage of the numerical part is dedicated to evaluating the dynamic trajectories, transport mechanisms, and spatial accumulation of discrete micro-particles within different structural platforms. This analysis is executed using the specialized Particle Tracing for Fluid Flow interface in COMSOL Multiphysics, which operates by coupling the pre-computed mechanical vibrations and acoustic velocity fields into a Lagrangian particle tracking framework. To systematically investigate these physics across multiple geometric scales, the computational workspace is divided into three distinct physical platforms based on the experimental setups: the macroscale Planar Plexiglas Plate, the mesoscale Laboratory Petri Dish enclosure, and the highly confined Microfluidic Channel network. Each layout is carefully designed in the software to study how structural deformations directly or indirectly guide suspended matter.

A critical methodology implemented in this simulation campaign involves studying the systems under two completely different environmental conditions: Dry Conditions (without water) and Wet Conditions (fully filled with water). This comparative approach is essential for isolating the specific physical forces that govern particle kinematics. Under dry conditions, the fluidic domain is entirely deactivated within the software, meaning the micro-particles interact directly with the vibrating solid surfaces. Conversely, under wet conditions, a full multi-physics coupling is achieved through the Acoustic-Structure Interaction interface. In this configuration, the out-of-plane flexural waves of the solid boundaries compress the adjacent liquid, generating acoustic pressure fields and high-velocity rotational fluid vortices known as acoustic streaming inside the Petri dish and microfluidic domains.

Even though the operating frequency framework implemented in this study falls within the low-frequency (kHz) acoustic spectrum, which is lower than the ranges (MHz) commonly utilized for direct acoustic radiation trapping, the physical coupling between the vibrating structure and the fluid domain is rigorously modeled utilizing the Pressure Acoustics interface in COMSOL Multiphysics. In this low frequency regime, the acoustic wave interaction within the liquid layer predominantly drives boundary-driven acoustic streaming fields rather than dominant primary acoustic radiation forces. Therefore, invoking the acoustic multiphysics module is mathematically and physically required to compute the localized acoustic pressure gradients and fluid velocity vectors that form the baseline for the subsequent particle tracing simulations.

In the simulation setup, after the background structural and acoustic fields reach a steady-state condition, thousands of model micro-particles are mathematically released into the computational domains. The software tracks the time-resolved position of each individual particle by solving Newton’s second law of motion, computing how the total net force vector changes the particle's velocity over time. The mathematical definitions of the active forces are automatically modified depending on the medium defined in the model. In the wet (liquid) configurations, the particles experience a constant competition between the primary Acoustic Radiation Force, which drives them based on their material density and compressibility relative to water, and the fluidic Stokes Drag Force exerted by the boundary-driven Rayleigh streaming vortices. In the dry configurations, these fluid forces are omitted, and the model

focuses on mechanical contact dynamics, where particles bounce along the surface due to the localized acceleration gradients of the plate.

To ensure the simulation closely matches realistic laboratory scenarios, the particle parameters such as absolute diameter, mass density, and initial spatial distribution are explicitly adjusted within the COMSOL interface to mimic real granular materials and biological entities. The time-dependent solver is configured with fine temporal steps to accurately capture the rapid momentum changes during surface impacts or vortex trapping. By executing these high-resolution tracking routines, the simulation provides a visual representation of how particles migrate over time to form regular Chladni patterns at the vibrationless nodes in dry environments, or inverse Chladni patterns at the high-amplitude antinodes in liquid environments. Therefore, by evaluating the dynamic balance and spatial domination of these coupled fields, the simulation explicitly demonstrates how the suspended matter strictly follows the predictable geometric rules of both classical Chladni and reversed Chladni patterning regimes. This complete numerical methodology serves as a predictive tool for validating the electromechanical sorting and trapping efficiency observed throughout the experimental phases of this work.

Chapter 3. Multiscale Characterization of Piezoelectrically Actuated Planar Structures for Acoustic Application

3.1. MEMS Speaker (Micromachined Acoustic Transducer)

As discussed in Section 2.1, MEMS microspeakers based on the converse piezoelectric effect are attracting increasing attention for compact, low-power, batch-fabricated, non-invasive air-conduction hearing-aid applications [44–46]. Beyond commercially available solutions, numerous studies have introduced novel designs and implementations of piezo-actuated micro-transducers [47, 48, 49]. Regardless of the specific geometric configuration, a piezo-driven microspeaker typically relies on a flexible vibrating diaphragm that displaces the surrounding air medium to generate sound waves [50, 51]. As detailed in Section 2.1, laser diode feedback interferometry (LDFI), or self-mixing interferometry (SMI), was selected over alternative non-contact techniques (LDV, VCSEL-based sensors) for its compactness and its ability to measure absolute displacement and motion direction on diffusive surfaces [52, 53, 54]. In this thesis, the LDFI methodology was explicitly implemented to evaluate the out-of-plane vibration behavior of a commercial thin-film piezo-MEMS speaker manufactured by USound [55, 56], which was mounted securely inside a specialized acoustic enclosure [57]. A small oval aperture on the front panel of the housing provides the coherent laser beam with direct access to the recessed internal diaphragm. The high-sensitivity optical setup consists of a piezo-MEMS speaker mounted on a sample holder and a laser diode interferometer, as shown in the photograph of Figure 3.1. The detection chain including the transimpedance amplifier (TIA) and oscilloscope follows the same schematic architecture described in Chapter 2 (Figure 2.1).

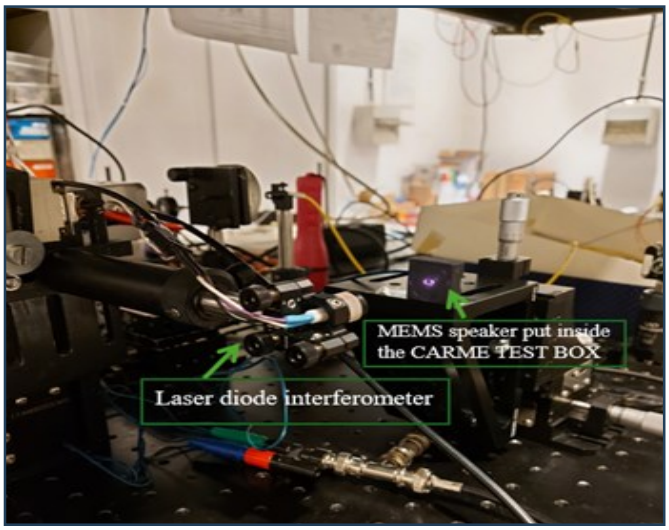


Figure 3.1. Photo of the experimental setup

During operation, the coherent beam emitted from the semiconductor laser diode impinges almost perpendicularly onto the vibrating surface. A fraction of the backscattered light, modulated by the out-of-plane displacement, re-enters the active laser cavity. This optical feedback perturbs the internal laser field, encoding variations in the target distance into intensity modulations captured by the integrated monitor photodiode. As discussed in Section 2.1, for small-amplitude vibration regimes, the interferometer is operated near the quadrature point to ensure a linear relationship between the photodiode output voltage and the diaphragm displacement.

3.1.1. Spectral Response

In the regime of small mechanical displacements ($\Delta s << \lambda/4$), the interferometric response is proportional to the displacement. This operational window is highly advantageous for frequency-domain measurements, where the piezo-actuator is driven by a broadband electrical excitation such as white noise with a constant power spectral density across the band of interest allowing the electromechanical frequency response to be efficiently extracted through Fast Fourier Transform (FFT) analysis of the photodetected signal. This approach permits the precise identification of the resonant frequencies.
To obtain the electro-mechanical frequency response of the micro-speaker, the photo-detected signal V_{pd} was recorded in the frequency range of 0–25 kHz using a Dynamic Signal Analyzer (DSA). To facilitate electrical connectivity, the MEMS device was connected to a commercial on-chip driving board (provided by company INVENTVM), with dedicated output pins routed to the recording instruments as shown in Figure 3.2. To extend the structural analysis and map the spatial distribution of the vibrations, five independent measurement tracks were acquired under identical white-noise excitation settings (configured with 100 signal averages, a frequency span of 25.6 kHz, and 1600 spectral lines, yielding a frequency resolution of 16 Hz.). The five tracks correspond to distinct laser focal coordinates across the chip surface: center (Position p_3), Position p_4, Position p_5, Position p_2, and Position p_1, as comprehensively mapped in Figure 3.3.

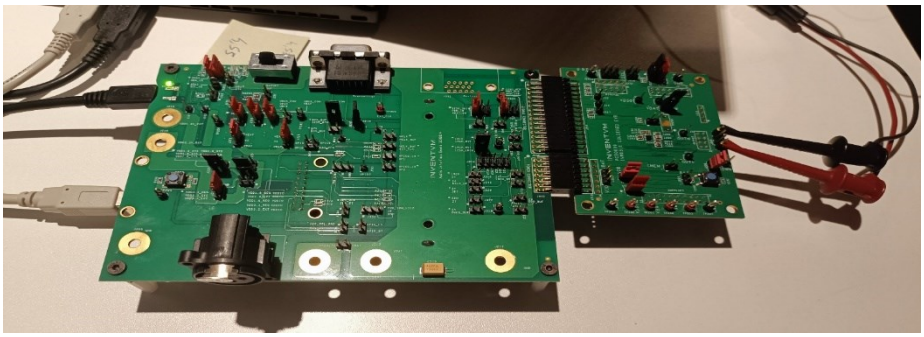


Figure 3.2. MEMS speaker driving board provided by company INVENTVM.

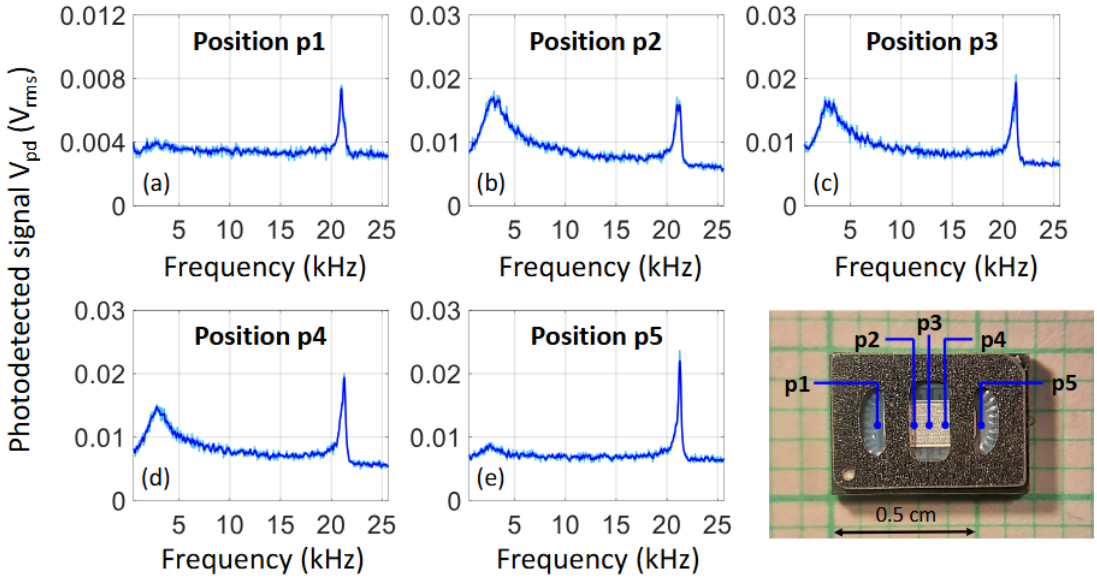


Figure 3.3. Photodetected signal V_{pd} measured directing the laser beam toward center p_3 and positions p_4, p_5, p_2, p_1 and acquired as a function of the frequency in the band 0 Hz – 25 kHz when the MEMS is driven with electrical white noise.

The experimental frequency-domain curves demonstrate that the mechanical vibration modes are non-uniformly distributed across the multi-layer diaphragm structure. The spectral results reveal the clear presence of two primary out-of-plane mechanical resonance peaks within the monitored bandwidth. There is a low frequency resonance at f≈2.8 kHz, this peak is observed uniformly across all measured scanning positions. It exhibits a broad spectral profile with a low-quality factor indicating a heavily damped behavior that matches the nominal manufacturer specifications for stable acoustic audio reproduction [58]. The spatial scanning indicates that this mode induces a larger displacement at the geometric center (Position p3) and decays toward the outer boundary clamping, confirming it as a symmetric first-order bending mode.

The other resonance at f≈21.7 kHz is located immediately above the upper frequency threshold of human hearing; this second mechanical mode is characterized by a significantly higher Q factor revealing an underdamped structural response that produces a sharp, sensitive spectral spike. While this underdamped mode does not directly affect the linear acoustic broadcasting band, it expected to influence the device performance primarily through its contribution to localized harmonic distortion and mechanical stability under high-stress excitation.

3.1.2. Time domain response: Displacement and Phase Delay

The piezo-MEMS loudspeaker was further characterized in the time domain across the entire swept frequency range. For each discrete driving frequency, the photodetected fringe maxima each corresponding to a λ/2 displacement step were tracked, and a sinusoidal curve, with frequency constrained to the known driving frequency, was fitted to the resulting time sequence. The displacement amplitude and phase delay with respect to the driving voltage were both extracted from this fit. Normalizing the displacement amplitude by the corresponding driving signal amplitude at each frequency yields the displacement sensitivity. To supplement the broadband white-noise characterization and gain deeper insights into the

dynamic behavior of the device around its fundamental resonance zone, a targeted discrete frequency sweep investigation was executed. While the coherent laser beam remained focused precisely at the geometric center of the piezo-MEMS diaphragm, the mechanical system was driven by continuous sinusoidal voltage signals. As graphically illustrated in Figure 3.4a, the photodetected voltage output (V_{pd}) exhibits distinctive asymmetric fringe patterns generated by the continuous phase modulation of the back-injected light.

To quantify this movement, the individual fringe maxima were calculated; the black markers highlighted in Figure 3.4b precisely indicate these tracked fringe maxima. These specific mathematical markers display sharp, asymmetric downward transitions with a slope that is noticeably steeper than the corresponding upward paths. In the physical framework of self-mixing interferometry, this directional slope asymmetry confirms that the piezoelectric lattice is experiencing a synchronized phase contraction, thereby pulling the diaphragm backward to its maximum distance relative to the optical head.

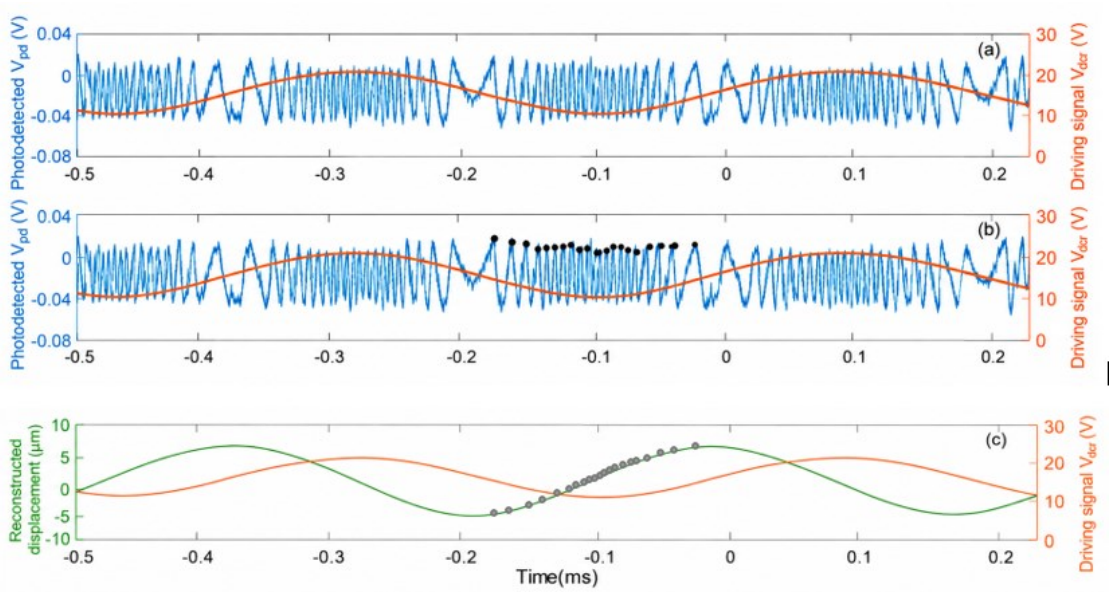


Figure 3.4. (a). Driving sinusoidal signals V_{dr} (red traces) and photodetected output signals V_{pd} (blue traces) exhibiting distorted interferometric fringes due to optical feedback, acquired at the frequency 2.8 kHz (b). Fitted driving sinusoidal signals (red trace) and photodetected output signal (blue trace) (c). Reconstructed displacement at frequency equal to the driving frequency (f = 2.8 kHz).

As plotted in Figure 3.4c, this best-fit sinusoidal curve was achieved by constraining the reconstructed mechanical frequency to be identical to the active driving frequency f=2.8kHz. The peak-to-peak physical displacement amplitude was then directly extracted from this optimized fitted curve, ensuring high quantitative precision and establishing a robust verification link between the small-signal white-noise spectrum and large-signal sinusoidal frequency response characterization. To map the operational transfer function, the displacement sensitivity in μm/V (defined as the ratio between the extracted mechanical displacement amplitude and the driving voltage amplitude) and the concurrent phase delay ($\Delta\Phi$) were calculated across a sweeping frequency range of 0–5 kHz around the first mode.For each individual frequency step during this sweep, the raw optoelectronic interferometric signal captured by the integrated monitor photodiode was recorded via the digital oscilloscope and subsequently exported for post-processing in MATLAB. A sinusoidal driving voltage with the amplitude of 2.85 V was applied to the MEMS speaker through the on-chip driving board of INVENTVM company, with the laser beam focused near the center. On-chip board supplies

a differential driving signal, whose effective amplitude delivered to the actuator is approximately twice that of the single-ended signal supplied by the external generator. As summarized in Figure 3.5, due to the highly overdamped nature of the system, the maximum displacement sensitivity (reaching approximately 0.75 µm/V) occurs at a frequency lower than the natural resonance frequency. At the exact natural frequency (2.8 kHz), the double complex-conjugate poles governing the mechanical system transfer function [59] induce a precise phase delay shift of -90° or -270° depending on the vector coordinate orientation.

The Figures 3.5 (a), (b) present the electro-mechanical frequency response of the piezoelectric MEMS speaker over the range of approximately 400 Hz to 4800 Hz, comprising two coupled plots that together characterize the behavior of the device around its first resonance. In the Figure 3.5a, the diaphragm displacement (blue curve, in µm) and the driving signal amplitude (purple curve, in V) are shown as functions of frequency. Although the driving amplitude was kept approximately constant (about 5.7 V), the measured displacement increases progressively with frequency, reaching a maximum of nearly 4 µm in the range of roughly 2000–2400 Hz; this region corresponds closely to the first resonance frequency reported for the device around 2.8 kHz beyond which the displacement gradually decreases. In the Figure 3.5b, the displacement sensitivity (red curve, in µm/V) and the phase delay (green curve, in degrees) are plotted as functions of frequency. The displacement sensitivity follows a trend similar to that of the displacement itself, rising to a maximum value of approximately 0.75 µm/V near 2200–2400 Hz before decreasing sharply at higher frequencies. Because the first resonance is overdamped, this peak in sensitivity occurs at a frequency slightly lower than the natural resonance frequency, consistent with the theoretical behavior of a damped second-order mechanical system. Concurrently, the phase delay decreases steadily with increasing frequency, from about 0° at lower frequencies to nearly −150° at the higher end of the range, which is the expected signature of passing through a damped mechanical resonance characterized by a pair of complex-conjugate poles. Overall, this figure provides a comprehensive picture of the linear frequency response of the MEMS speaker driving by the board with the chip around its first resonance

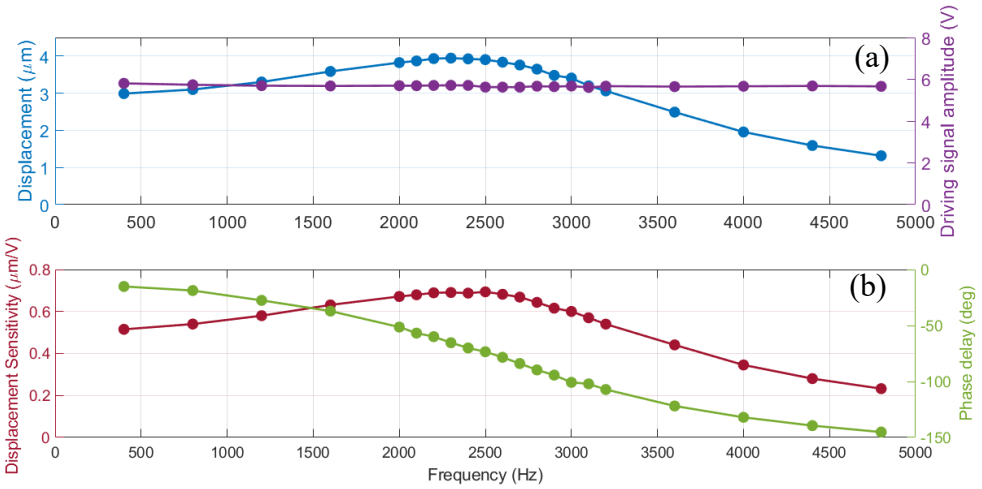


Figure 3.5 (a) Displacement (blue data) and driving signal amplitude (purple data), (b). displacement sensitivity (red data) and phase delay (green data) as functions of the frequency with sweeping frequency around the first resonance frequency 2.8 kHz.

To further investigate the system's electrical performance and validate the structural mode shapes, a comparative analysis was executed between two distinct actuation approaches: generating the driving signal via the on-chip commercial board and supplying it externally through a signal generator, keeping the voltage fixed at 2.85 V peak-to-peak at the first resonance frequency (2.8 kHz). The spatial distribution of the vibration amplitude was mapped in fine steps by translating the laser spot across the surface coordinates. As detailed in the time-domain summary in Figures 3.6a and 3.6b, driving with the chip demonstrates the displacement sensitivity centered around 0.75µm/V with a flat phase delay of -90° across the central coordinates. Similarly, the external signal generator exhibits an identical spatial profile with the same sensitivity baseline (around 0.75 µm/V).

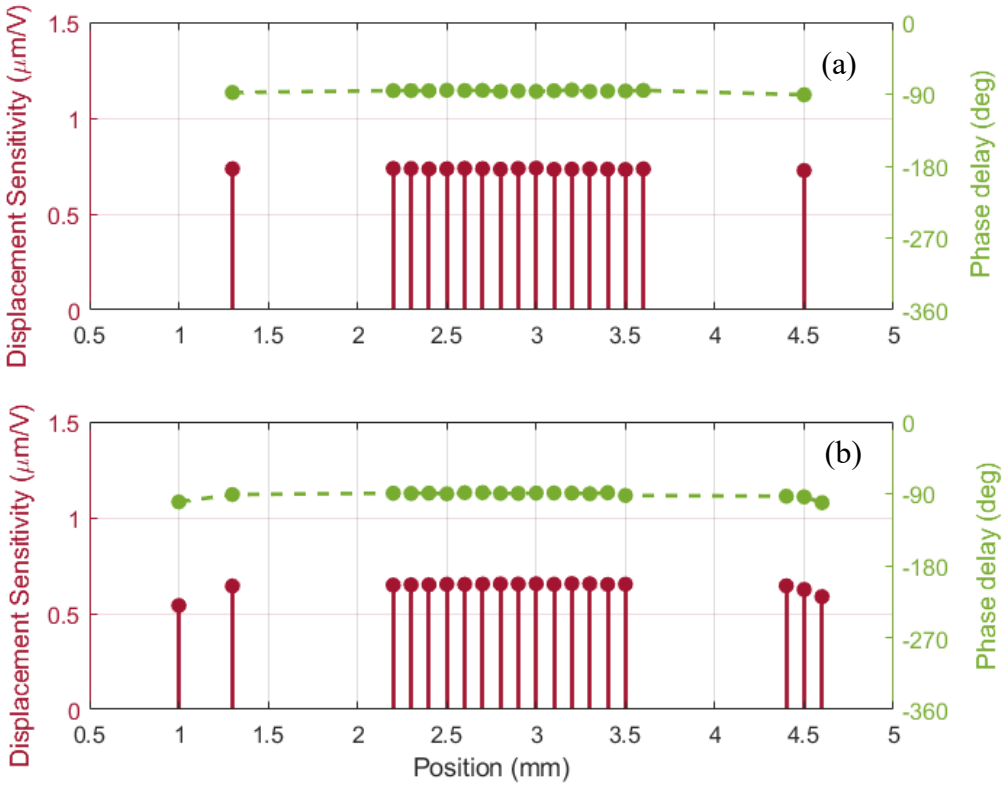


Figure 3.6 (a) Displacement sensitivity (red data) and phase delay (green data) as a function of laser position at the first resonance frequency 2.8 kHz while driving with signal generator, (b) displacement sensitivity (red data) and phase delay (green data) as a function of laser position at the frequency 2.8kHz while driving with the board.

Finally, the spatial scanning routine was repeated for the high-frequency underdamped second resonance mode (21.7 kHz). The excitation voltage was reduced to a small-signal amplitude 4V peak-to-peak. The laser position on the diaphragm surface was systematically varied from 2.4 mm to 3.7 mm in precise 0.1 mm increments. As reported in Figures 3.7a and 3.7b, the extracted spatial profile reveals a strong, highly dynamic spatial dependency around the second resonance: the displacement sensitivity drops sharply from 0.4 µm/V at the boundary coordinates down to a minimum of 0.18 µm/V near the internal coordinates (3.3 mm), accompanied by severe localized phase delay fluctuations shifting rapidly from -260° to -210°.

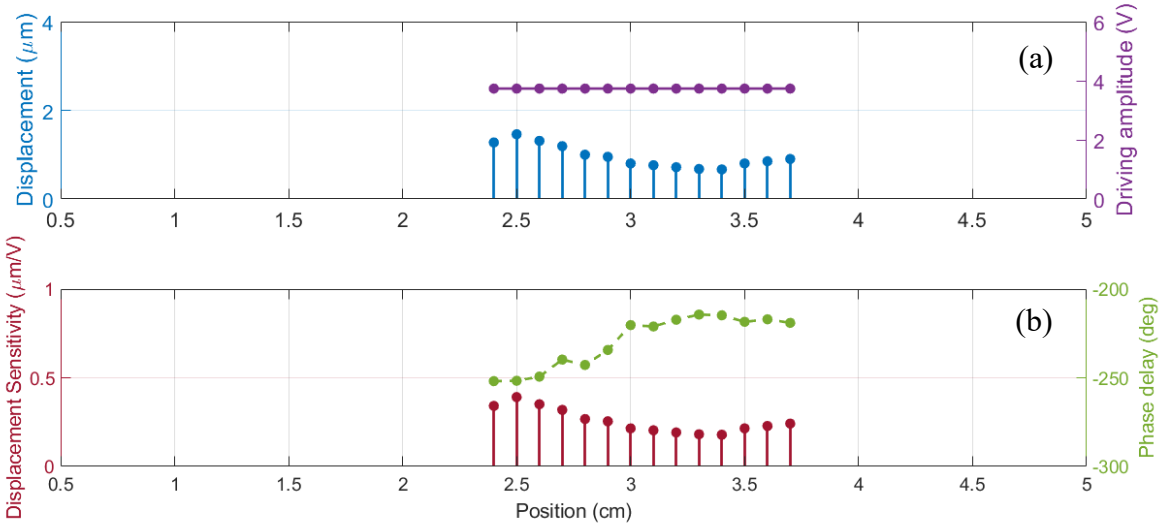


Figure 3.7. (a) Displacement (blue data) and driving signal amplitude (purple data), (b) displacement sensitivity (red data) and phase delay (green data) as a function of laser position range from 2.4 mm to 3.7 mm at the second resonance frequency 21.7 kHz.

3.2. Macro-Scale Structural Dynamics

Piezoelectric actuators are widely utilized in Structural Health Monitoring (SHM), precision mechanics, and active vibration control due to their inherently high operational bandwidth, compact physical dimensions, fast response times, and exceptional ability to efficiently convert electrical energy into precise mechanical deformation [60]. A precise and comprehensive understanding of the complex dynamic vibration behavior of piezo-actuated plate structures such as the one investigated in this chapter is absolutely essential, characterization, and systematic optimization of advanced sensing and actuation systems. In the foundational article entitled "Assessment of Vibration Frequencies of Piezo-Actuated Plate by Model Assisted Self-Mixing Interferometry", the authors effectively combine experimental SMI measurements with analytical modeling to accurately identify the specific vibration frequencies of a thin plate structure actuated by a securely bonded piezoelectric element [60]. This part directly adapts the core concepts, methodologies, and principles introduced in that seminal work and integrates them with a comprehensive, three-dimensional finite element modeling (FEM) strategy performed using the advanced capabilities of COMSOL Multiphysics. The ultimate aim of this macro-scale investigation is to reproduce, validate, and extensively extend part of that dynamic analysis by numerically evaluating and experimentally validating the natural frequencies, structural mode shapes, and electromechanical resonance behavior of a piezo-actuated Plexiglas plate.

The primary structure considered in this section is a Plexiglas plate characterized by a uniform density of 1180 kg/m^3. The nominal geometric dimensions of this thin Plexiglas sheet are specified as 152mm×101mm×1mm. The plate material exhibits a Young's modulus situated within the range of 2.5GPa to 3.5GPa, and a Poisson's ratio evaluated between 0.25 and 0.37. To introduce controlled mechanical excitation into the continuum, a rectangular piezoelectric ceramic material with known piezoelectric coefficients (d_{ij}), dielectric permittivity matrix (ε_{ij}), and elastic compliance constants (s_{ij}) is mechanically bonded directly to the plate. The spatial dimensions of this active piezoelectric patch are configured as 40mm×30mm×0.8mm. To

guarantee high fidelity in the numerical model and replicate physical conditions, the interface bonding layer is explicitly incorporated within the 3D computational domain. The bonding interface consists of a double-sided adhesive tape featuring a physical thickness of 0.12 mm. The isotropic mechanical properties of this viscoelastic adhesive layer specifically a Young's modulus of 6.5MPa, a structural density of 570 kg/m^3, and a Poisson's ratio of 0.25 are integrated into the Solid Mechanics framework of the COMSOL model to prevent artificial stiffness overestimation and accurately capture the shear-lag energy transfer phenomena between the actuator and the Plexiglas substrate. This comprehensive geometric and material configuration ensures that both the passive mechanical modal parameters and the forced electromechanical frequency response curves under electrical driving signals are captured with high numerical stability, allowing for a rigorous, high-fidelity quantitative comparison against the non-contact experimental self-mixing interferometric measurements. Figure 3.8 provides a detailed schematic and structural layout illustrating the explicit dimensions of the Plexiglas plate as deployed within the experimental test frame. The relative positioning, coordinate alignment, and surface area boundaries of the centrally bonded piezoelectric patch are clearly designated, serving as a synchronized geometric reference for both the finite element mesh discretization and the subsequent spatial laser readout scans.

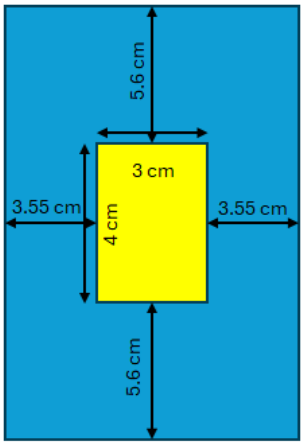


Figure 3.8. Schematic representation of the plexiglass plate. The piezoelectric actuator (yellow) is attached to the bottom side of the Plexiglas plate (blue).

3.2.1. Spectral Response

Figure 3.9 illustrates the experimental arrangement utilized for measuring the out-of-plane physical displacement and analyzing the continuous dynamic characteristics, including the natural and resonant frequencies of the continuous Plexiglas plate. The optical technique employed throughout this macro-scale investigation is SMI, which is based on directly monitoring the internal optical power fluctuations of a semiconductor laser diode.

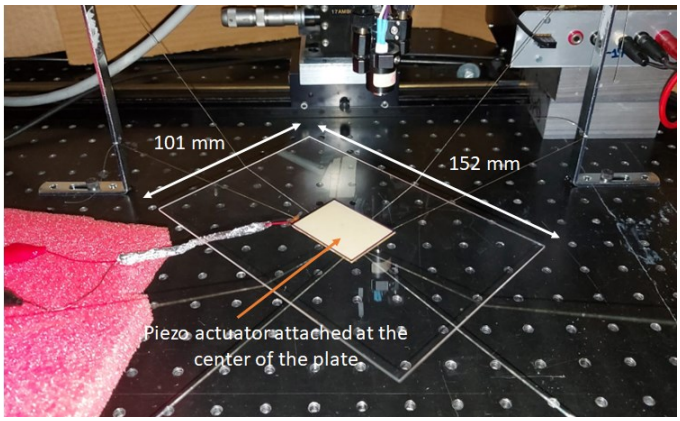


Figure 3.9 Photograph of the plexiglass plate suspending on the nylon wires

As demonstrated in the photograph provided in Figure 3.9, the Plexiglas plate was horizontally suspended inside the testing frame using fine nylon wires attached to its outer corners. This low-constraint mounting mechanism successfully replicates the ideal free-free boundary conditions defined in the corresponding numerical model, eliminating parasitic structural damping and ensuring that the recorded resonance peaks strictly reflect the intrinsic natural eigenvalues of the continuous polymer plate. Figure 3.10 reports the experimental photodetected spectral response acquired at three representative positions on the plate (corner, short edge, and long edge).

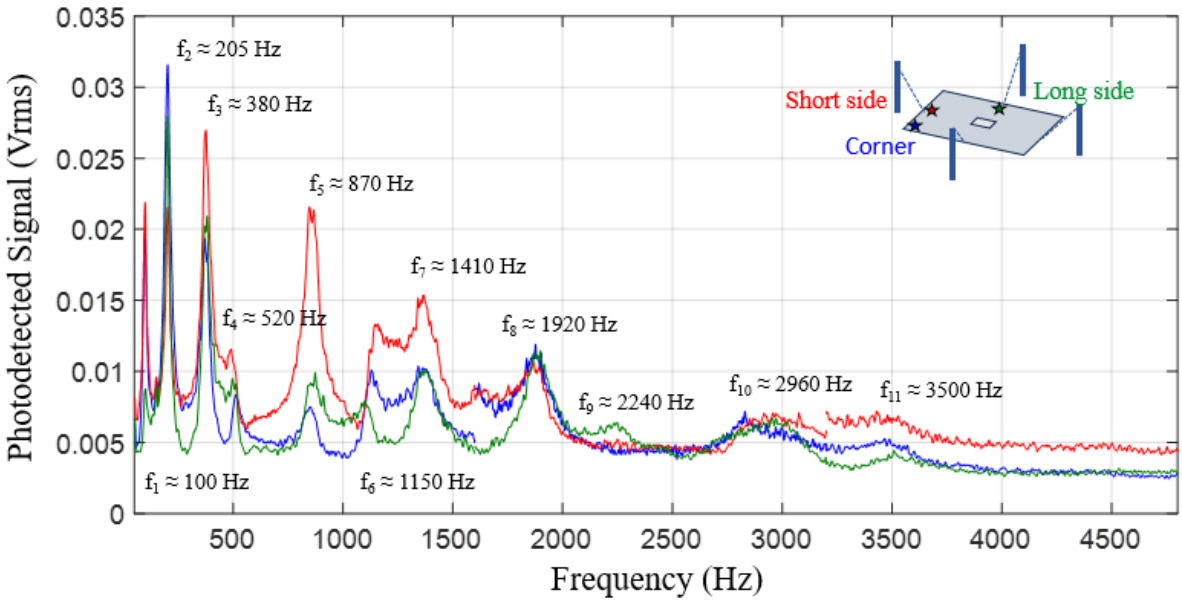


Figure 3.10. Experimental multi-modal voltage power spectra of the suspended Plexiglas plate up to 4.5 kHz, captured via broadband noise excitation across three tracking coordinates to resolve the discrete structural resonance frequencies (f_1 to f_{11}).

3.3. Numerical Simulation Results

To establish a rigorous predictive validation platform and corroborate the experimental self-mixing interferometric data, a comprehensive three-dimensional finite element modeling (FEM) campaign was executed within the COMSOL Multiphysics environment. This numerical framework is systematically organized into two sequential modeling phases: a pure

mechanical analysis followed by a fully coupled electromechanical multiphysics evaluation, accurately replicating the geometric boundaries, material transformations, and dynamic responses of the active piezo-structure.

3.3.1. Physics

To thoroughly evaluate the structural behavior and progressive coupling of the coupled system, the numerical simulation workflow was divided into two distinct simulation stages, implementing specific physics configurations for each phase. In the initial phase of the simulation, the focus is placed entirely on the intrinsic structural dynamics of the uncharged system. This stage utilizes the Solid Mechanics interface in isolation, treating both the Plexiglas substrate and the passive ceramic patch as continuous elastic domains. By solving the structural tensor equations of motion under zero external load and excluding all electrical fields, this phase is dedicated exclusively to executing an Eigenfrequency Study. The purpose of this mechanical solver is to determine the natural frequencies (eigenvalues) and map the fundamental shape of the structural modes (eigenvectors) inherent to the physical plate continuum.

Mechanical Modal Analysis

In the initial phase of the simulation, the focus is placed entirely on the intrinsic structural dynamics of the uncharged system. This stage utilizes the Solid Mechanics interface within COMSOL Multiphysics to find the natural frequencies of the structure. The isotropic material parameters of the Plexiglas substrate plate are defined with a Young's modulus of nominal 3 GPa and a Poisson's ratio of 0.35. To replicate the physical free-free testing configuration, in which the Plexiglas plate is suspended by four thin nylon wires attached at its corners, the wires are represented in the Solid Mechanics model as point-applied spring foundations at the four corner points, defined in COMSOL through a general (non-diagonal) symmetric spring-constant matrix k_p = [[0, 100, 0], [100, 0, 0], [0, 0, 300]] N/m in the global coordinate system, applied identically at all four corners. The off-diagonal terms account for the in-plane shear coupling introduced by the oblique orientation of the suspension wires, while the diagonal term k_{zz} = 300 N/m governs the out-of-plane restoring stiffness. These stiffness values are negligible compared to the bending stiffness of the Plexiglas plate itself, so that the springs provide only the minimal numerical constraint required to remove the rigid-body singularity in the eigenfrequency solver without perturbing the computed natural frequencies. To determine the natural frequencies (eigenvalues) and map the fundamental shape of the structural modes (eigenvectors) inherent to the physical plate continuum, an Eigenfrequency Study was implemented in this mechanical phase. By solving the unconstrained structural tensor equations of motion under zero external load and excluding all electrical fields, this study step provides the essential natural frequencies of the system. The computed intrinsic mode shapes and their respective three-dimensional surface deformation profiles for the first eight eigenvalues are graphically presented in Figure 3.11.

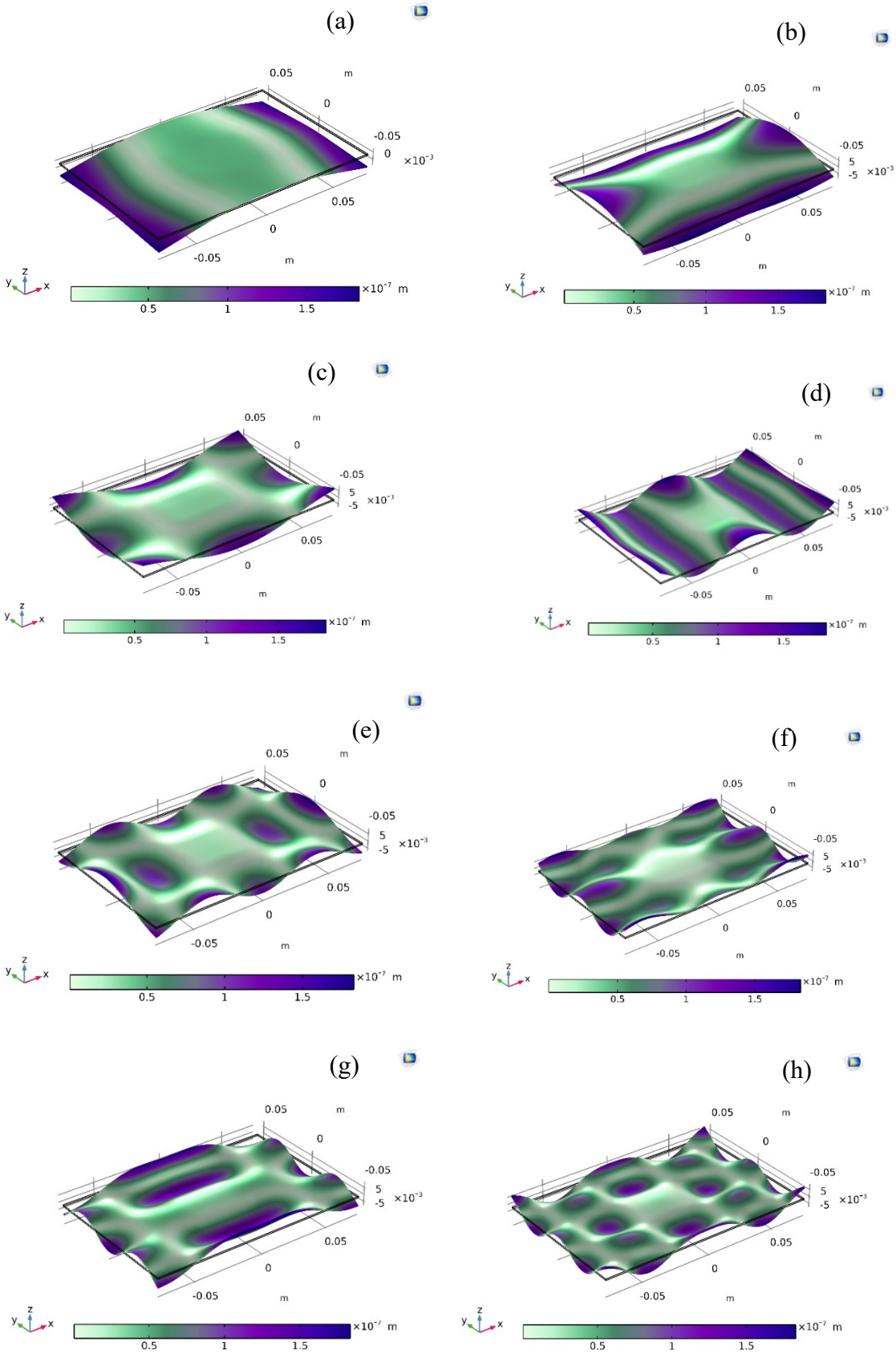


Figure 3.11. Simulated mechanical mode shapes of the plexiglass plate obtained via COMSOL Multiphysics: (a) f_1=101.36Hz, (b) f_2=194.23Hz, (c) f_3=338.67Hz, (d) f_4=451.53Hz, (e) f_5=735.55Hz, (f) f_6=949.11Hz, (g) f_7=1195.1Hz, (h) f_8=1578.2Hz

The experimental macroscopic validation of the continuous structural mode shapes and dynamic topologies was qualitatively and quantitatively corroborated utilizing full-field Chladni pattern visualizations. Figure 3.12 graphically illustrates the experimentally captured particle deposition patterns on the vibrating Plexiglas surface under harmonic piezoelectric actuation, serving as a direct physical representation of the operational deflection shapes.

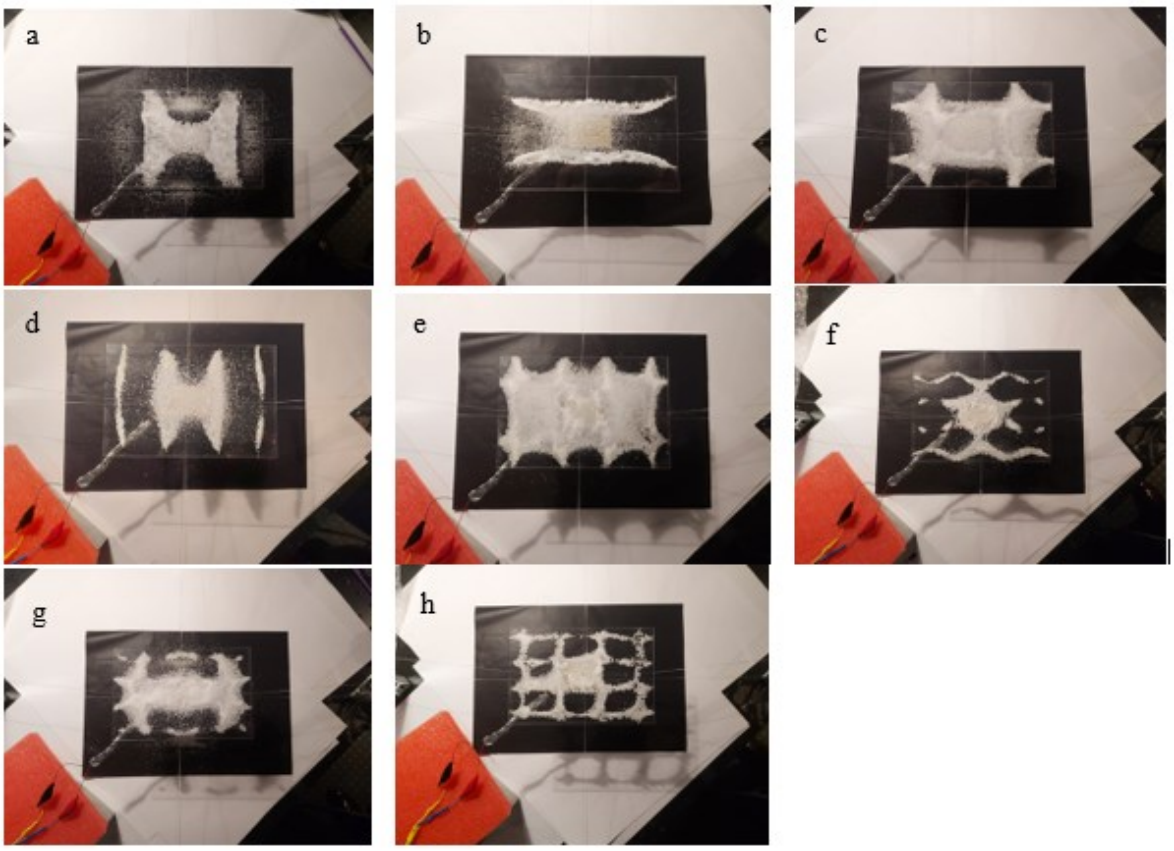


Figure 3.12. Experimental Chladni patterns formed by particle deposition along the structural node lines of the suspended Plexiglas plate under discrete harmonic piezoelectric actuation at (a) f_1=100Hz, (b) f_2=205Hz, (c) f_3=380Hz, (d) f_4=520Hz, (e) f_5=870Hz, (f) f_6=1150Hz, (g) f_7=1410Hz, (h) f_8=1920Hz

Electromechanical Frequency Response Analysis

Once the mechanical eigenvalues were established, the simulation transitioned to a multi-field coupling framework to capture the operational performance of thepiezo-actuated panel. In this phase, the Solid Mechanics interface is coupled with the Electrostatics interface, which is assigned to the active volume of the piezoelectric patch to govern the internal electric potential and displacement vector field. These parallel domains are linked via the Piezoelectric Devices multiphysics interface, which solves the linear stress-charge and strain-charge constitutive matrices of the piezoelectric. This setup accurately models the inverse piezoelectric effect, where applied electrical fields induce in-plane strains that drive out-of-plane flexural bending. In contrast to the first phase, this stage executes a Frequency Domain Study step, simulating the steady-state harmonic response of the electrically excited plate across a broadband sweep to identify forced resonance peaks.

3.3.2. Boundary Conditions

Replicating realistic physical constraints within the virtual finite element environment is the best way to prevent artificial stiffness overestimation and numerical frequency shifts. The structural coupling between the Wisol4030 and the plate is explicitly resolved by modeling the thin double-sided adhesive tape layer as a continuous elastic domain. This interface layer is assigned to a physical thickness of 0.12 mm, a localized density of 570 kg/m^3, a Young's modulus of 6.5 MPa, and a Poisson's ratio of 0.25, allowing for an accurate representation of the shear-lag energy transfer phenomena. For the electrical domain utilized in Phase 2, appropriate boundary conditions were applied to the actuator electrodes: the bottom bonding interface of the Wisol4030 patch was set to a Ground boundary condition (V = 0), while a harmonic AC voltage terminal with an amplitude of 5V was applied to the top electrode surface to drive the frequency domain simulation. Because combined electromechanical models and high-frequency flexural modes exhibit strong localized strain gradients, a rigorous mesh convergence analysis was conducted to ensure grid-independent solutions. A structured, layer-refined mesh strategy was applied to the piezoelectric and adhesive domains, forcing the maximum element size to remain below 1/4 of the layer thickness. The global mesh density was systematically swept across three distinct refinement levels (Normal, Fine, and Finer) until the relative variation in successive natural frequencies obtained from the Eigenfrequency Study dropped well below a strict convergence threshold of 0.1%, eliminating artificial frequency shifts and providing a highly stable, converged baseline for subsequent experimental cross-validation.

3.4. Comparison of Numerical and Experimental Results

As explicitly demonstrated by the experimental evidence in Figure 3.12, the geometric coordinates of the nodal lines where the micro-particles accumulate due to zero localized out-of-plane acceleration exhibit an exceptional spatial correlation with the continuous zero-displacement contours predicted by the finite element eigenfrequency analysis in COMSOL Multiphysics. The high-fidelity convergence between the virtual mode shapes and the physical Chladni sedimentations securely verifies that the structural constraints, boundary conditions, and material anisotropy implemented within the numerical framework replicate the physical continuum with high accuracy.

The primary structural eigenvalue, corresponding to the fundamental symmetric bending configuration, yields a minimal relative error well within acceptable engineering tolerances. For the higher-order flexural modes, the minor, progressive spectral shift observed in the physical laboratory testing is physically justified by the mass-loading effect of the granular visualization particles, real-world acoustic radiation impedance against the ambient fluid medium, and micro-scale viscoelastic dissipation within the polymer lattice mechanisms that are idealized as conservative in the un-damped numerical domain. Ultimately, this comprehensive validation framework confirms that the model-assisted characterization strategy acts as a robust predictive platform. The excellent quantitative agreement across both the spatial deflection topologies (Chladni patterns) and the discrete spectral peaks demonstrates that the coupled 3D multiphysics model accurately captures the dynamic transfer functions of the system, establishing a reliable baseline for utilizing the suspended piezo-actuated Plexiglas plate as an efficient flat-panel acoustic radiator.

Figure 3.13 presents the numerical frequency-domain characterization of the Plexiglas plate

reports the corresponding natural frequencies computed via the COMSOL Multiphysics eigenfrequency solver. Table 3.1 provides a direct numerical comparison between the experimentally identified resonance peaks and the numerically predicted eigenfrequencies across the full evaluated bandwidth, showing good overall agreement between the simulated and measured modal response of the structure.

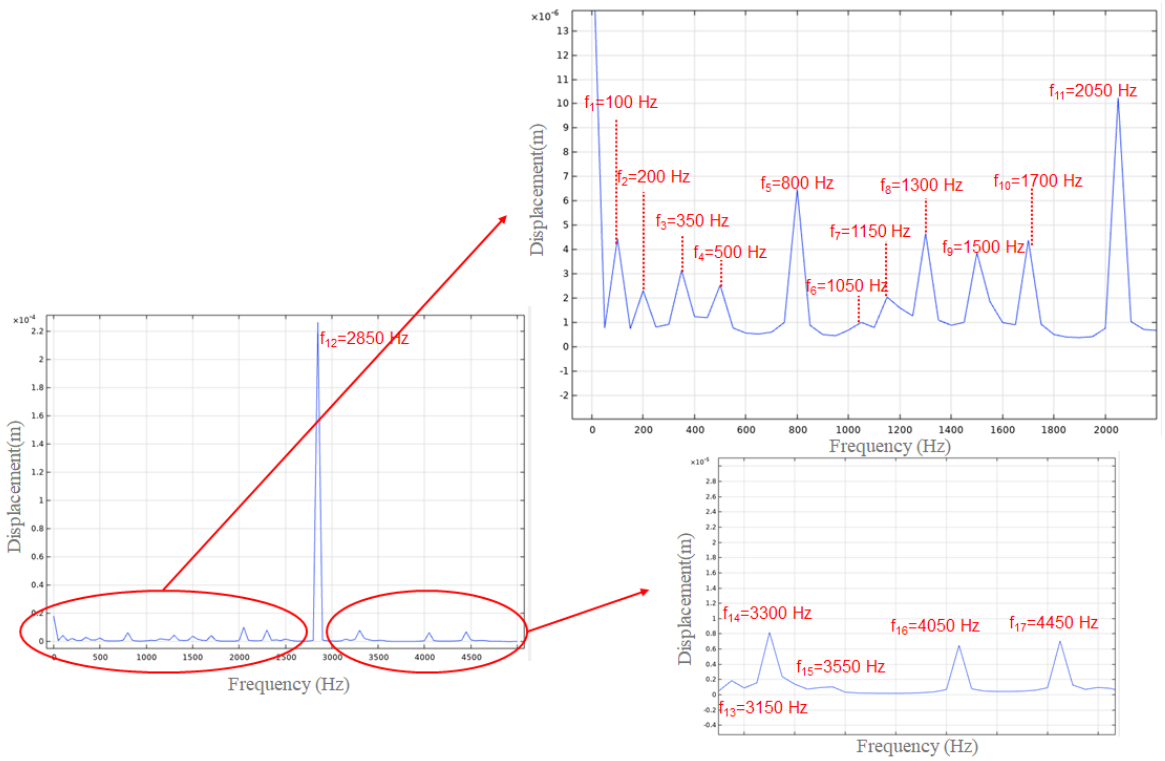


Figure 3.13. Numerical electromechanical frequency response spectrum of the piezo-actuated Plexiglas plate computed via COMSOL Multiphysics

Table 3.1. Comparison between experimentally identified resonance peaks and numerically predicted (COMSOL) eigenfrequencies of the Plexiglas plate.

Mode	**Experimental (Hz)**	**Numerical – COMSOL (Hz)**	**Difference (%)**
f_1	100	101.36	1.34%
f_2	205	194.23	5.25%
f_3	380	338.67	10.8%
f_4	520	451.53	13.16%
f_5	870	735.55	15.45%
f_6	1150	949.11	17.46%
f_7	1410	1195.1	15.24%
f_8	1920	1578	17.8%

Overall, the comparison between numerical and experimental results confirms that the COMSOL based finite element model provides a reliable representation of the plate's dynamic behavior. As shown in Table 3.1, the discrepancy between the simulated and measured resonance frequencies remains minimal for the lower-order modes, indicating that the fundamental structural parameters (geometry, boundary conditions, and material properties) were accurately captured in the numerical model. However, as the mode order increases, the relative error between the numerical and experimental frequencies becomes progressively larger, which can be attributed to the cumulative influence of higher-order effects such as mass loading from the visualization particles, fluid-structure damping, and local viscoelastic losses that are not fully accounted for in the idealized, undamped numerical framework. This trend suggests that while the model remains highly accurate for predicting the fundamental behavior, additional refinement particularly regarding damping mechanisms would be beneficial for improving accuracy at higher frequencies.

Chapter 4. Particle Manipulation in a Petri Dish Using Piezoelectric Actuation

4.1. Introduction and Platform Overview

Building on the self-mixing interferometric characterization methodology and the finite-element modeling framework established in Chapter 2, this chapter applies the same experimental and numerical toolset to a new target geometry: a piezo-actuated Petri dish intended for the acoustic manipulation and density and size-based sorting of suspended micro-particles. The Petri dish combines a rigid circular side wall with a thin, piezoelectrically driven bottom, allowing a liquid medium to be enclosed directly above the vibrating surface. This geometry is representative of a broader class of lab-on-a-chip and point-of-care platforms in which acoustically induced streaming and Chladni-type nodal patterning are exploited to trap, concentrate, or separate particles without any moving mechanical parts. The commercial Petri dish used in this work has an outer diameter of 58 mm, an inner diameter of 56 mm, an internal cavity height of 14 mm, and an external wall height of 17 mm, as shown in Figure 4.1. A rectangular piezoelectric actuator is bonded to the outer face of the dish bottom, following the same actuation scheme described for the Plexiglas plate in Section 3.2. Two operating conditions were considered: the dish empty (dry condition) and the dish filled with water up to approximately half of the internal cavity height (~7 mm, wet condition), consistent with the dry and wet modeling.

During experiments, the dish was filled with water to a level of 7 mm, corresponding to approximately half of the dish's inner height, as illustrated in Figure 4.2. This water level was chosen to ensure sufficient volume for particle suspension while maintaining a stable standing-wave pattern.

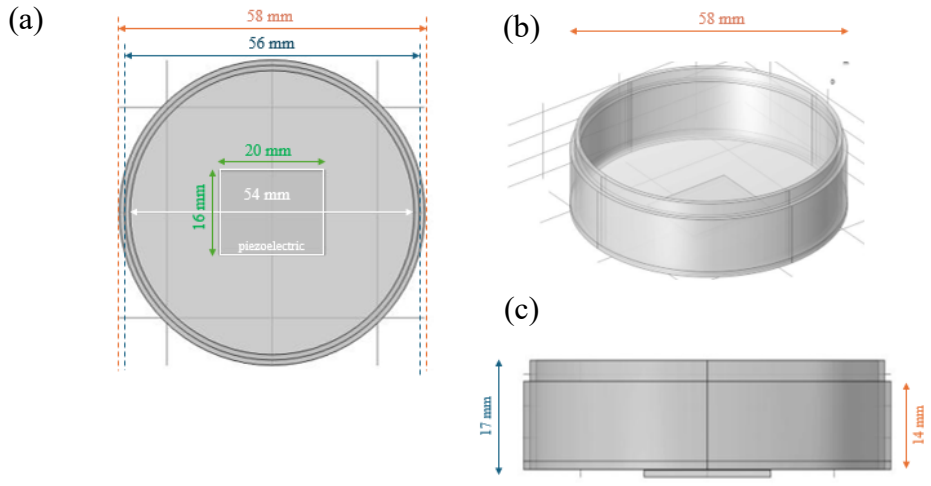


Figure 4.1. Geometry and dimensions of the Petri-dish resonator as implemented in the COMSOL model: (a) top view showing outer/inner diameter and actuator footprint; (b) isometric view of the assembled dish; (c) front view showing the external wall height (17 mm) and the internal cavity height (14 mm) used for the water-filled condition.

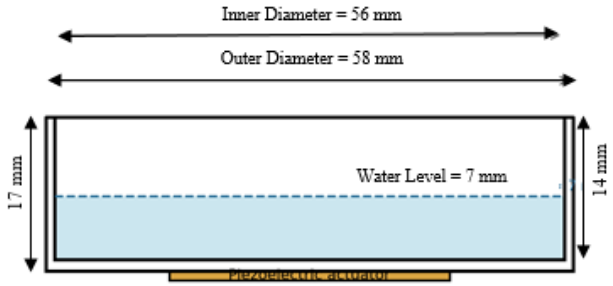


Figure 4.2. Cross-sectional schematic of the Petri dish, showing the bonded piezoelectric actuator and the water level used in the wet-condition tests.

Numerical eigenfrequency and electromechanical frequency-response results were obtained in COMSOL Multiphysics. These are compared with the experimental spectral, time-domain, and Chladni-pattern results of Section 2.1 to evaluate the platform's particle-sorting performance.

4.2. Numerical Results

4.2.1. Mechanical Simulation

The purely mechanical eigenfrequencies of the Petri dish were extracted using the Solid Mechanics interface and the Eigenfrequency Study Solver described in Section 2.2.1, applied here to the specific Petri-dish. Simulations were repeated for the dry and water-filled conditions, with the water volume treated as an added-mass fluid domain coupled to the vibrating bottom, in line with the acoustic-structure coupling strategy of Section 2.2.3. Table 4.1 summarizes the resulting eigenfrequencies in the dry and water-filled condition. Filling the cavity with water lowers the fundamental frequency from 1203.3 Hz to 978 Hz, reflecting the added-mass loading of the liquid layer on the vibrating bottom.

Table 4.1. Mechanical eigenfrequencies of the Petri dish for the dry and water-filled conditions.

Condition	Fundamental frequency	Higher-order frequency
Dry (empty)	1203.3 Hz	6611.6 Hz
Water-filled (~7 mm)	978 Hz	—

Figure 4.3 shows the corresponding mode shapes for the dry condition. The fundamental mode at 1203.3 Hz (Figure 4.3a) is a classical axisymmetric bending mode, with a single displacement antinode at the center of the dish (dark purple) that decays smoothly outward through a sequence of concentric rings toward the clamped rim, where the displacement vanishes; the black rectangle marks the footprint of the bonded piezoelectric actuator, which lies well within the central antinode and is therefore well positioned to excite the mode. The higher-order mode at 6611.6 Hz (Figure 4.3b) is markedly more structured: in addition to an outer set of concentric nodal rings, a distinct elliptically shaped antinode region appears directly above the actuator footprint, reflecting the non-axisymmetric influence of the rectangular actuator on this higher-order mode shape. Figure 4.4 shows the fundamental mode of the water-filled dish at 978 Hz, which retains the same axisymmetric, single-antinode

topology as the dry fundamental mode (Figure 4.3a); this confirms that the added mass of the surrounding water lowers the resonance frequency without altering the underlying mode shape.

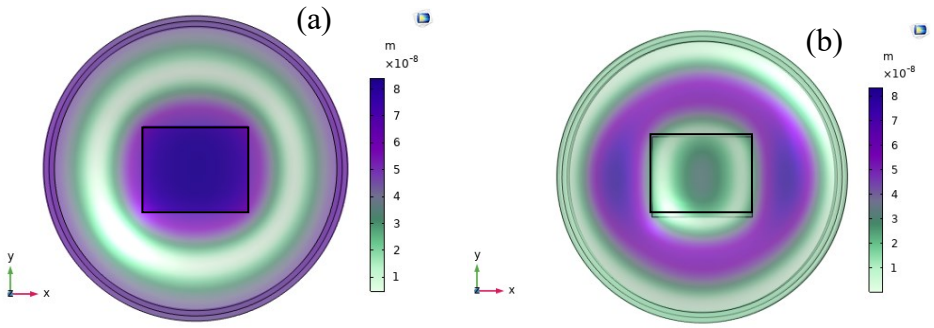


Figure 4.3. Dry condition eigenmodes: (a) 1203.3 Hz, (b) 6611.6 Hz.

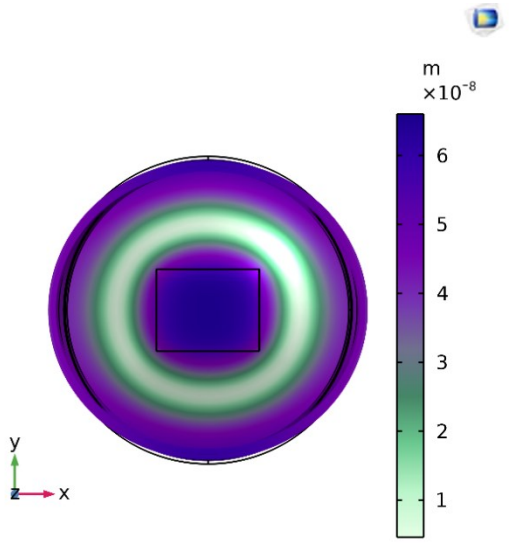


Figure 4.4. Water-filled fundamental eigenmode 978 Hz.

4.2.2. Electromechanical Simulation

Following the eigenfrequency analysis, the fully coupled electromechanical response was computed using the Piezoelectricity interface and the Frequency Domain Study Solver described in Section 2.2.2, with the same electrode boundary conditions (driving electrode and grounded counter-electrode) used for the Plexiglas plate. This analysis reproduces the actual harmonic voltage excitation applied experimentally, rather than a purely modal condition, and therefore provides a more realistic estimate of the operating resonance frequency.

In the dry condition, the electromechanically driven resonance was found at 1300 Hz, in reasonable agreement with, and slightly higher than the corresponding mechanical eigenfrequency of 1203.3 Hz; the small upward shift is attributable to the additional electromechanical stiffening introduced when the piezoelectric coupling and electrode loading are included explicitly, rather than being neglected as in the purely mechanical eigenfrequency solver. In the water-filled condition, the electromechanical resonance was found at 950 Hz, lower than the dry value, consistent with the fluid-loading trend already observed in the mechanical analysis.

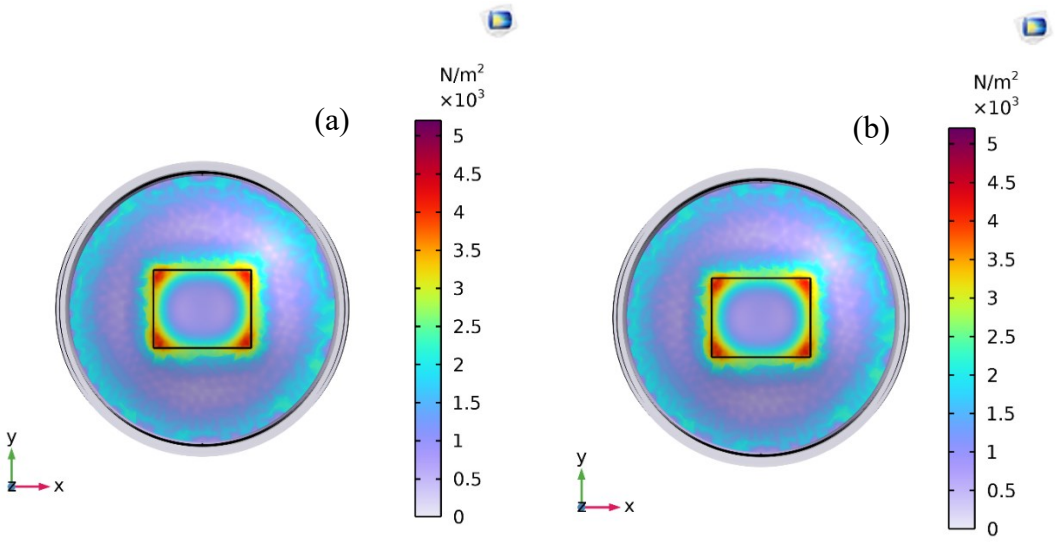


Figure 4.5. Electromechanically driven fundamental response: (a) dry, 1300 Hz; (b) water-filled, 950 Hz.

Figure 4.5 shows the corresponding electromechanically driven pressure fields. In both the dry (Figure 4.5a) and water-filled (Figure 4.5b) conditions, the field displays a sharply peaked, rectangular hot-spot of maximum pressure (red/yellow, reaching approximately 5×10^3 N/m²) directly coincident with the footprint of the bonded piezoelectric actuator, surrounded by a broader, roughly axisymmetric set of concentric pressure contours decaying toward the clamped rim. This rectangular near-field feature, absent from the purely mechanical eigenmode of Figure 4.3a, reflects the localized forcing imposed by the actuator geometry itself, which is captured only when the electromechanical coupling and electrode boundary conditions are modeled explicitly rather than solved as a modal eigenvalue problem. Away from the actuator, however, the two fields converge to the same overall single-antinode topology as the corresponding mechanical fundamental modes (Figs. 4.3a and 4.4), confirming that the electromechanically driven response and the mechanical eigenmode represent the same underlying fundamental mode of the dry and water-filled dish, respectively. To identify additional operating points beyond the fundamental mode, a broadband electromechanical frequency sweep was performed, tracking the maximum out-of-plane displacement amplitude as a function of driving frequency. As shown in Figure 4.6, the sweep of 50 Hz reveals a rich sequence of resonance peaks at approximately 950, 2600, 3650, 5300, 5900, 6650, 8000 and 8900 Hz. These higher-order resonances extend the set of frequencies available for exciting different modal patterns, and were subsequently used to select the driving conditions for the Chladni-pattern experiments reported in Section 4.3.3.

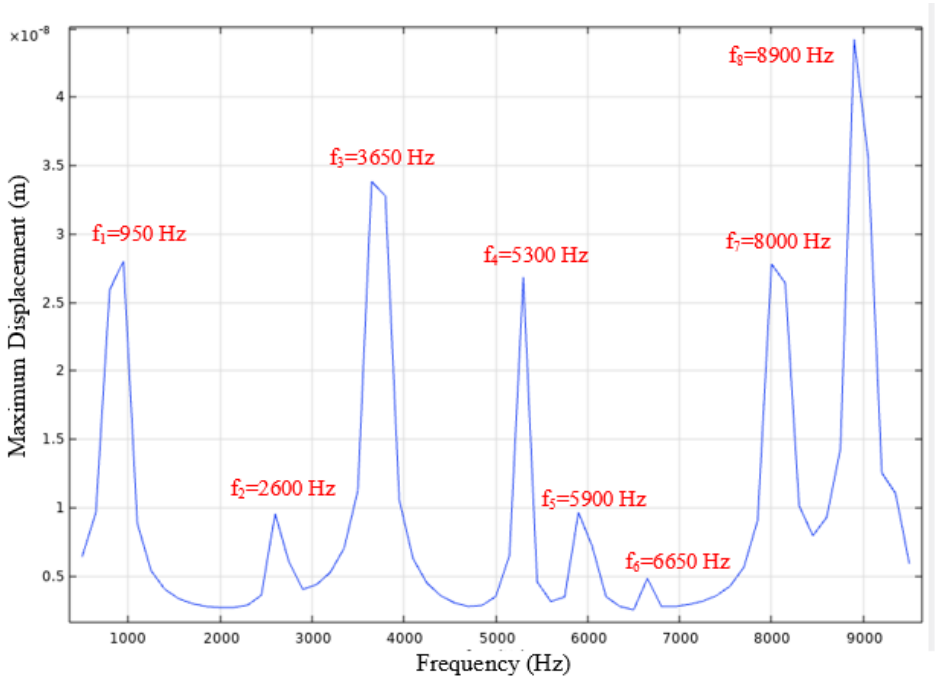


Figure 4.6. Simulated maximum out-of-plane displacement amplitude as a function of driving frequency (electromechanical model)

4.2.3. Extended Acoustic-Pressure and Particle-Tracing Simulation (Water-Filled Condition)

To support the interpretation of the water-filled Chladni-pattern and density-sorting experiments of Section 4.3.3, the electromechanical model, water-filled Petri dish was extended with a fully coupled acoustic-structure interaction and a particle-tracing physics interface and re-evaluated over a much wider frequency band from 500 Hz up to 15 kHz. This extended model tracks both the maximum structural out-of-plane displacement and the total acoustic pressure generated in the water, and adds particle-tracing simulations of iron particles (2 mm diameter, density 7800 kg/m³, denser than water) suspended in the fluid domain, allowing the resonances most relevant to particle trapping and sorting to be identified directly from simulation. Simulation results of the maximum out-of-plane displacement of the water-filled Petri are shown in Figure 4.7.

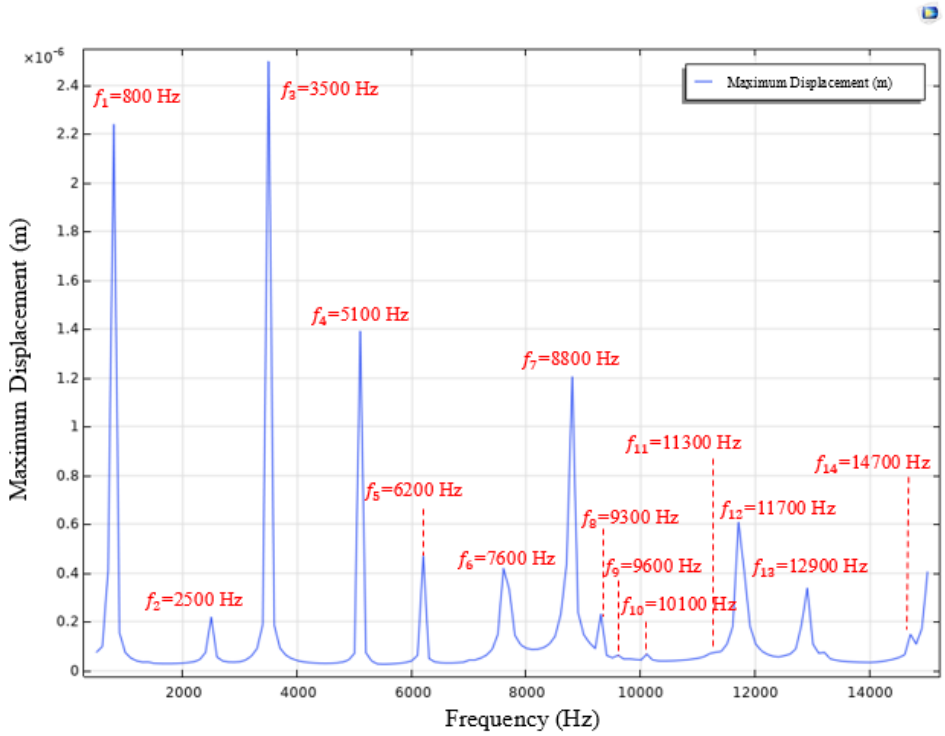


Figure 4.7. Simulated maximum out-of-plane displacement amplitude of the water-filled Petri dish over the 500 Hz–15 kHz band.

The corresponding total acoustic pressure generated inside the water, evaluated over the same frequency band, is shown in Figure 4.8. As expected for an acoustic-structure-coupled system, the acoustic pressure peaks occur at essentially the same driving frequencies as the structural displacement peaks, confirming that the fluid loading is being driven resonantly by the vibrating dish bottom.

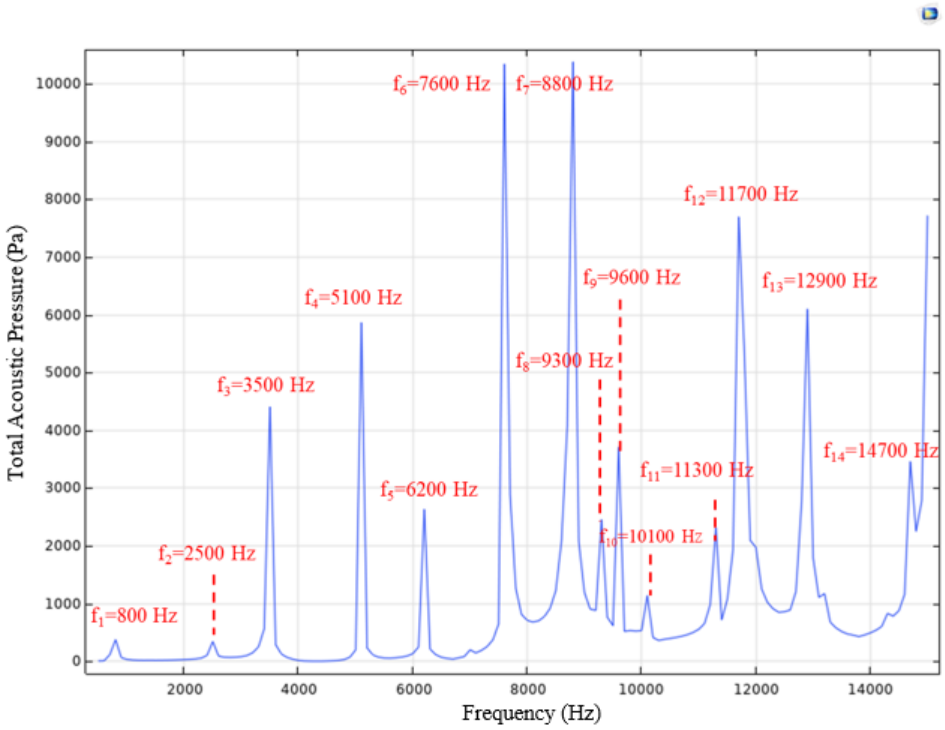


Figure 4.8. Simulated total acoustic pressure in the water Petri dish over the 500 Hz–15 kHz band.

Figure 4.9 show the simulated spatial distribution of the total unlike the narrower electromechanical sweep of Section 4.2.2, which identified eight resonance peaks based on structural displacement alone, this extended acoustic-structure model identifies fifteen resonance peaks across the wider 500 Hz–15 kHz band, reflecting the additional acoustic modes of the water cavity captured by the fully coupled simulation. Acoustic pressure at each of the fifteen resonance peaks. Each panel is a top view of the pressure field inside the water-filled cavity at the labeled driving frequency; warm colors (red) indicate positive pressure and cool colors (blue) indicate negative pressure relative to the ambient value, with the black rectangle marking the footprint of the piezoelectric actuator on the underside of the dish.

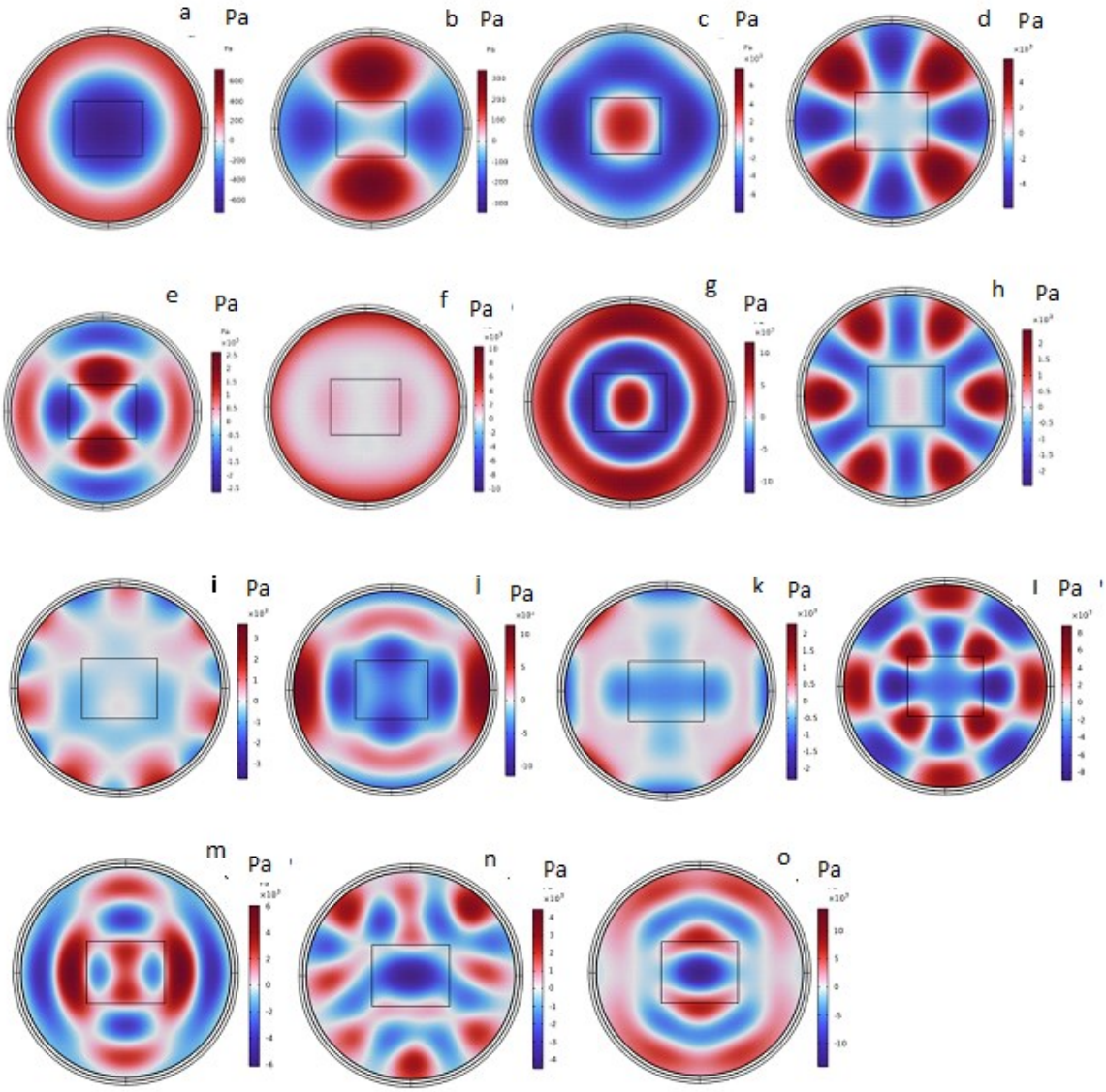


Figure 4.9 (a-o). Simulated total acoustic pressure field patterns in the water-filled at resonance peaks: a) f_1=800 Hz, b) f_2=2500 Hz, c) f_3=3500 Hz, d) f_4=5100 Hz, e) f_5=6200 Hz, f) f_6=7600 Hz, g) f_7=8800 Hz, h) f_8=9300 HZ, i) f_9=9600 Hz, j) f_{10}=10100 Hz, k) f_{11}=11300 Hz, l) f_{12}=11700 Hz, m) f_{13}=12900 Hz, n) f_{14}=14700 Hz, o) f_{15}=15000 Hz.

Figure 4.10 present the corresponding particle-tracing results: for each of the same resonance peaks, spherical iron particles of 2 mm diameter and 7800 kg/m³ density (denser than water)

were released in the fluid domain and allowed to evolve for 40 s under the combined effects of the acoustic radiation force and streaming drag, with the final particle positions colored by velocity magnitude. The particles consistently migrate toward the higher-pressure-amplitude regions of the corresponding pattern in Figure 4.9, directly reproducing, in simulation, the antinode-seeking behavior later observed experimentally for the iron particles in Section 4.3.3.

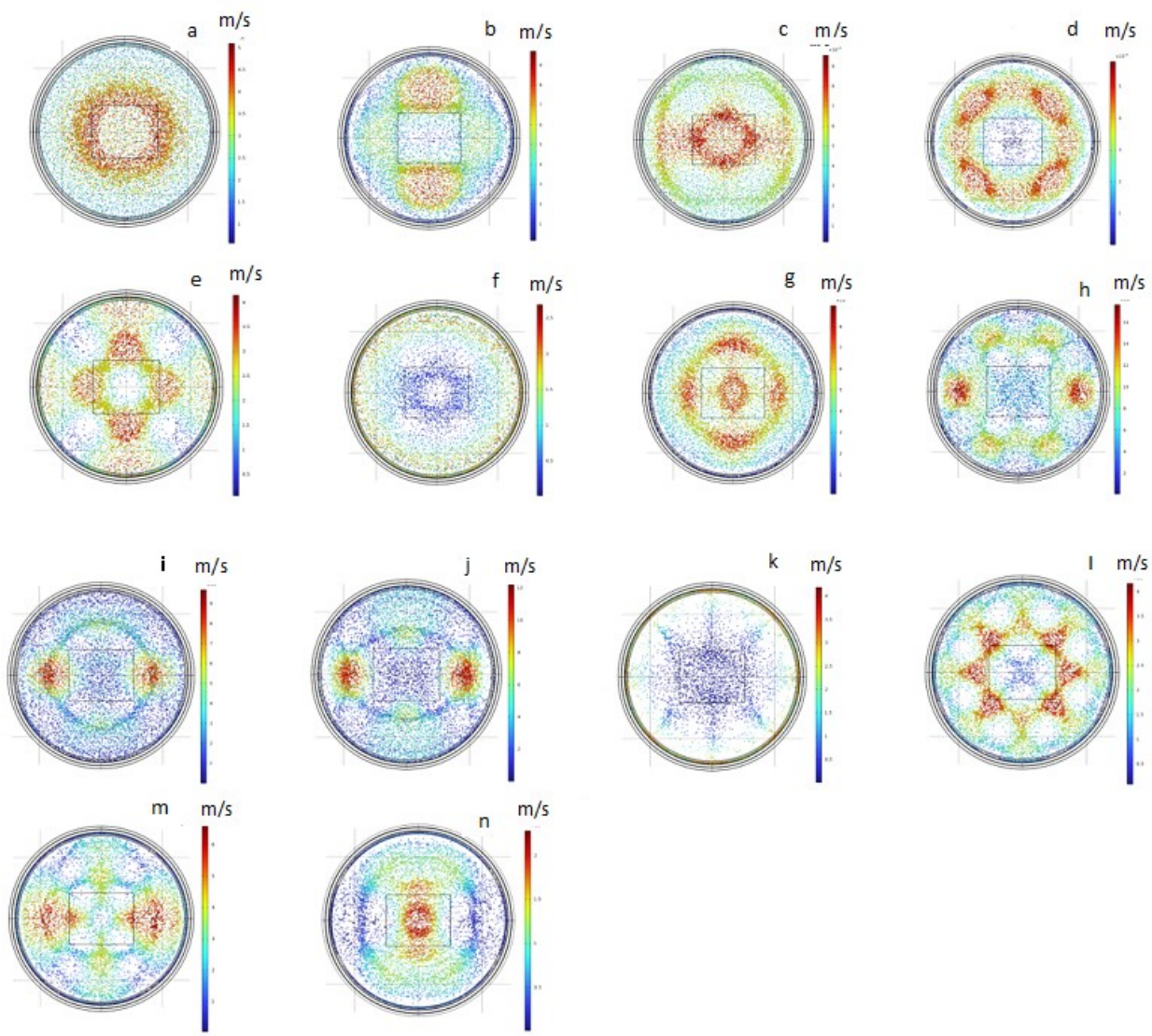


Figure 4.10. Simulated particle trajectories according their velocity (2 mm diameter, 7800 kg/m³ density) at t = 40 s for representative resonance peaks of a) f_1=800 Hz, b) f_2=2500 Hz, c) f_3=3500 Hz, d) f_4=5100 Hz, e) f_5=6200 Hz, f) f_6=7600 Hz, g) f_7=8800 Hz, h) f_8=9300 HZ, i) f_9=9600 Hz, j) f_{10}=10100 Hz, k) f_{11}=11300 Hz, l) f_{12}=11700 Hz, m) f_{13}=12900 Hz, n) f_{14}=14700 Hz.

The particle-tracing physics used in this extended model follows the theoretical framework recently established for the formation of inverse Chladni patterns on vibrating structures submerged in liquids in which the net force acting on a suspended microparticle combines the acoustic radiation force, the acoustic-streaming-induced drag force, and buoyancy/gravity, so that the particle motion is governed by [61] :

$$d(m_p v)/dt = F_d + F_{ac} + F_B + F_G \qquad (1)$$

where m_p is the particle mass and v its velocity. The acoustic radiation force F_{ac} is obtained from the Gorkov potential,

$$F_{ac} = \nabla\{V_0[3(\rho_p - \rho_f)/(2\rho_p + \rho_f)\cdot\langle E_{kin}\rangle - (1 - \beta_p/\beta_f)\cdot\langle E_{pot}\rangle]\} \qquad (2)$$

with ρ_p and ρ_f the particle and fluid densities, β_p and β_f the corresponding compressibilities, V_0 the particle volume, and $\langle E_{kin} \rangle$, $\langle E_{pot} \rangle$ the time-averaged acoustic kinetic and potential energy densities. For the iron particles used in this work, which are considerably denser than water ($\rho_p > \rho_f$), the kinetic-energy term dominates the force potential and carries a positive sign, so F_{ac} points toward the pressure antinodes rather than the nodes the mechanism responsible for the inverse Chladni behavior reproduced numerically in Figures 4.9 and 4.10 and observed experimentally in Section 4.3.3. The streaming-induced drag force is obtained from Stokes' law,

$$F_d = 6\pi\mu r_0(u_2 - v) \qquad (3)$$

Where r_0 is the particle radius, μ the fluid viscosity and u2 the acoustic-streaming velocity field. Because F_d scales linearly with particle radius while F_{ac} scales with particle volume ($\propto r_0^3$), the two forces are balanced by a threshold particle size, below which streaming drag dominates and particles instead follow the streaming vortices rather than settling at the antinodes. The 2 mm iron particles used in the present simulations and experiments lie well above this threshold, so acoustic radiation is expected to dominate their motion, consistent with the antinode-seeking trajectories of Figure 4.10.

4.3. Experimental Results

4.3.1. Spectral Response

The resonance frequencies of the Petri-dish platform were identified experimentally using the same self-mixing interferometric characterization procedure described in Section 2.1.1, complemented by direct visual identification of the Chladni patterns formed by the two indicator particle types used throughout this chapter: iron particles (denser than water) and purple plastic particles (less dense than water), placed on or in the vibrating structure. In the dry (empty) condition, two resonances were identified, at 1280 Hz and 6500 Hz. In the water-filled condition (~7 mm), a single dominant resonance was identified at 1090 Hz using both iron particles alone and a mixture of iron and purple plastic particles as indicators, together with a further higher-order resonance at 4500 Hz observed with the combined iron/purple-plastic mixture. Figure 4.11 shows the measured spectral responses used to identify these resonance frequencies, processed in MATLAB from the raw self-mixing interferometric acquisition. In this figure, the light-colored trace is the raw signal recorded directly by the acquisition system, and the darker, overlaid trace is the same signal after a moving-average smoothing filter has been applied in MATLAB to suppress high-frequency measurement noise while preserving the underlying resonance peaks; resonance frequencies are read off directly as the frequency at which the smoothed trace reaches a local maximum.

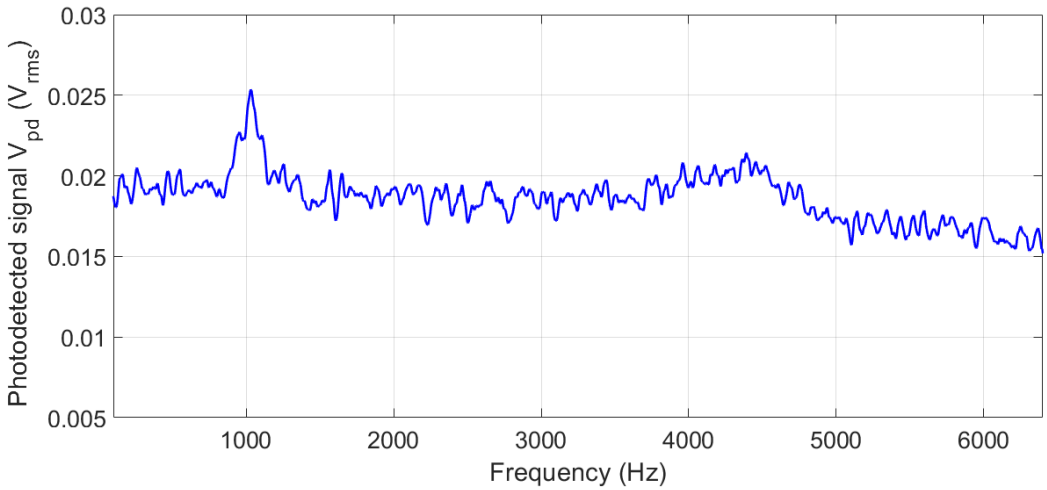


Figure 4.11. MATLAB-processed spectral characterization of the water-filled Petri dish (water level = 7 mm), measured at the center of the dish: photodetected self-mixing signal amplitude V_{pd} plotted against frequency from 0 to 6.4 kHz.

In Figure 4.11, V_{pd} is the amplitude of the voltage generated by the photodetector integrated in the laser package, which is directly modulated by the optical feedback induced by the vibrating dish surface; its amplitude therefore tracks the strength of the mechanical response at each driving frequency. The photodetected signal V_{pd} were acquired at the same measurement position (dish center) with the same driving amplitude (20 V peak-to-peak).

Table 4.2 compares these experimental values with the numerical predictions of Section 4.2 for the Petri dish configuration. The dry-condition results show good agreement between simulation and experiment, both for the fundamental (1203–1300 Hz predicted vs. 1280 Hz measured) and for the higher-order mode (6611.6 Hz predicted vs. 6500 Hz measured). In the water-filled condition, the measured fundamental (1090 Hz) is somewhat higher than both numerical estimates 978 Hz; this discrepancy is plausibly attributable to simplifications in the modeled water volume and boundary clamping conditions relative to the actual experimental setup, and should be revisited if a tighter quantitative match is required.

Table 4.2. Comparison between numerically predicted and experimentally identified resonance frequencies.

Condition	Numerical prediction	Experimental (Petri dish)
Dry/fundamental	1203.3 Hz	1280 Hz
Dry/higher order	6611.6 Hz	6500 Hz
Wet/fundamental	978 Hz	1090 Hz
Wet/higher order	3500 Hz	4500 Hz

4.3.2. Time-domain Response

Figure 4.12 reports the displacement-reconstruction results obtained specifically for the Petri-dish platform, driven at f = 1040 Hz (close to the 1090 Hz fundamental resonance identified in Section 4.3.1), with the self-mixing probe scanned along two orthogonal diameters of the dish, aligned with the long and short sides of the rectangular actuator at measurement points spaced 0.5 cm apart from −2.5 cm to +2.5 cm around the center.

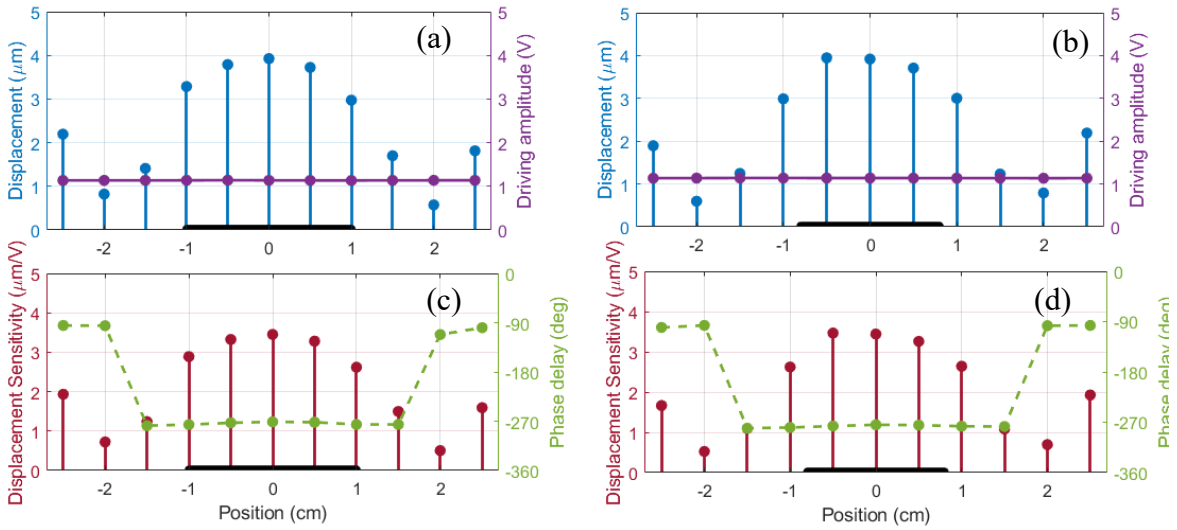


Figure 4.12. MATLAB-processed displacement results (blue stems) along the long side of the actuator axis (a) and along the short side axis (b) of the Petri dish at f = 1040 Hz, driving signal amplitude in purple. Displacement sensitivity (red stems) along the long side axis (c) and along the short side axis (d) and phase delay (green dashed line). The black horizontal bar marks the footprint of the piezoelectric actuator.

In Figure 4.12, the top panels (a, b) show the reconstructed out-of-plane displacement in micrometers at each scan position, obtained in MATLAB from the self-mixing interferometric signal by fringe counting and sub-fringe phase-shift extraction, as described in Section 2.1.2; the driving amplitude (purple, right axis) is shown on the same plot purely as a reference and is essentially constant across the scan, confirming that the spatial variation seen in the displacement is a genuine mode-shape effect and not an artifact of a varying drive level. The bottom panels (c, d) convert this displacement into displacement sensitivity (in µm per volt of driving amplitude), which is the more physically meaningful quantity for comparing different positions since it normalizes out the (nearly constant) drive level; the displacement sensitivity is highest near the center of the actuator and falls off toward the rim, consistent with the fundamental mode shape already predicted numerically in Section 4.2.1. The phase delay (green) is the phase lag, in degrees, between the driving voltage and the reconstructed displacement signal at each position. The phase delay remains essentially constant (≈ −270°) across the central region covered by the actuator, confirming that this region vibrates in phase as a single rigid-like antinode at this driving frequency. Toward the dish rim, the phase shifts sharply by approximately 180°, indicating that the outer region vibrates in antiphase with the center that is, moving in the opposite direction at each instant.

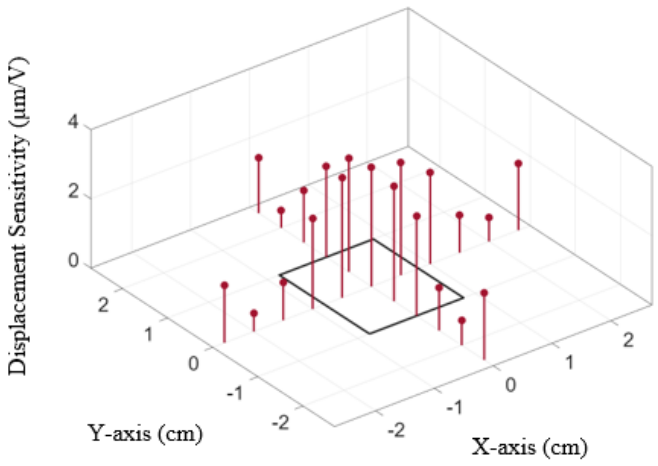


Figure 4.13. Full two-dimensional map of the displacement sensitivity (µm/V) of the Petri dish at f = 1040 Hz, reconstructed in MATLAB from a grid of self-mixing interferometric measurements over the dish surface; the black square marks the piezoelectric actuator footprint.

Figure 4.13 extends the single-axis scans of Figure 4.12 into a full spatial map The resulting displacement sensitivity map confirms, over the full two-dimensional surface, that the highest displacement-per-volt response is concentrated directly above and around the actuator, with a roughly axisymmetric decay toward the rim of the dish; this spatial map is what was subsequently used to select representative scan lines of Figure 4.12 and to choose favorable measurement positions for the spectral and Chladni-pattern studies of Sections 4.3.1 and 4.3.3.

4.3.3. Chladni Patterns

As discussed in Section 2.2.3, exciting the Petri dish at one of its resonance frequencies produces a spatially structured particle distribution that depends on whether the cavity is dry or filled with liquid. In the dry condition, particles migrate towards the vibrationless nodal lines of the structural mode shape, forming a classical Chladni pattern. In the water-filled condition, acoustic streaming reverses this behavior, driving particles towards the high-amplitude antinodes and producing an inverse Chladni Pattern. The Petri-dish platform was used to verify both regimes and to test whether the resulting patterns could be exploited for density-based particle sorting. The dry-condition mechanism is the classical mechanical effect in which particles are ejected from the high-amplitude antinodes by the direct motion of the plate and accumulate at the vibration-free nodes; it is therefore independent of particle density or size. The water-filled, inverse-pattern regime, by contrast, is governed by the acoustic radiation and streaming-induced drag forces of Eqs. (4.1), (4.3), introduced in Section 4.2.3, which depend explicitly on particle density and size and are responsible for the density-selective sorting demonstrated below.

In the dry condition, driving the empty dish at its fundamental resonance (1280 Hz) with iron particles produced a clear nodal Chladni pattern. The same pattern, at the same frequency, was reproduced independently with purple plastic particles, confirming that, in the dry regime, the resulting spatial distribution is governed by the structural mode shape itself and is essentially independent of the density of the indicator material (Figure 4.14a, 4.14b).

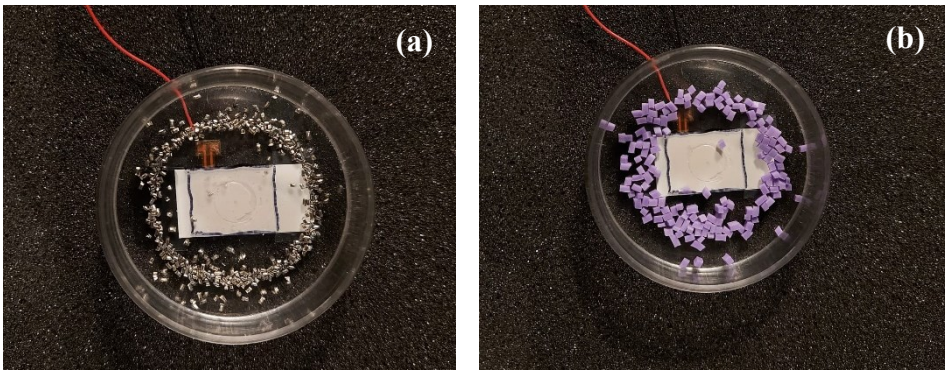


Figure 4.14. Dry-condition Chladni patterns at 1280 Hz obtained with the two indicator particle types: (a) iron particles; (b) purple plastic particles. Black lines on the white rectangle define the borders of the piezoceramic actuator. The white rectangle is the double side tape.

To assess whether this behavior persists once a fluid medium is introduced and whether acoustic streaming begins to dominate particle transport, as predicted numerically in Section 2.2.3 the same dish was filled with a ~7 mm layer of water and re-excited. Under this condition, the resonance shifted to 960 Hz. At this frequency, both iron particles alone and a mixture of iron and purple plastic particles produced an inverse Chladni pattern, with particles migrating toward the antinodal regions rather than the nodal lines observed in the dry case. This reversal confirms, for the Petri-dish geometry, that particle trapping under wet conditions is governed by the streaming-dominated mechanism already characterized numerically in Section 2.2.3, in contrast to the mode-shape-governed behavior observed in the dry condition. The density-selective sorting capability of the platform was then investigated directly with the dish filled with water, iron particles were combined with purple plastic particles (density lower than water) and the same driving condition was applied (with a small frequency scan performed around 960 Hz to optimize the pattern), the two particle populations segregated into distinct spatial regions according to their density (Figure 4.15), demonstrating that the acoustically driven Petri-dish platform can perform density-based particle separation, not merely single-species trapping. This density-selective behavior follows directly from the sign of the density-contrast term in the Gorkov radiation force of Eq. (2) in this chapter, introduced in Section 4.2.3. For the iron particles, denser than water, the coefficient (ρ_p-ρ_f) is positive and the kinetic-energy term dominates, driving the particles toward the acoustic pressure antinodes and reproducing the inverse Chladni Pattern already predicted numerically in Section 4.2.3. The purple plastic particles, by contrast, are hollow microspheres consisting of a thin polymer shell enclosing an air or gas-filled cavity; as a result, their effective density defined as total particle mass divided by total particle volume, shell plus enclosed cavity falls below that of water (ρ_p-ρ_f), even though the solid polymer itself is not intrinsically lighter than water. Because of this hollow structure, the density-contrast coefficient changes sign, reversing the dominant contribution to F_{ac} and shifting the equilibrium position of these particles away from the antinodes preferred by the iron particles. It is this density-dependent reversal of the acoustic radiation force, rather than any difference in particle size, since both particle types were of comparable size, that produces the spatial segregation observed in Figure 4.15.

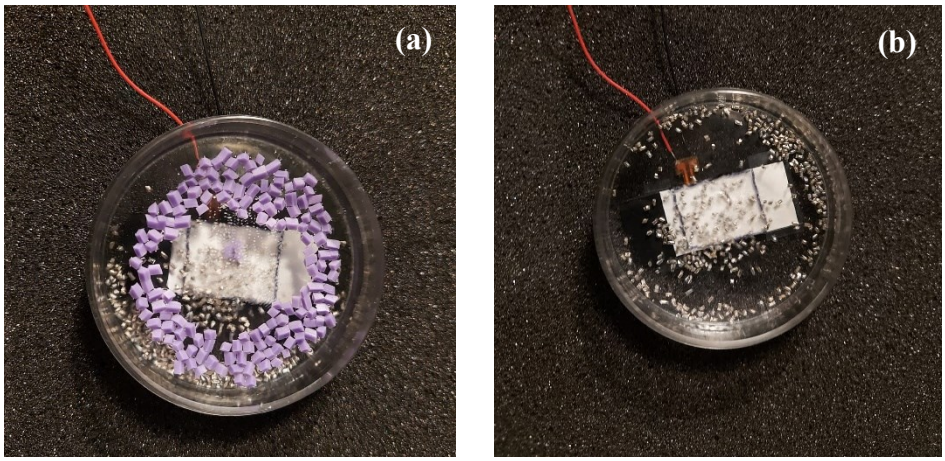


Figure 4.15. Water-filled Chladni patterns at 960 Hz: (a) plastic particles; (b) iron particles.

Taken together, the numerical and experimental results of this chapter show that the piezo-actuated Petri-dish platform reproduces, on a macroscopic and easily accessible geometry a density-independent nodal pattern in air, and a density-selective antinodal pattern once the cavity is filled with water. The good agreement between the predicted and measured dry-condition resonances, together with the demonstrated ability to spatially separate particles of different density at a single driving frequency, supports the use of this platform as a simple, low-cost testbed for acoustically driven particle sorting.

Chapter 5. Particle Manipulation in a Polymer Channel Microslide Using Piezoelectric Actuation

5.1. Materials and Methods

The Petri-dish platform of Chapter 4 demonstrated that a piezo-actuated, open, macroscopic cavity can display frequency-tunable, density-selective Chladni and inverse-Chladni patterns. However, an open dish is not directly compatible with the closed, sterile, and volume-controlled sample handling required in most biological and lab-on-a-chip workflows. We have thus applied the same characterization strategy finite-element eigenfrequency and electromechanical modeling, self-mixing interferometric spectral and time-domain characterization, and Chladni-pattern imaging on a more interesting platform that is a commercial, closed microfluidic channel, the Polymer Channel Microslide by Ibidi, actuated by a bonded piezoelectric element. Where the Petri dish served as a proof of concept for acoustic particle manipulation, the microchannel is intended as a step towards a practically deployable device, and Section 5.5 accordingly tests it directly on biological and bio-relevant samples (yeast) rather than only on inert indicator particles.

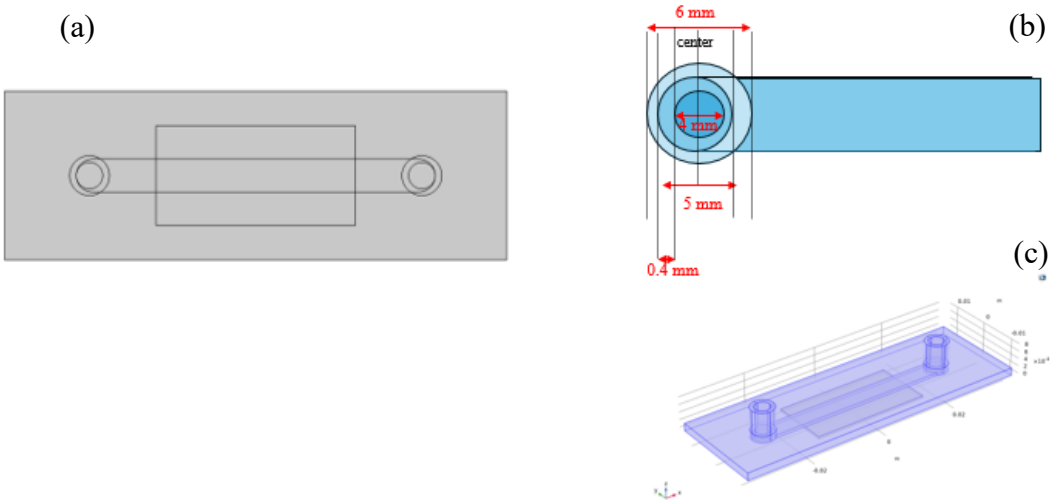


Figure 5.1. Structure of the microchannel (COMSOL CAD model). (a) Top view of the microchannel geometry, showing the two inlet/outlet ports; (b) detail view of the port region (c) three-dimensional isometric CAD rendering of the full microchannel structure.

The device is a microfluidic channel in the format of a microscopy slide, with two inlet/outlet ports as shown in Figure 5.1. Outer dimensions are 25.5 mm × 75.5 mm, whereas channel length, width, depth, and volume are 49 mm, 5 mm, 800 µm, and 200 µl, respectively. A piezoelectric actuator is bonded to the bottom face of the device, at its center, to provide the electromechanical excitation; the finer dimensions labeled in Figure 5.1b (6 mm, 5 mm, 4 mm, 0.4 mm) describe the inlet/outlet port region around this central actuator location. The COMSOL model couples four physics interfaces, consistent with the general modeling framework of Section 2.2. Solid Mechanics for the polystyrene microchannel structure, Pressure Acoustics (Frequency Domain) for the enclosed fluid (water or air), Electrostatics coupled through the Piezoelectricity Multiphysics node for the bonded actuator, and an Acoustic–Structure Boundary coupling linking the fluid and solid domains. The material tree

specifies four domains: Lead Zirconate Titanate for the piezoelectric actuator, a Tape layer representing the adhesive bond between the actuator and the microchannel body, Polystyrene (PS) for the microchannel structure itself, and H_2O (water) for the wet-condition fluid domain. The inclusion of an explicit Tape domain means that the model accounts for the finite stiffness of the bonding layer, rather than assuming an idealized rigid bond between actuator and structure. The frequency sweep was computed over the range 200–20000 Hz in 200 Hz steps. Material properties for each domain follow the general modeling methodology of Section 2.2, with the piezoelectric layer's Young's modulus set to 2.5 GPa for all Structure results reported in this chapter. Both air-filled and water-filled conditions were considered, following the same dual-condition strategy already used for the Petri-dish platform in Section 4.1. since the transition between the two is what drives the node-to-antinode reversal in particle trapping documented for the Petri dish in Section 4.3.3 and re-examined for the microchannel in Section 5.4.3. All self-mixing interferometric measurements and Chladni-pattern imaging follow the acquisition procedure described in Section 2.1.

5.2. Experimental Results

5.2.1. Spectral Response

The resonances of the structure were experimentally identified through a purely optical and contact-less technique, namely self-mixing interferometric frequency-domain measurements acquired at three positions along the channel, labeled A, B and C (Figure 5.2). At all three positions, the photodetected signal amplitude Vpd shows two spectral features: a dominant peak at around 660 Hz, corresponding to the first resonance, and a smaller secondary peak around 3.3 kHz, corresponding to a higher-order resonance. The consistency of the peak frequencies across the three positions indicates that they are global properties of the structure rather than local artifacts. The fundamental resonance at ≈660 Hz is therefore adopted as the operating frequency in the particle-trapping experiments presented in the next section.

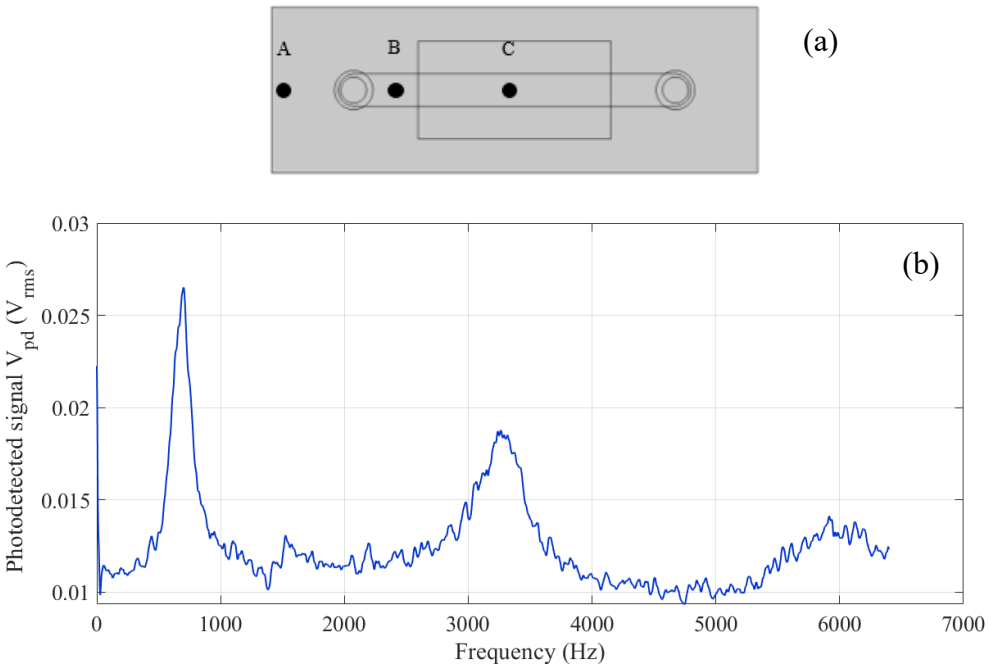


Figure 5.2. Continued on the next page

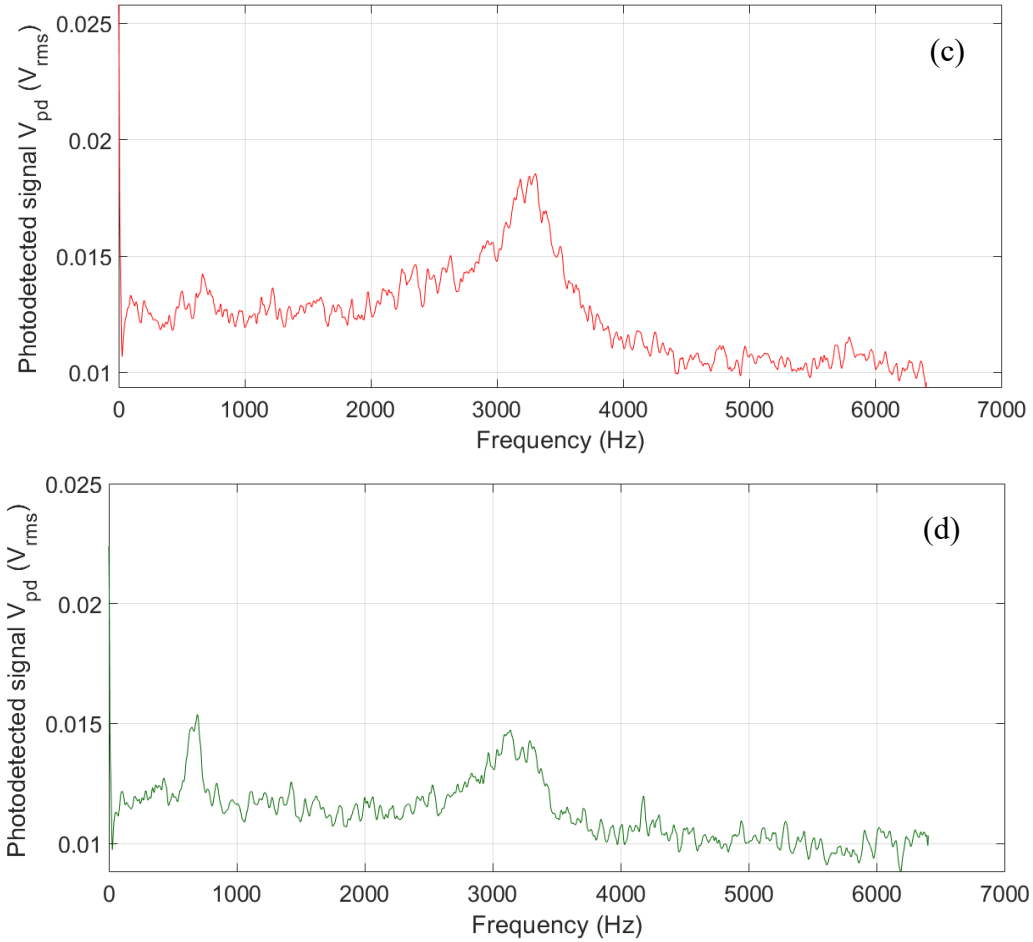


Figure 5.2. (a) schematic of the measurement positions along the channel, Self-mixing interferometric frequency-response measurements at three positions (b) Position A, near the inlet port; (c) Position B and (d) Position C.

5.3. Chladni Patterns

Chladni Pattern imaging (see Section 2.2.3 for the underlying physical mechanism) was used both to confirm the resonance frequencies identified spectrally and to evaluate the ability of the device to spatially redistribute particles. Quinoa seeds were used as a lightweight dry-condition indicator, driven at 20Vp-p. With no driving applied, the quinoa grains remain randomly and uniformly scattered on top of the microslide. Once the actuator is driven at a frequency close to 660 Hz, the grains collect into two straight lines running along the short sides of the channel, perpendicularly to its longer axis (Figure 5.3a). The fundamental mode's nodal lines run lengthwise at the edges of the 5 mm-wide. Driving at a frequency close to 6000 Hz produces a visibly different (Figure 5.3b), distributed more broadly across the channel width and consistent with the higher-order mode shape that will describe at section 5.4.1.

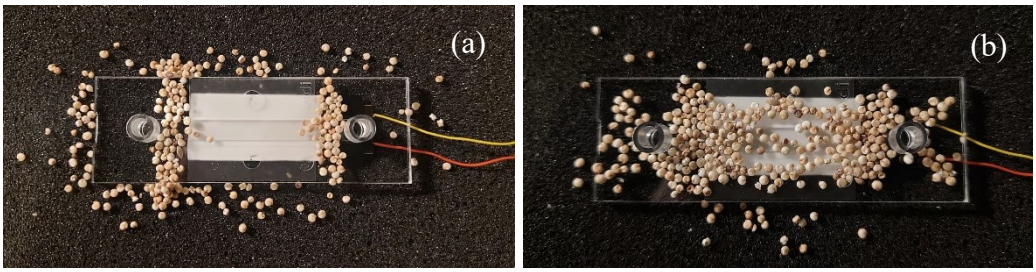


Figure 5.3. Air-filled-condition Chladni patterns with quinoa on top of the microslide; (a) Driving frequency ≈660 Hz, grains collect into two straight lines along the short sides of the microslide; (b) Driving frequency ≈6000 Hz.

The resonance frequencies of the air-filled channel were identified experimentally using quinoa grains as a Chladni Pattern indicator, following the imaging procedure of Section 2.1.1. Four resonances were identified: 660 Hz, 3300 Hz, and 6700 Hz under simple excitation, together with an additional resonance at 5900 Hz identified once the driving amplitude was increased to 20Vp-p, indicating that this particular mode requires a higher actuation energy to produce a visible indicator pattern than the other three, consistent with it being a weaker or less efficiently excited mode of the structure. Figure 5.4 shows the Chladni patterns formed by quinoa grains on the air-filled channel at two of the higher-order resonances: (a) at a driving frequency of approximately 6700 Hz and (b) at approximately 5900 Hz. In both cases, the grains move away from the regions of large vibration amplitude and accumulate in distinct clusters along the channel, marking the nodal regions of the vibrating surface. The two patterns differ clearly in how the grains are distributed, which shows that each resonance excites a different vibration mode of the channel.

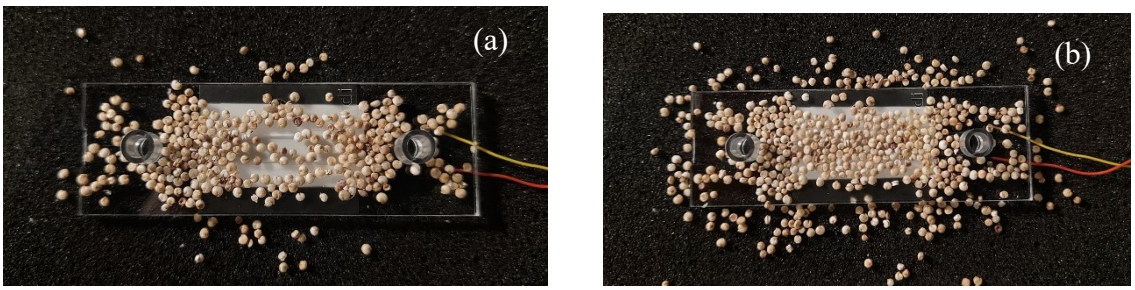


Figure 5.4. Air-filled-condition Chladni Patterns with quinoa:(a) driving frequency ≈6700 Hz, (b) driving frequency ≈5900 Hz

Iron particles injected into the channel by syringe, were then used to compare the water-filled (Figure 5.5) and air-filled (Figure 5.6) conditions at the fundamental resonance (≈660 Hz). Two water-filled trials, acquired on different dates, are reported. One with a larger particle load (many particles) Figure (5.5a) and one with a reduced load (few particles) Figure (5.5b), both driven at 20Vp-p. Comparing the two provides a basic check of whether the trapping pattern is sensitive to the amount of material being manipulated.

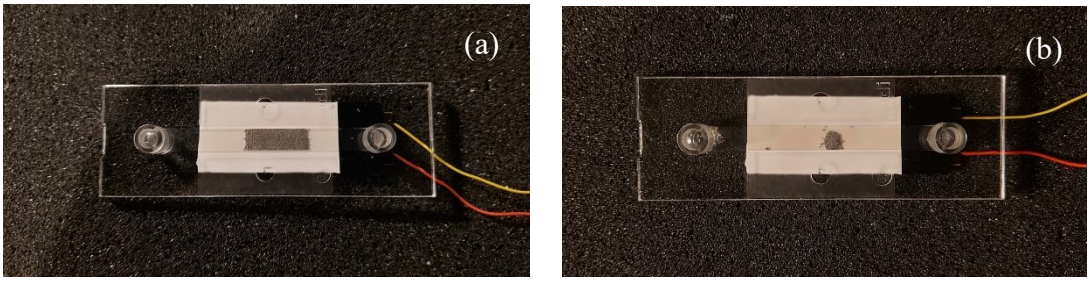


Figure 5.5. Water-filled microchannel with iron particles at ≈660 Hz: (a) higher particle load; (b) lower particle load.

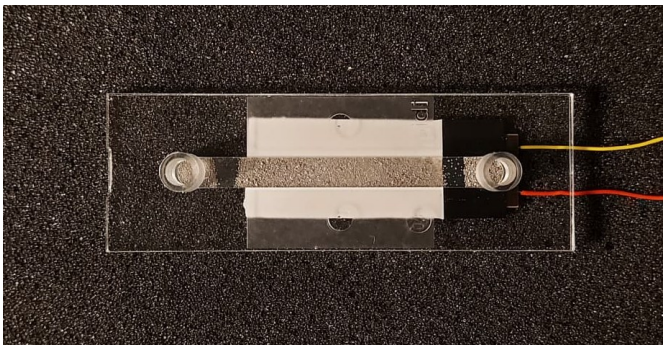


Figure 5.6. Air-filled Chladni Pattern with iron particles at ≈660 Hz.

Experimental observations at the fundamental resonance frequency (≈660 Hz) strongly corroborate this theoretical distinction between the wet and dry operational conditions. When the microchannel is filled with water, the presence of the fluid medium enables the acoustic radiation force to dominate, effectively concentrating the dense iron particles into a tight, highly localized band along the channel center (Figure 5.5). Conversely, under the air-filled condition at the same driving frequency, the absence of an effective fluidic coupling medium eliminates the fluid-mediated radiation force. Consequently, the iron particles fail to assemble into a central line and instead remain dispersed across the channel width or shift toward the structural vibration boundaries (Figure 5.6). This dramatic contrast confirms that the central alignment observed in water is governed purely by acoustic radiation forces within the fluid domain rather than direct mechanical surface vibrations.

5.4. Numerical Results

5.4.1. Mechanical and Electromechanical Modes in Air-filled Microchannel

Following the eigenfrequency and electromechanical modeling procedures described in Sections 2.2.1 and 2.2.2, four structural modes of the air-filled device were identified in the 0–7 kHz range, both as purely mechanical eigenfrequencies and as electromechanically driven resonances (Young's modulus of Polystyrene = 2.5 GPa) with the sweep of 50 Hz.

Figure 5.7 shows the four mode shapes in order of increasing frequency, confirming the expected bending-mode progression for a slender structure of this kind: the fundamental (624 Hz) is a single, gently curved bending shape along the microchannel's long axis. The second mode (2997 Hz) already shows a visible central dip, corresponding to one additional half-wavelength and the third and fourth modes (5150 Hz, 6265 Hz) display progressively more undulating multi-lobed shapes along the microchannel length with an increasing number of alternating up and down displacement lobes a similar qualitative pattern of increasing bending-mode order with frequency already observed for the Petri dish in Section 4.2.1.

Figure 5.8 (a-d) shows the corresponding electromechanically driven response, plotted here as the peak von Mises stress rather than displacement magnitude; at each frequency, the stress is concentrated around the two cylindrical port structures and along the device central actuated region, consistent with the actuator as described in Section 5.1.

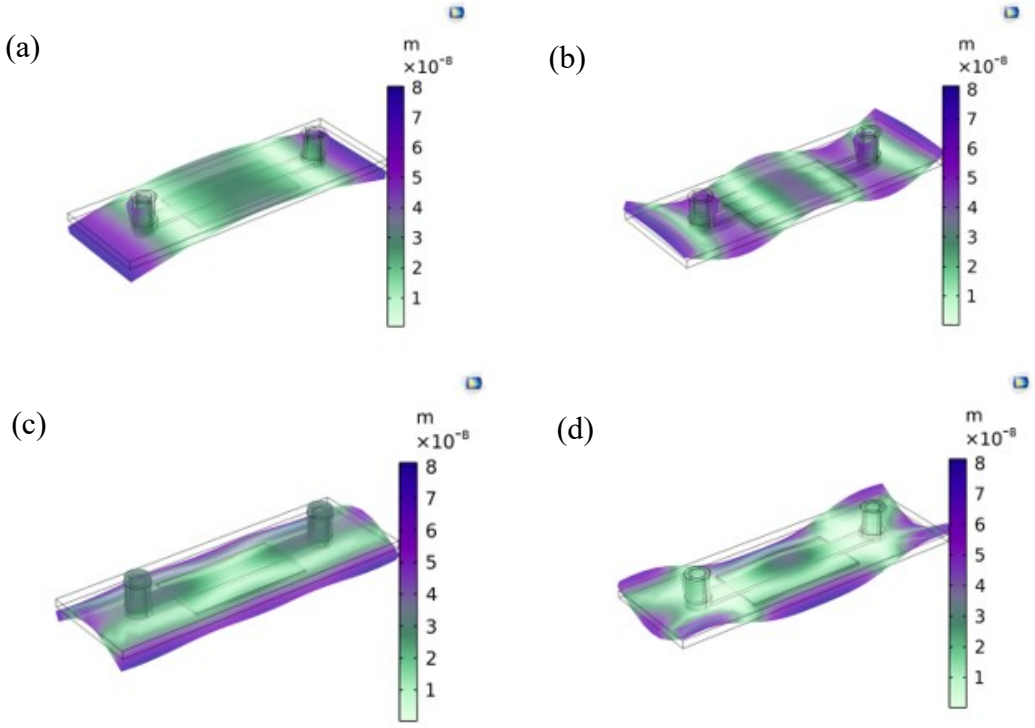


Figure 5.7. Mechanical eigenmodes of the air-filled mode Structure microchannel (a) 624 Hz; (b) 2997 Hz; (c) 5150 Hz; (d) 6265 Hz.

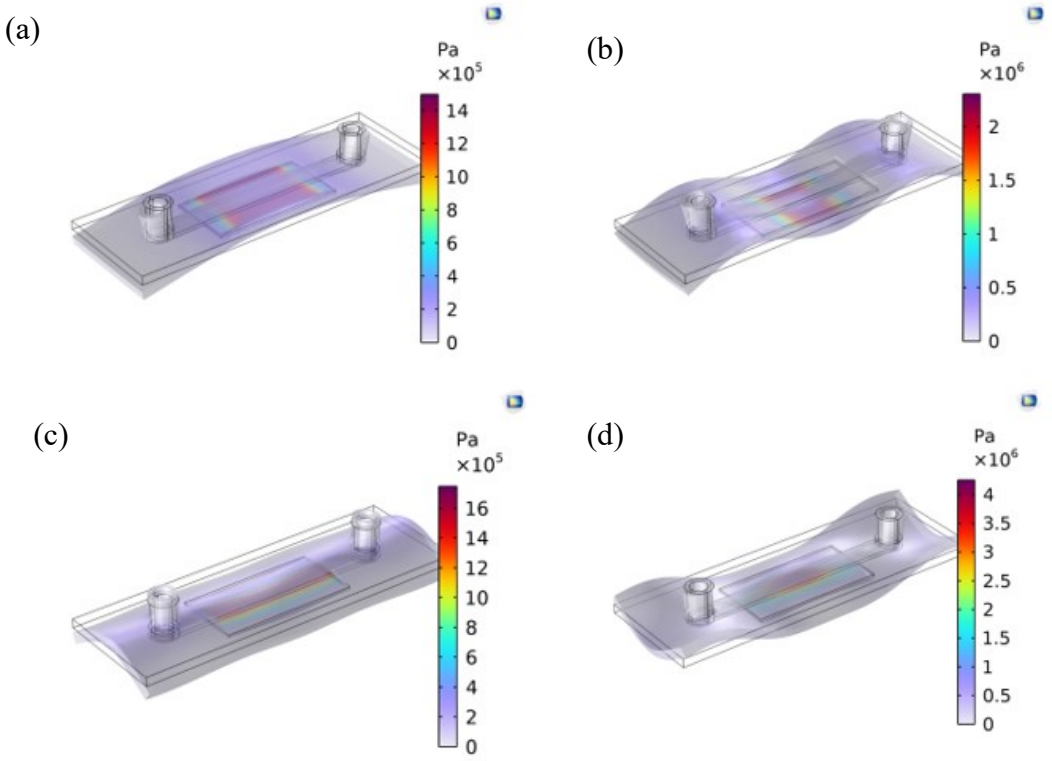


Figure 5.8. Electromechanically driven von Mises stress response of the air-filled Structure (E = 2.5 GPa): (a) 600 Hz; (b) 3000 Hz; (c) 5000 Hz; (d) 6200 Hz.

5.4.2. Water-Filled Response: Displacement and Acoustic Pressure Spectra

With the microchannel filled with water, a broadband electromechanical frequency sweep (200–20000 Hz) was performed to numerically obtain both the maximum structural displacement (Figure 5.9a) and the total acoustic pressure inside the fluid (Figure 5.9b). The two spectra do not coincide peak-to-peak. The displacement spectrum shows fourteen resonance peaks, and the acoustic-pressure spectrum shows fifteen. When the two figures (5.9a and 5.9b) are compared, only eleven peaks appear in both spectra simultaneously. These eleven common frequencies are the ones of practical interest for particle manipulation, since only at these frequencies the device simultaneously support a strong structural displacement and a strong standing acoustic-pressure field. The remaining frequencies appear as a resonance in only one of the two spectrum (600 and 3000 Hz in displacement only; 1600, 4600, 8600, 16800 and 17000 Hz in acoustic pressure only) and are less directly useful for acoustically driven trapping, even though they are still genuine structural or acoustic resonances of the system.

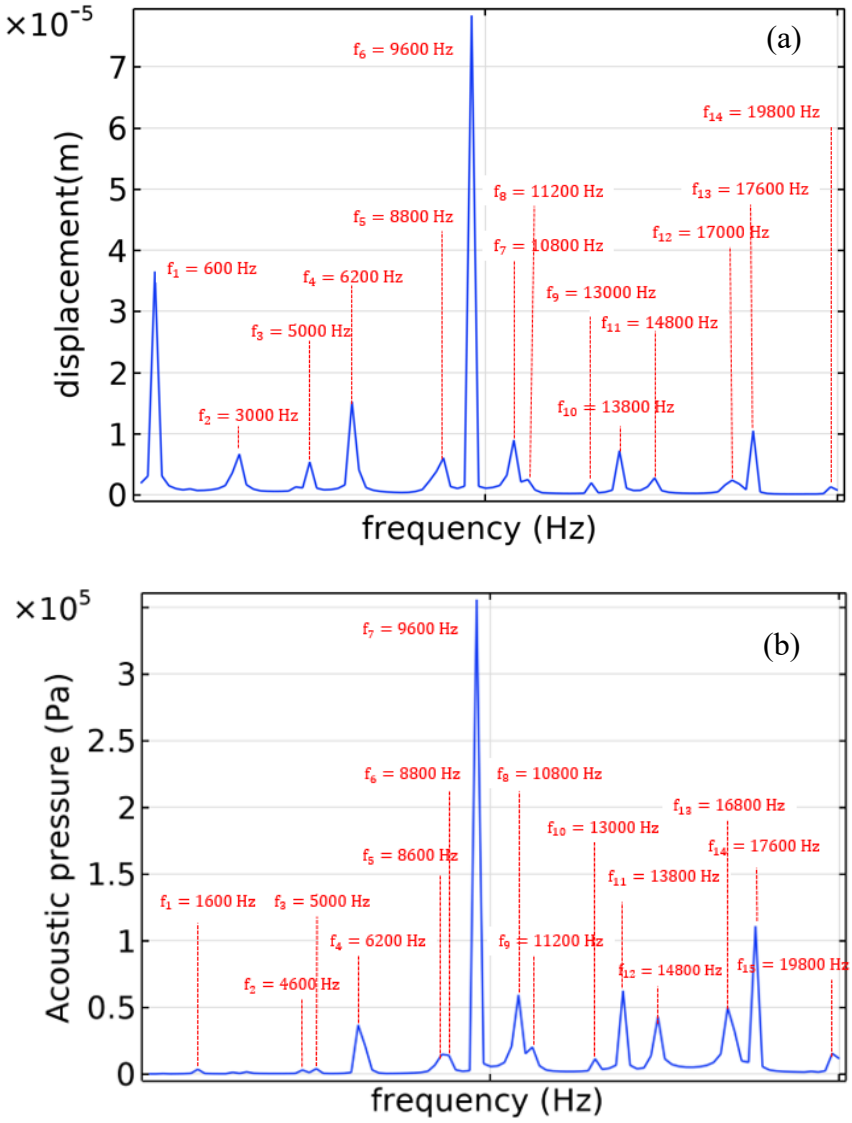


Figure 5.9. Water-filled microchannel, broadband electromechanical sweep: (a) maximum displacement spectrum (fourteen peaks, the highest at 9600 Hz); (b) total acoustic pressure spectrum (fifteen peaks, similarly the highest at 9600 Hz).

The higher-order mode shapes corresponding to several of these resonances (8900–18000 Hz) were additionally extracted and are shown in Figure 5.10. As frequency increases, the mode shapes display a progressively larger number of alternating displacement lobes along the microchannel length, consistent with the increasing bending-mode order already noted for the lower four modes in Section 5.4.1.

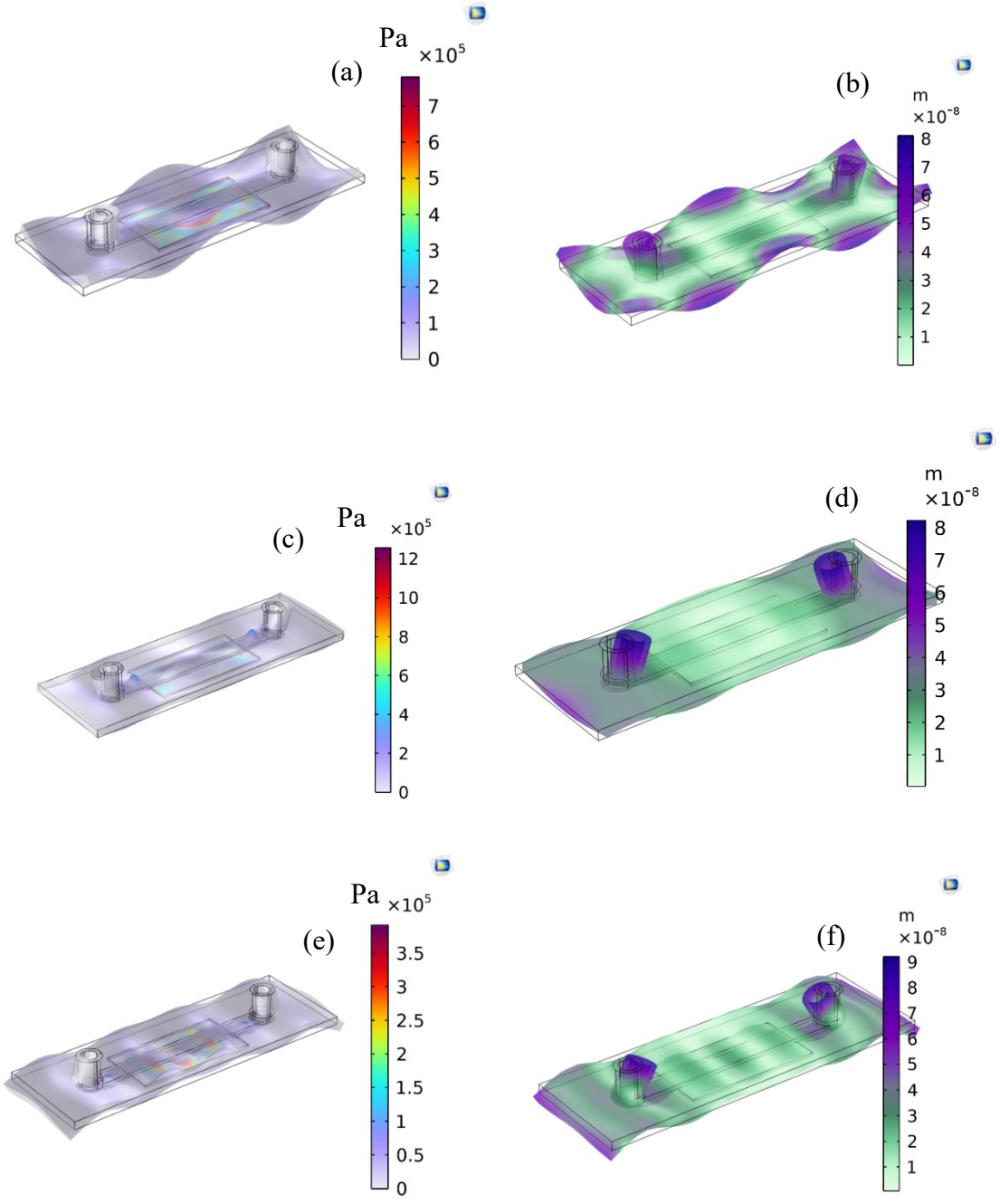


Figure 5.10. Continued on the next page

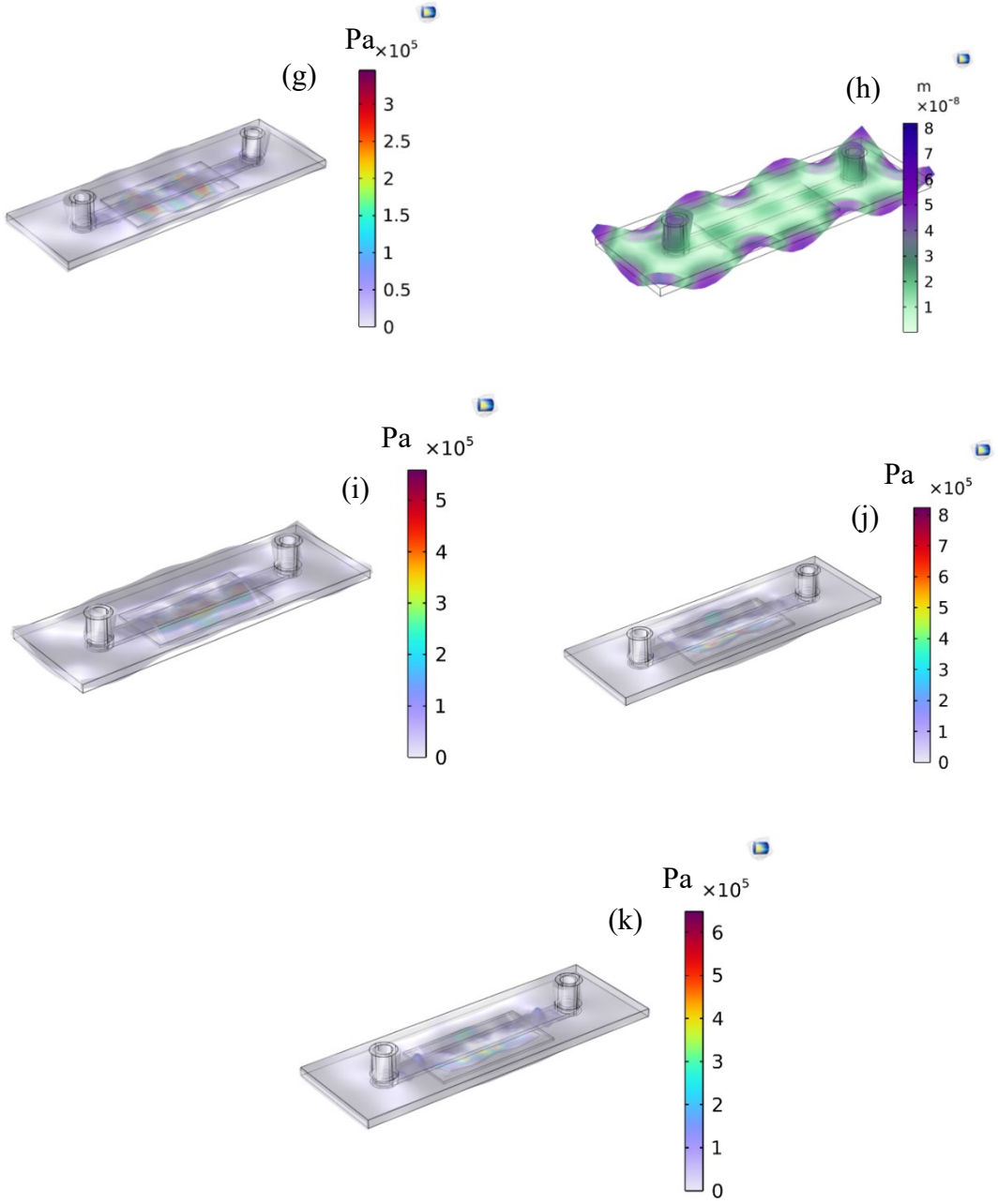


Figure 5.10. Higher-order mechanical/electromechanical mode shapes, air-filled mode (a) electromechanical at 9400 Hz, (b) mechanical at 9268 Hz, (c)electromechanical at 10000 Hz, (d) mechanical at 10037 Hz, (e) electromechanical at 11600 Hz, (f) mechanical at 11422 Hz, (g) electromechanical at 13400 Hz, (h) mechanical at 13410 Hz, (i) electromechanical at 16200 Hz, (j) electromechanical at 17600 Hz, (k) electromechanical at 18000 Hz.

The spatial distribution of the acoustic pressure field inside the water-filled microchannel was also examined individually at some of the resonance frequencies of Figure 5.9, via top-down surface plots of the total acoustic pressure (Figure 5.11). At the lowest frequencies (600–6200 Hz, Figure 5.11), the pressure field forms a single broad, high-pressure band running along the center of the microchannel between the two ports. As frequency increases through the common resonances (8600–13800 Hz), this central band progressively splits into an increasing number of alternating high and low-pressure lobes along the microchannel length and by the highest frequency tested 17600 Hz the pattern consists of many closely spaced alternating lobes spanning the full microchannel length. This directly confirms from the

COMSOL pressure-field solution itself. The acoustic standing-wave pattern and therefore the number and spacing of pressure nodes available for particle trapping becomes systematically finer as the driving frequency increases.

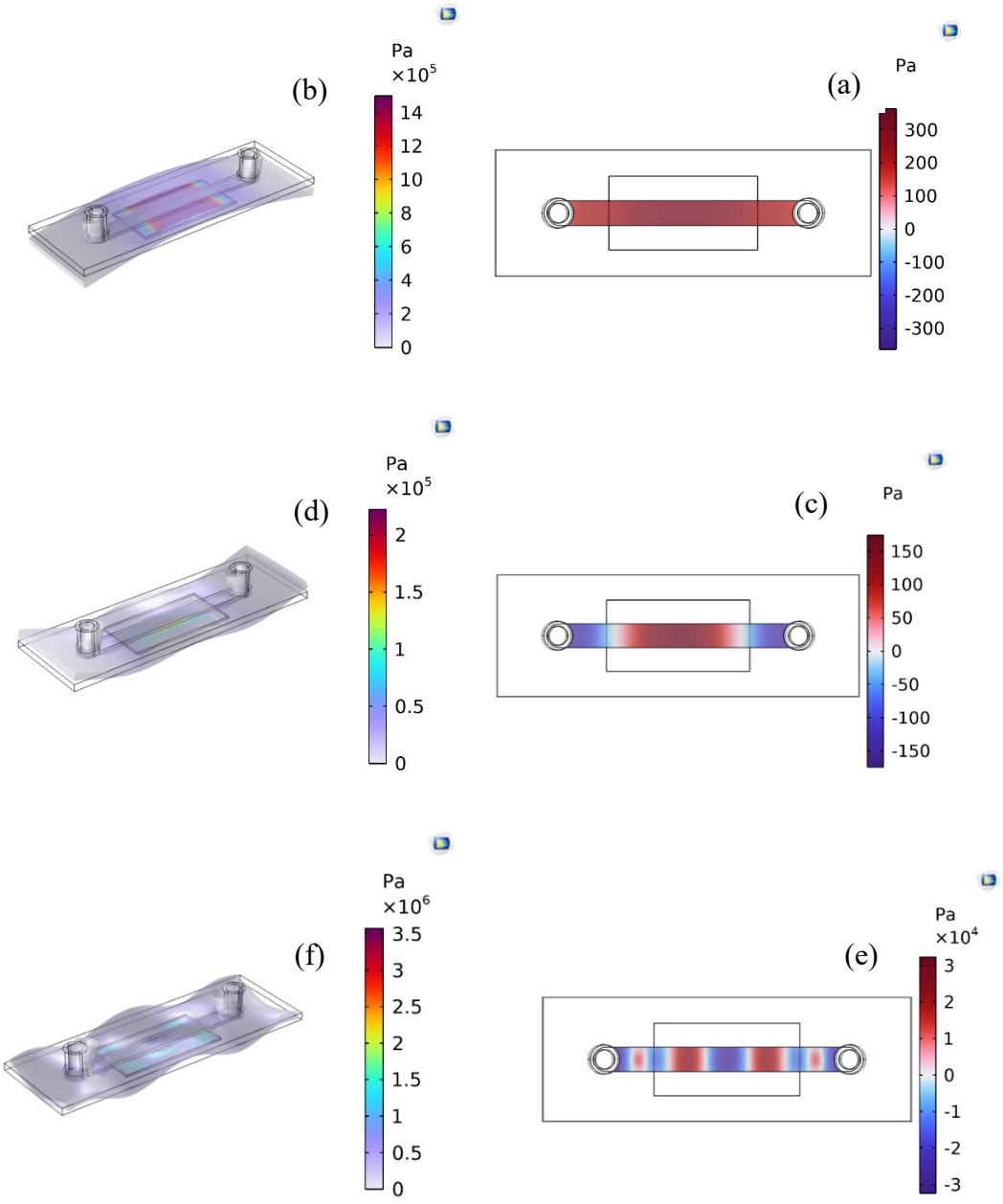


Figure 5.11. Continued on the next page

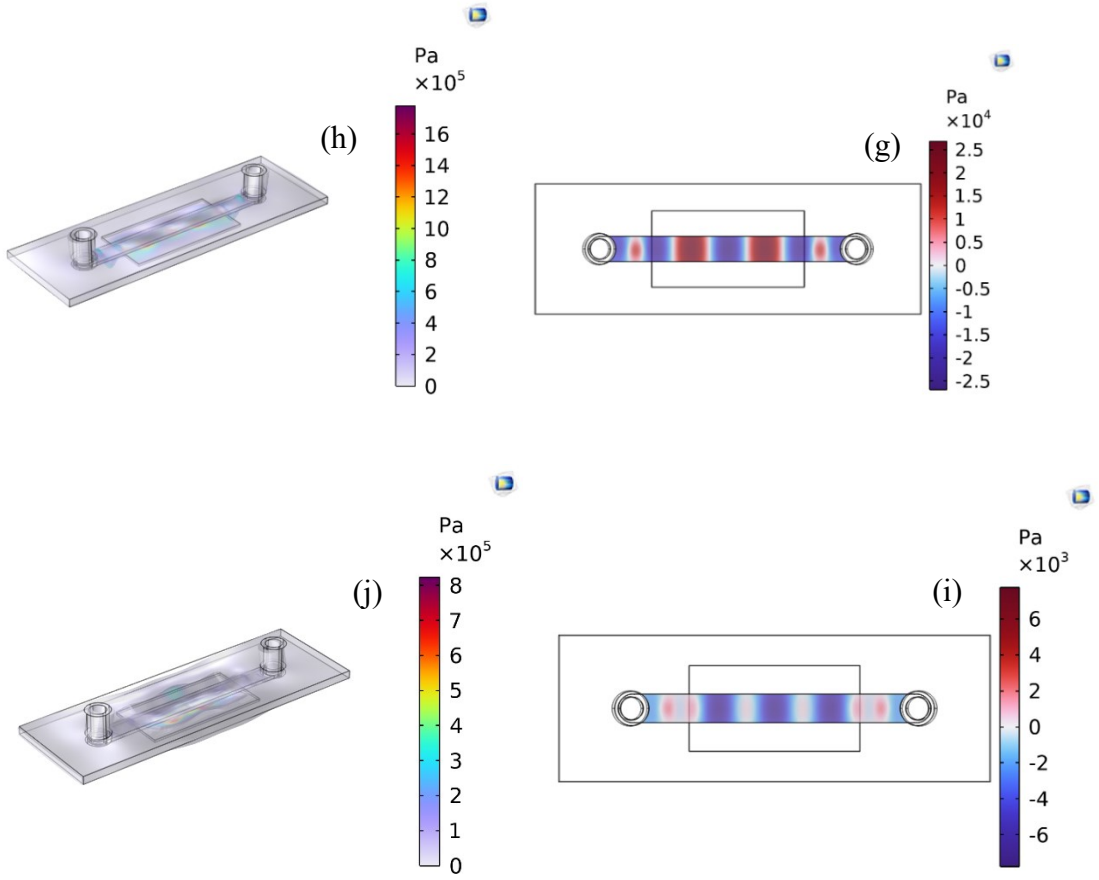


Figure 5.11. Acoustic pressure field at (a) 600 Hz (c) 1600 Hz (e) 9600 Hz (g) 10800 Hz (i) 17600 Hz; Von Mises stress at (b) 600 Hz (d) 1600 Hz (f) 9600 Hz (h) 10800 Hz (j) 17600 Hz.

5.4.3. Particle Tracing Simulation

Following the particle tracing methodology mentioned in Section 2.2.3, iron microparticles were introduced (numerically, and later experimentally by syringe injection) into the water-filled and air-filled microchannel, and their behavior was simulated at the first two resonances at which both the structural displacement and the acoustic pressure are strong, that is f_1=600 Hz and f_2=9600 Hz, selected from Figure 5.9 using the Particle Tracing for Fluid Flow physics in COMSOL. In the water-filled microchannel, particle motion is governed by the same acoustic radiation force and viscous Stokes drag balance introduced in Section 1.3.1 (Equations 7–12). For iron particles, the density ($\rho_p \approx$ 7870 kg/m³, roughly eight times that of water) and stiffness are both much greater than those of water, so f_1 and f_2 (Equations (8), (9)) are positive and close to their upper limits, giving a strongly positive contrast factor Φ (Equations (11)). As established in Section 1.3.1, a positive Φ drives particles toward the pressure nodes of the standing wave equivalently, the displacement antinodes. This is the same node-concentration behavior responsible for antinode trapping observed in the Petri-dish platform in Section 4.3.3, and it is expected to reproduce itself here. The iron particles should collect at the displacement antinodes of the water-filled microchannel. This frequency dependence is directly confirmed by the acoustic pressure field maps of Figure 5.11(e) at 9600 Hz the standing-wave pattern already shows more closely spaced pressure lobes along the microchannel than at the lower frequencies of Figure 5.11(c), so the particle-tracing pattern at

9600 Hz is expected to subdivide into a correspondingly larger number of narrower particle-collection regions than at 600 Hz. To investigate the time-dependent acoustic trapping dynamics, the numerical particle distribution in the water-filled microchannel driven at 600 Hz was evaluated at different time steps, as depicted in Figure 5.12. At t = 5 s (Figure 5.12a), the suspended iron particles begin migrating toward the channel center under the influence of the localized acoustic pressure gradient, displaying an initial transverse gathering behavior. As actuation progresses to t = 10 s (Figure 5.12b), the dominant primary acoustic radiation force, coupled with fluidic interactions, forces the particles to assemble into a significantly tighter, well-defined central focus band along the channel axis. This temporal evolution clearly demonstrates the progressive nature of the acoustic trapping mechanism, confirming that steady-state spatial alignment is achieved within a few seconds of continuous excitation.

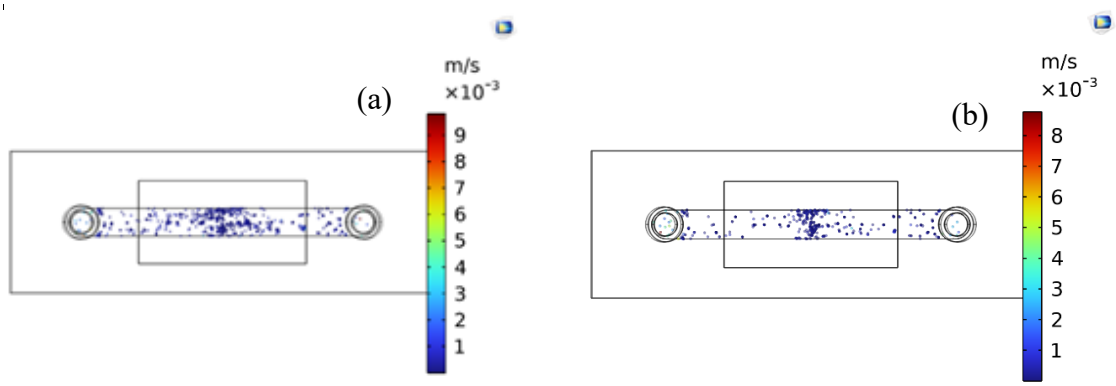


Figure 5.12. Top view of the simulated iron-particle distribution in the water-filled microchannel at 600 Hz at (a) t =5s and (b) t=10s after starting the actuation.

Furthermore, at a higher operating frequency of 9600 Hz (Figure 5.13), the increased acoustic wavelength spatial density modifies the pressure landscape, causing the particles at t = 5 s to organize into multiple localized nodal clusters distributed periodically along the length of the channel. This distinct transition from a single continuous axial band to discrete multi-cluster trapping highlights the strong frequency dependence of the acoustic radiation potential in tailoring particle patterning regimes

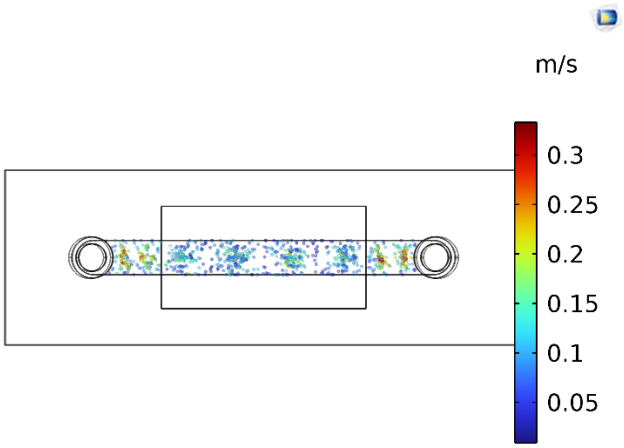


Figure 5.13. Top view of the simulated iron-particle distribution in the water-filled microchannel at 9600 Hz at t = 5s after actuation.

In the air-filled microchannel, by contrast, air is a much more compressible and lower-density medium than water, so the magnitude of the acoustic radiation force acting on the iron particles is expected to be substantially weaker. However, because the microchannel remains a sealed, enclosed acoustic cavity in this configuration, air is still in principle, capable of sustaining a standing acoustic pressure field, and the same Gor'kov type radiation force mechanism described above for water may still apply only more weakly and over a correspondingly longer timescale. This is expected to differ qualitatively from the classical open-surface Chladni mechanism of Section 2.2.3, in which particles resting on an exposed, atmosphere-facing solid surface respond directly to the mechanical vibration of that surface and migrate towards the nodal lines of the structural mode shape. Whether the enclosed air-filled channel behaves acoustically like a weak fluid trapping particles at antinodes, as in water or instead like an open Chladni surface trapping particles at nodes is therefore not obvious a priori, and is examined numerically below.

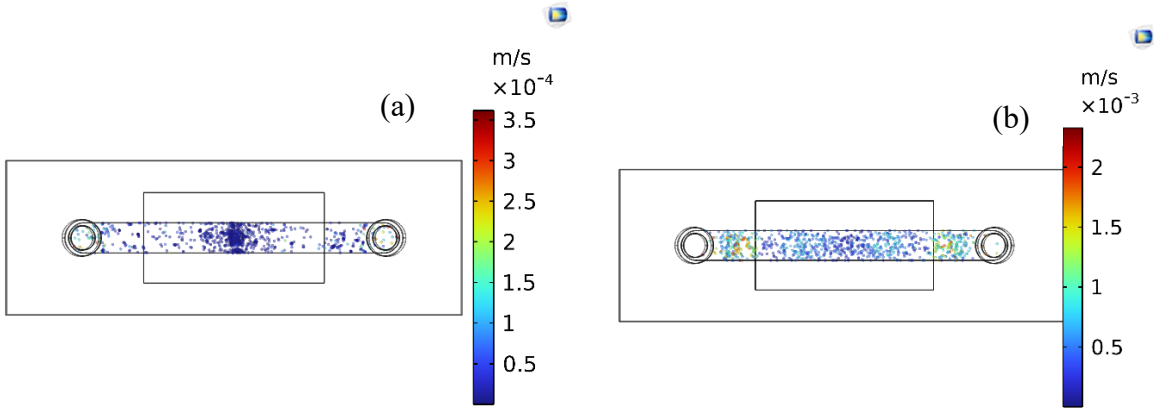


Figure 5.14. Top view of simulated iron-particle distribution in the air-filled microchannel: (a) 600 Hz; (b) 9600 Hz.

The air-filled simulation results (Figure 5.14), are more nuanced than a simple dry/wet reversal. At 600 Hz, after a long driving time (t = 120 s), the iron particles in air do collect into a dense central band the same location as in water (Figure 5.12), not the edge/node location that would be expected from a classical open-surface Chladni mechanism. This supports the interpretation above. Within this enclosed-cavity COMSOL model, air still behaves acoustically as a weak radiation force transmitting fluid, so the governing physics, and therefore the trapping location, is qualitatively the same in air as in water, differing mainly in the much longer time (120 s vs. a few seconds) needed to reach a comparable degree of clustering, consistent with the much weaker radiation force expected in air. At 9600 Hz, only an early transient (t = 5 s) is available, and the particles have not yet clustered. They remain spread along the channel with the highest instantaneous velocities near the two ports, which may indicate either that clustering at this higher frequency requires an even longer settling time, or that the higher-order acoustic field in air produces a qualitatively different, multi-lobed transient pattern before finally settling.

In the dry condition, the simulation results and the experimental results show different particle behaviors. The quinoa grains are placed outside the channel on its open surface, whereas the iron particles are placed only inside the channel. In the simulation, the particles are suspended inside the microchannel and they accumulate at the center of the channel. In the experiment, the particles rest directly on solid surfaces exposed to the atmosphere. The quinoa particles collect away from the center, along the two edges according to the Figure. 5.3a. The iron particles inside the microchannel accumulate at the center part as shown in Figure. 5.14a. This difference is plausibly explained by the fact that the two air conditions are not physically the

same experiment. In the experimental tests, the particles are in direct contact with a vibrating open surface, so the relevant mechanism is the behavior of Chladni patterns. In the simulation, the particles are fully enclosed within the microchannel and are governed by the acoustic radiation force inside the cavity. The two dry configurations are therefore complementary rather than contradictory. Whether an air-filled microchannel behaves like an open Chladni plate or like an acoustofluidic cavity depends on whether the particles sit on an exposed solid surface or are fully enclosed. This distinction should be kept in mind when designing any future closed-channel biological application (Section 5.5).

Table 5.1 compares the resonant frequencies identified experimentally via interferometric measurements under dry conditions with the numerical predictions. The results show good qualitative agreement. All four experimental values fall within or close to the predicted numerical range. However, across all four resonances, the experimental frequencies are systematically higher than both the mechanical and electromechanical numerical predictions by approximately 6–15%. Differences might be attributed to a modeling simplifications of the boundary clamping conditions (assumed ideal in COMSOL, but in practice softened by the mounting hardware and adhesive layers) and the assumed material properties.

Table 5.1. Comparison between numerically predicted and experimentally identified resonance frequencies.

Condition	Numerical (air-filled)	Experimental (air-filled)
Fundamental	600–624 Hz	660 Hz
2nd resonance	2997–3000 Hz	3300 Hz
3rd resonance	5000–5150 Hz	5900 Hz
4th resonance	6200–6265 Hz	6700 Hz

5.5. Biological Application

Sections 5.3 and 5.4 established, for the water-filled channel, a set of driving frequencies at which a strong structural and acoustic-pressure resonance coexist., and confirmed experimentally that at least the fundamental of theseresonance (≈660 Hz) is expected to produce a reproducible particle-trapping pattern with an inert, dense indicator (iron, Section 5.4.3). The purpose of this section is to test whether the same driving conditions can be applied, without modification, to particles of direct biological interest a necessary step before the platform can be considered for any real sample-handling or cell-sorting application. Two particle types were tested: Yeast suspension in phosphate-buffered saline (PBS), as a biological test case, and polystyrene microspheres of well-defined diameter, as a rigid, monodisperse reference.

5.5.1. Yeast in PBS

Yeast suspensions (Saccharomyces boulardii) at two nominal concentrations (1× and 10×, where 10× is ten times concentrated than 1×) were tested at frequency of 660 Hz. For the 660 Hz condition, the 10× and 1× suspensions were imaged after 1.5 hours of continuous driving. No reproducible accumulation of yeast cells at a specific location in the microchannel was observed for yeast concentration 1× and 10× (Figure 5.15a) and (Figure 5.15b), respectively. These negative results, obtained under otherwise identical driving conditions to the successful iron-particle trapping of Section 5.3, represent itself an important finding of this chapter, and

is analyzed below.

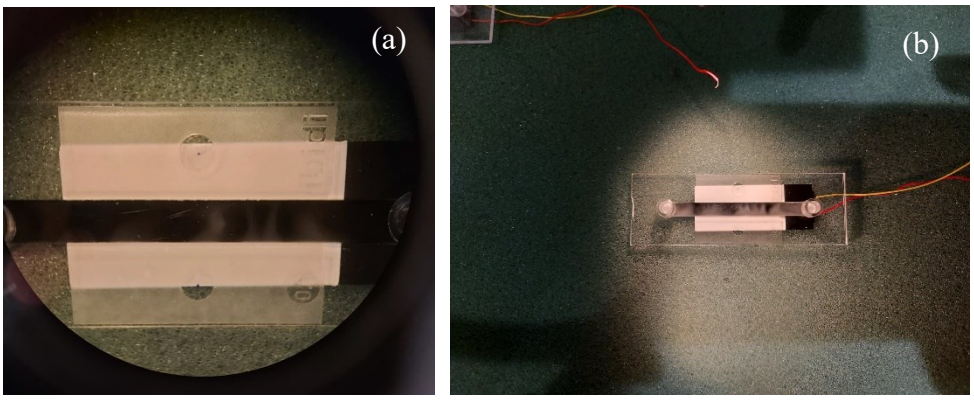


Figure 5.15. Yeast in PBS at frequency 660 Hz: (a) concentration 1×; (b) concentration 10×

Two independent physical factors are believed to contribute to this absence of trapping, and most likely act together. First, a piezoelectric actuator is, electrically, predominantly a capacitor, with an impedance $Zc=1/2\pi fC$ that decreases as the driving frequency increases. If the signal generator or amplifier used to drive the actuator has any non-negligible output impedance R_s, the actuator and source together form a simple voltage divider, and the voltage actually delivered across the piezoelectric element is

$$V_{piezo}(f) = V_{source} \times \frac{Z_C}{R_s + Z_C} = \frac{V_{source}}{\sqrt{1+(2\pi f R_s C)^2}} \qquad (1)$$

which falls below the nominal source voltage once the frequency is high enough that $2\pi fCRs$ becomes comparable to or greater than 1 and continues to decrease as f increases further. This is consistent with the reduction in effective driving voltage observed experimentally when the driving frequency was increased: even though the nominal source amplitude was set to, e.g., $20V_{p\text{-}p}$, the voltage actually reaching the piezoelectric element, and hence the mechanical displacement and acoustic pressure it can generate, was in practice significantly lower, particularly at the higher frequencies tested (e.g., 10,000 Hz).

This voltage roll-off, however, does not by itself explain the absence of trapping at the fundamental resonance (≈660–700 Hz), where the iron particles of Section 5.3 were trapped successfully under nominally the same driving conditions. The second, and most likely dominant, factor is the very strong particle-size dependence of the acoustic radiation force (FARF $\propto a^3$; Eq. 10, Section 1.3.1). Since a particle's radius enters the force cubed, even modest size differences translate into large force differences. Yeast cells are roughly 3–10 µm in diameter (a ≈ 1.5–5 µm), one to two orders of magnitude smaller than the iron filings used in Section 5.3 (typically of order 100 µm or larger). A conservative order-of-magnitude estimate, taking a 10:1 radius ratio, gives a radiation force smaller by a factor of order 10^3 for yeast relative to iron at the same acoustic field, and the ratio grows to $\approx 10^6$ for a 100:1 radius ratio. Combined with the reduced effective driving voltage discussed above which further lowers the acoustic pressure amplitude p_a, and therefore the acoustic energy density $E_a \propto {p_a}^2$ that enters the Gor'kov-derived force expression (Eq. 10) in chapter 1 the resulting radiation force on the yeast cells is plausibly too weak to compete with viscous drag and Brownian-scale thermal fluctuations at the cellular scale, so that no visible accumulation occurs at any of the tested frequencies, concentrations or observation times.

This outcome should not be read as a failure of the acoustic manipulation principle itself,

which was clearly demonstrated on the iron particles (Section 5.3) and at the macroscopic scale, on the Petri-dish platform of Chapter 4. Rather, it identifies the actuation amplitude available with the present driving hardware as the limiting factor for cell-scale biological particles, and points directly to the two concrete directions needed to close the gap: a driving amplifier capable of delivering the full nominal voltage across the piezoelectric load at the frequencies of interest (addressing the first factor above), and/or a higher intrinsic acoustic pressure design (e.g., a smaller microchannel cross-section or a resonance chosen for a larger $\langle P^2 \rangle$ at fixed input power) to compensate for the unfavorable r^3 scaling of the radiation force at the cellular scale.

5.5.2. Polystyrene Microspheres

Polystyrene microspheres of 50 µm diameter suspended in water were tested at 700 Hz inserted in the microchannel as shown in Figure 5.16. At 50 µm diameter (r = 25 µm), these spheres are five to fifteen times larger in radius than a yeast cell, and by the same r^3 scaling argument should experience a radiation force roughly 100 to 3000 times stronger than yeast at the same acoustic field making them a useful bracketing test between the iron particles (successfully trapped) and the yeast cells (not trapped).

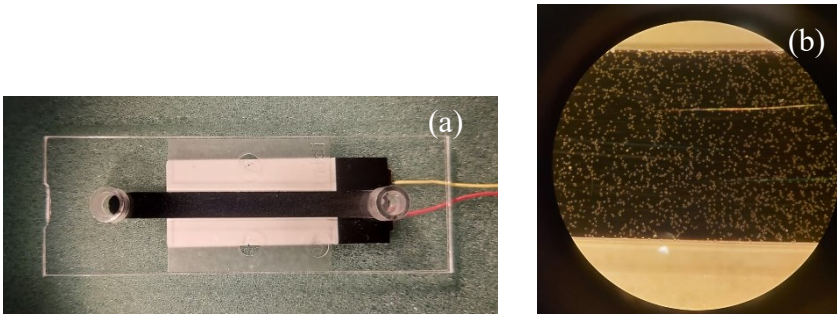


Figure 5.16. Polystyrene microspheres (d = 50 µm) in water at driving frequency 700 Hz (a) Top view, (b) Focused view inside the microchannel.

Contrary to the bracketing expectation above, the polystyrene microspheres show the same negative result as the yeast cells. The microscope image of Figures 5.16a and 5.16b shows the beads remaining densely but uniformly scattered across the field of view, with no visible band, clump, or any other reproducible spatial concentration despite being five to fifteen times larger in radius than a yeast cell.

This outcome is informative precisely because it fails to confirm the pure particle-size hypothesis, and points instead to the driving voltage as the dominant limiting factor. The acoustic radiation force of the Gor'kov potential depends on particle size through r^3, but it depends on the acoustic field itself through $\langle P^2 \rangle$ and $\langle V^2 \rangle$ i.e., quadratically in the acoustic pressure amplitude, which is in turn directly proportional to the voltage actually delivered to the piezoelectric actuator. If, as argued in Section 5.5.1, the effective voltage at 700 Hz is significantly reduced below its nominal value by the piezoelectric element's capacitive voltage-divider effect $V_{piezo}(f)$, then $\langle P^2 \rangle$ collapses roughly as the square of that already-reduced voltage, and the resulting radiation force can fall to a negligible level regardless of particle size: a 1000× larger r^3 factor for the 50 µm polystyrene spheres relative to yeast cannot compensate for an acoustic field that has itself been suppressed by a comparable or larger

factor. In other words, if the acoustic pressure amplitude at the driving frequency is insufficient to trap even a 50 µm rigid sphere, a particle size at which trapping is routinely achieved in the acoustofluidics literature under adequate driving conditions, the bottleneck is most likely the actuation stage itself (amplifier output, and/or its impedance mismatch with the capacitive piezoelectric load) rather than the size or mechanical properties of the particles being manipulated. Particle size (and the associated r^3 scaling) very likely still matters in principle, but with the present driving hardware, the acoustic field at 700 Hz appears to be too weak to trap any of the biologically relevant particles tested in this thesis. Iron particles showed a different behavior due to their density contrast, which yields a radiation force by orders of magnitude larger.

Taken together, the results of this section indicate that the resonance conditions identified numerically and experimentally reliably manipulate dense, rigid, indicator-scale particles (iron fillings), but were not, with the present driving hardware, sufficient to manipulate cell-scale biological particles (yeast). This is consistent with the combined effect of reduced effective actuation voltage at the piezoelectric element and the strongly unfavorable radius-cubed scaling of the acoustic radiation force at the micrometer scale. Addressing the actuation-amplitude limitation identified here is expected to be the key next step towards applying the piezo-actuated microchannel platform developed in this thesis to real biological particle manipulation, with future lab-on-a-chip applications such as contactless, label-free sorting, concentration, and separation of cells or other biological particles as the ultimate motivation for this line of work.

Conclusions and Future Perspectives

With this project, the effectiveness of self-mixing interferometry for the characterization of piezoelectrically actuated structures has been demonstrated, from the piezo-MEMS speaker to the Plexiglas plate, the Petri dish and the polymeric microchannel. The laser diode acts at the same time as source and sensor, so no external interferometer is needed: the technique is simple and low-cost, and it allows a non-invasive, non-contact measurement of resonance frequencies, displacement sensitivity and phase delay. The COMSOL models reproduced the main spectral features of the devices and provided the mode shapes and pressure fields needed to interpret the experiments.

The potentiality of low-frequency piezoelectric actuation has been explored for particle manipulation: in dry conditions, particles collect along the nodal lines (Chladni patterns), while in water they are driven towards the antinodes (inverse Chladni patterns), which allows density-based separation. In the microchannel, iron particles were successfully trapped at the fundamental resonance in the water-filled condition.

However, further studies can be carried out to improve the performance of the platform. In the microchannel, yeast cells and polystyrene microspheres did not show any reproducible accumulation. The acoustic radiation force scales with the cube of the particle radius, and the voltage delivered to the actuator decreases with frequency because the piezoelectric element behaves as a capacitor connected to a source with finite output impedance. This identifies the available driving amplitude as the limiting factor, not a failure of the actuation principle. In addition, the experimental resonances of the microchannel are about 6–15% higher than the simulated ones, and a more realistic description of the boundary conditions and of the cavity can reduce this difference.

For future work, a high-power driver able to deliver the full voltage at the frequencies of interest would allow the microchannel to be driven at higher frequencies, where the acoustic radiation force on small particles is stronger. In this way, micrometer-sized biological particles such as red blood cells, white blood cells and platelets could be manipulated. Since they differ in size, density and compressibility, they could be separated from a blood sample, for example for medical diagnostics, in a low-cost device made of standard consumables.

References

1. Liu, J., Tan, H., Zhou, X., Ma, W., Wang, C., Tran, N.-M.-A., Lu, W., Chen, F., Wang, J., & Zhang, H. “Piezoelectric thin films and their applications in MEMS: A review”. Journal of Applied Physics, 137(2), 020702, 2025.
2. Gill, M., Máthé, M. T., Salamon, P., Gleeson, J. T., & Jákli, A. “From solid to liquid piezoelectric materials”. Materials Horizons, 12(21), 8920-8942, 2025.
3. Mohd Radzi, M. H., & Kok, S. L. “Investigation of the piezoelectric charge coefficient d33 of thick-film piezoelectric ceramics by varying poling and repoling conditions”. International Conference on Mathematics, Engineering & Industrial Applications, 1660, 070083,2015.
4. Chen, J., Fei, C., Lin, D., Gao, P., Zhang, J., Quan, Y., Chen, D., Li, D., & Yang, Y. “A Review of UltraHigh Frequency Ultrasonic Transducers”. Frontiers in Materials, 8, 733358, 2021.
5. Tadigadapa, S., & Mateti, K. “Piezoelectric MEMS sensors: state-of-the-art and perspectives”. Measurement Science and Technology, 20(9), 092001, 2009.
6. Toth, F., Hassanpour Guilvaiee, H., & Jank, G. “Acoustics on small scales: Modelling viscous effects in MEMS devices”. e&i Elektrotechnik und Informationstechnik, 138(3), 155-161, 2021.
7. Qiu, Y., Gigliotti, J. V., Wallace, M., Griggio, F., Demore, C. E. M., Cochran, S., & Trolier-McKinstry, S. “Piezoelectric Micromachined Ultrasound Transducer (PMUT) Arrays for Integrated Sensing, Actuation and Imaging”. Sensors, 15(4), 8020-8041, 2015.
8. Friend, J., & Yeo, L. Y. “Microscale acoustofluidics: Microfluidics driven via acoustics and ultrasonics”. Reviews of Modern Physics, 83(2), 647-704, 2011.
9. Bruus, H. “Acoustofluidics 2: Perturbation theory and ultrasound resonance modes”. Lab on a Chip, 12(1), 20-28, 2012.
10. Dual, J. and Schwarz, T. “Acoustofluidics 3: Continuum mechanics for ultrasonic particle manipulation”. Lab on a Chip, 12(2), 244-252, 2012.
11. Bach, J. S. and Bruus, H. “Theory of pressure acoustics with viscous boundary layers and streaming in curved elastic cavities”. The Journal of the Acoustical Society of America, 144(2), 766-784, 2018.
12. Bruus, H. “Acoustofluidics 7: The acoustic radiation force on small particles”. Lab on a Chip, 12(6), 1014-1021, 2012.
13. Gor'kov, L. P. “On the forces acting on a small particle in an acoustical field in an ideal fluid”. Soviet Physics Doklady, 6(9), 773-775, 1962.
14. Settnes, M. and Bruus, H. “Forces acting on a small particle in an acoustical field in a viscous fluid”. Physical Review E, 85(1), 016327, 2012.
15. Barnkob, R., Augustsson, P., Laurell, T. and Bruus, H. “Measuring the local pressure amplitude in microchannel acoustophoresis”. Lab on a Chip, 10(5), 563-570, 2010.
16. Wiklund, M., Green, R. and Ohlin, M. “Acoustofluidics 14: Applications of acoustic streaming in microfluidic devices”. Lab on a Chip, 12(14), 2438-2451, 2012.
17. Muller, P. B., Barnkob, R., Jensen, M. J. H. and Bruus, H. “A numerical study of microparticle acoustophoresis driven by acoustic radiation forces and streaming-induced drag forces”. Lab on a Chip, 12(22), 4617-4627, 2012.
18. Barnkob, R., Augustsson, P., Laurell, T. and Bruus, H. “Acoustic radiation- and streaming-induced microparticle velocities determined by microparticle image

velocimetry in an ultrasound symmetry plane". Physical Review E, 86(5), 056307, 2012.
19. Antfolk, M., Muller, P. B., Augustsson, P., Bruus, H. and Laurell, T. "Focusing of sub-micrometer particles and bacteria enabled by two-dimensional acoustophoresis". Lab on a Chip, 14(15), 2791-2799, 2014.
20. Friend, J. and Yeo, L. Y. "Microscale acoustofluidics: Microfluidics driven via acoustics and ultrasonics". Reviews of Modern Physics, 83(2), 647-704, 2011.
21. Zhou, Q., Sariola, V., Latifi, K. and Liimatainen, V. "Controlling the motion of multiple objects on a Chladni plate". Nature Communications, 7, 12764, 2016
22. Leissa, A. W. "Vibration of Plates". NASA SP-160, Scientific and Technical Information Division, NASA, Washington, D.C., 1969.
23. Vuillermet, G., Gires, P.-Y., Casset, F. and Poulain, C. "Chladni patterns in a liquid at microscale". Physical Review Letters, 116(18), 184501, 2016.
24. van Gerner, H. J., van der Hoef, M. A., van der Meer, D. and van der Weele, K. "Inversion of Chladni patterns by tuning the vibrational acceleration". Physical Review E, 82(1), 012301, 2010.
25. Tuan, P. H., Wen, C. P., Chiang, P. Y., Yu, Y. T., Liang, H. C., Huang, K. F. and Chen, Y. F. "Exploring the resonant vibration of thin plates: Reconstruction of Chladni patterns and determination of resonant wave numbers". The Journal of the Acoustical Society of America, 137(4), 2113-2123, 2015.
26. Lei, J. "Formation of inverse Chladni patterns in liquids at microscale: roles of acoustic radiation and streaming-induced drag forces". Microfluidics and Nanofluidics, 21(3), 50, 2017.
27. Wang, Q., Ruan, T., Xu, Q., Hu, Z., Yang, B., You, M., Lin, Z. and Liu, J. "A piezoelectric MEMS speaker with a combined function of a silent alarm". Micromachines, 14(3), 702, 2023.
28. Gazzola, C. et al. "On the design and modeling of a full-range piezoelectric MEMS loudspeaker for in-ear applications". Journal of Microelectromechanical Systems, 32(6), 626-637, 2023.
29. Männchen, A., Stoppel, F., Brocks, T., Niekiel, F., Beer, D. and Wagner, B. "Design and electroacoustic analysis of a piezoelectric MEMS in-ear headphone". AES International Conference on Headphone Technology, 2019.
30. Ullmann, D. "Life and work of E.F.F. Chladni". The European Physical Journal Special Topics, 145(1), 25-32, 2007.
31. Stoppel, F., Fankhänel, J., Giese, T., Eisermann, C., Pieper, I. and Lofink, F. "Highly miniaturized 115 dB full-range MEMS loudspeaker for in-ear applications". Sensors and Actuators A: Physical, 116373, 2025.
32. Anelli, C. and Merlo, S. "Electro-mechanical frequency response of a piezo-MEMS speaker measured by laser diode feedback interferometry". Journal of Microelectromechanical Systems, 34(4), 452-458, 2025.
33. Rembe, C., Kant, R. and Muller, R. S. "Optical measurement methods to study dynamic behavior in MEMS". Proceedings of SPIE, 4400, Microsystems Engineering: Metrology and Inspection, 2001.
34. Rembe, C., Kowarsch, R., Ochs, W., Dräbenstedt, A., Giesen, M. and Winter, M. "Optical three-dimensional vibrometer microscope with picometer-resolution in x, y, and z". Optical Engineering, 53(3), 034108, 2014.
35. Brunner, S., Völkel, R., & Zappe, H. Compact VCSEL-based optical position and displacement sensors for micro-actuators. Sensors and Actuators A: Physical, 110(1-3), 270–276, (2004).

36. Taimre, T., Nikolić, M., Bertling, K., Lim, Y. L., Bosch, T. and Rakić, A. D. “Laser feedback interferometry: a tutorial on the self-mixing effect for coherent sensing”. Advances in Optics and Photonics, 7(3), 570-631, 2015.
37. Donati, S. “Developing self-mixing interferometry for instrumentation and measurements”. Laser & Photonics Reviews, 6(3), 393-417, 2012.
38. Giuliani, G., Norgia, M., Donati, S. and Bosch, T. “Laser diode self-mixing technique for sensing applications”. Journal of Optics A: Pure and Applied Optics, 4(6), S283-S294, 2002.
39. Donati, S., Giuliani, G. and Merlo, S. “Laser diode feedback interferometer for measurement of displacements without ambiguity”. IEEE Journal of Quantum Electronics, 31(1), 113-119, 1995.
40. Lang, R. and Kobayashi, K. “External optical feedback effects on semiconductor injection laser properties”. IEEE Journal of Quantum Electronics, 16(3), 347-355, 1980.
41. Scalise, L., Yu, Y., Giuliani, G., Plantier, G. and Bosch, T. “Self-mixing laser diode velocimetry: application to vibration and velocity measurement”. IEEE Transactions on Instrumentation and Measurement, 53(1), 223-232, 2004.
42. Merlo, S. and Donati, S. “Reconstruction of displacement waveforms with a single-channel laser-diode feedback interferometer”. IEEE Journal of Quantum Electronics, 33(4), 527-531, 1997.
43. Bendat, J. S. and Piersol, A. G. “Random Data: Analysis and Measurement Procedures”. 4th ed., John Wiley & Sons, Hoboken, NJ, 2010.
44. Lei, J., Hill, M. and Glynne-Jones, P. “Numerical simulation of 3D boundary-driven acoustic streaming in microfluidic devices”. Lab on a Chip, 14(3), 532-541, 2014.
45. Kaiser, B., Langa, S., Ehrig, L., et al. “Concept and proof for an all-silicon MEMS micro speaker utilizing air chambers”. Microsystems & Nanoengineering, 5, 2019.
46. Gemelli, A., Tambussi, M., Fusetto, S., Aprile, A., Moisello, E., Bonizzoni, E. and Malcovati, P. “Recent trends in structures and interfaces of MEMS transducers for audio applications: a review”. Micromachines, 14(4), 847, 2023.
47. Wang, H., Chen, Z. and Xie, H. “A high-SPL piezoelectric MEMS loud speaker based on thin ceramic PZT”. Sensors and Actuators A: Physical, 309, 112018, 2020.
48. Wang, H., Li, M., Yu, Y., Chen, Z., Ding, Y., Jiang, H. and Xie, H. “A piezoelectric MEMS loud speaker based on ceramic PZT”. 20th International Conference on Solid-State Sensors, Actuators and Microsystems & Eurosensors XXXIII (TRANSDUCERS 2019), Berlin, 2019.
49. Zheng, Q., Cao, K., Bai, C., Ma, X. and Deng, N. “An ultra-high low-frequency SPL piezoelectric MEMS loudspeaker based on sputtered PZT”. Sensors and Actuators A: Physical, vol. 389, no. 116551, 2025.
50. Mingsian Bai and JW Liao, " Acoustic Analysis and Design of Miniature Loudspeakers for Mobile Phones," Journal of the Audio Engineering Society, 53(11):1061-1076, 2005.
51. D.J. Burns. et al, “A system for automatic electrical and optical characterization of microelectromechanical devices”, Journal of Microelectromechanical Systems, 8(4), 473 – 482, 1999.
52. Bosch, T., Servagent, N. and Donati, S. “Optical feedback interferometry for sensing application”. Optical Engineering, 40(1), 20-27, 2001.
53. Norgia, M. and Donati, S. “A displacement-measuring instrument utilizing self-mixing interferometry”. IEEE Transactions on Instrumentation and Measurement, 52(6), 1765-1770, 2003.

54. hang, Z., Gao, Y. and Su, W. “Laser self-mixing interferometer for MEMS dynamic measurement”. Frontiers of Optoelectronics, 6(2), 210-215, 2013.
55. STMicroelectronics and USound. “STMicroelectronics and USound Deliver First Advanced MEMS Silicon Micro-Speakers”. Press release, Geneva and Graz, 3 January 2018.
56. STMicroelectronics and USound. “STMicroelectronics and USound Agree to Make World’s First Spectacular-Sounding MEMS Speakers”. Press release, Geneva and Graz, 21 February 2017.
57. Alison E. Hake. et al, “Ultraminiature AlN diaphragm acoustic transducer”, Appl. Phys. Lett. 117, 143504, 2020.
58. USound Technical Specifications, "Ganymede Series Piezo-MEMS Loudspeaker Technical Datasheet v2.5," USound GmbH, Graz, Austria, Tech. Rep., 2021.
59. W. T. Thomson, Theory of Vibration with Applications, 5th ed. Upper Saddle River, NJ: Prentice Hall, 1998.
60. E. Bodo, L. Ciccarelli, V. Bello, S. Morganti, S. Merlo, “Assessment of Vibration Frequencies of Piezo-actuated Panel by Model-Assisted Self-Mixing Interferometry”, IEEE Open Journal of Instrumentation and Measurement, vol. 4, pp. 1-8, 2025.
61. Junjun Lei, "Formation of inverse Chladni patterns in liquids at microscale: roles of acoustic radiation and streaming-induced drag forces", Microfluid Nanofluidics, 21(3):50, 2017.